UiO : Department of Mathematics
University of Oslo

Investigating the Interaction Between Morphology of the Anterior Bend and Aneurysm Initiation

Henrik Aasen Kjeldsberg

Master's Thesis, Spring 2018

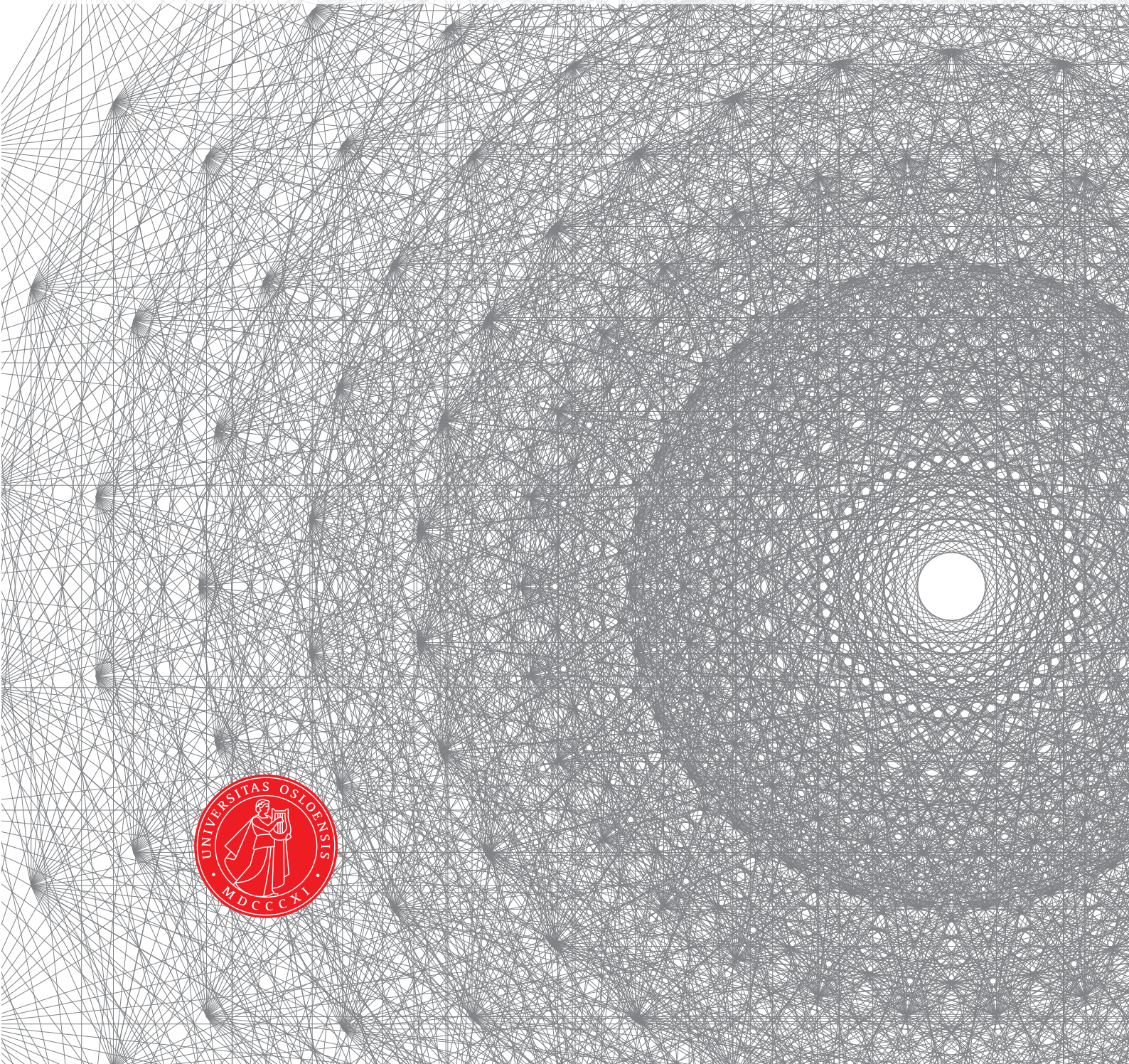

This master's thesis is submitted under the master's programme *Mechanics*, with programme option *Mechanics*, at the Department of Mathematics, University of Oslo. The scope of the thesis is 60 credits.

The front page depicts a section of the root system of the exceptional Lie group E_8, projected into the plane. Lie groups were invented by the Norwegian mathematician Sophus Lie (1842–1899) to express symmetries in differential equations and today they play a central role in various parts of mathematics.

Abstract

Cerebral aneurysms are bulges on the artery and are most commonly located at bifurcations in the vicinity of the Circle of Willis. The presence of aneurysms is statistically linked with morphological features of the main arteries supplying the brain with blood.

Previous work by Bergersen (2016) studied wider angles in the terminus bifurcation of the internal carotid artery (ICA), and area variations of the vessel. The goal of this thesis was to continue development of methods used to manipulate morphological features in the ICA. We explored angle and curvature variations in the carotid siphon bend located in the ICA, upstream of where most aneurysms are formed.

The manipulations were performed on ten healthy patient-specific models. We studied hemodynamic stimuli at the bifurcations and the presence of turbulent flow. Curvature variations were found not to affect the time-averaged wall shear stress. However, the occurrence of unstable flow varied slightly, without following any particular trend. Similarly, angle variations were found not to affect the hemodynamic stress, but correlated with the presence of unstable flow. The results are in contradiction to the leading theory for aneurysm initiation, and suggest that the temporally varying stress from the unstable flow is a plausible source for aneurysm initiation.

Preface

This thesis has been written to complete the Master of Science degree at the University of Oslo, Faculty of Mathematics and Natural Sciences, Department of Mathematics, Mechanics Division.

In the completion of the thesis, I have been so fortunate to have been able to write and perform the whole thesis in collaboration with The Center for Biomedical Computing at Simula Research Laboratory at Fornebu.

I would first and foremost like to express my greatest gratitude to my supervisor, Aslak Wigdahl Bergersen, for his guidance and much needed help throughout the whole period. Be it in person, through e-mails, or Skype; he has always provided me with excellent advice and support. Second, I would like to thank my supervisor Dr. Kristian Valen-Sendstad for always being helpful and giving me insight into the motivation behind the previous work on this subject. I would also like to thank my co-supervisor Professor Mikael Mortensen for the support and great lectures on computational fluid dynamics.

A special thanks to my closest friends at the University of Oslo for the past five years, Kristoffer Ulvik Høisæther, Anders Lindstrøm, and Tale Bakken Ulfsby. My years in Oslo would not have been the same, had it not been for your wonderful company and support, and all the unforgettable Fridays.

Finally, I would like to thank my father, Fredrik, for his love, help, and continuous support in everything I pursue.

Henrik Aasen Kjeldsberg
Oslo, May 2018.

Contents

1. Medical Background and Motivation

A stroke is a medical condition where the blood supply to a region of the brain is blocked, which reduces the amount of oxygen and nutrients the brain receives, causing brain cells to die. Stroke is the second leading cause of death, accounting for 11.8% of all deaths worldwide in 2015, and is the leading cause of disabilities [1]. Furthermore, stroke can result in permanent brain damage and cause physical or mental disabilities. There are two main types of stroke: ischemic stroke caused by a blockage, and hemorrhagic stroke caused by bleeding into the brain.

According to a large cohort study in Japan, 85% of hemorrhagic strokes are caused by cerebral aneurysms [2]. A cerebral aneurysm is a balloon-shaped bulge on a blood vessel with a distinct neck at its base, as depicted in Figure 1.1 **A**. Cerebral aneurysms are most common in the vicinity of the Circle of Willis, a network of arteries which distributes blood to the brain, see Figure 1.1 **B**. Within this network of arteries, aneurysms arise most commonly at bifurcations of the blood vessel, especially in the internal carotid artery (ICA) terminus bifurcation. A hemorrhagic stroke occurs when a cerebral aneurysm ruptures.

The blood flow in the cardiovascular system is driven by a pressure gradient. When an aneurysm ruptures, the pressure gradient is equalized, restricting the blood supply to the brain, which leads to a hemorrhagic stroke. Ruptured aneurysms constitute 5% of all strokes [3], and in contrast to other categories of strokes, half of the patients are younger than 55 years. Therefore ruptured aneurysms are responsible for 27.3% years of potential life lost as a result of stroke, before the age of 65 [4].

Ruptured aneurysms often lead to severe brain damage, and are fatal approximately 50% of the time, including pre-hospital deaths [3]. Among recovered patients, only 25% report complete recovery without any psychosocial or neurological symptoms [6]. Therefore, any new insight into the pathology and

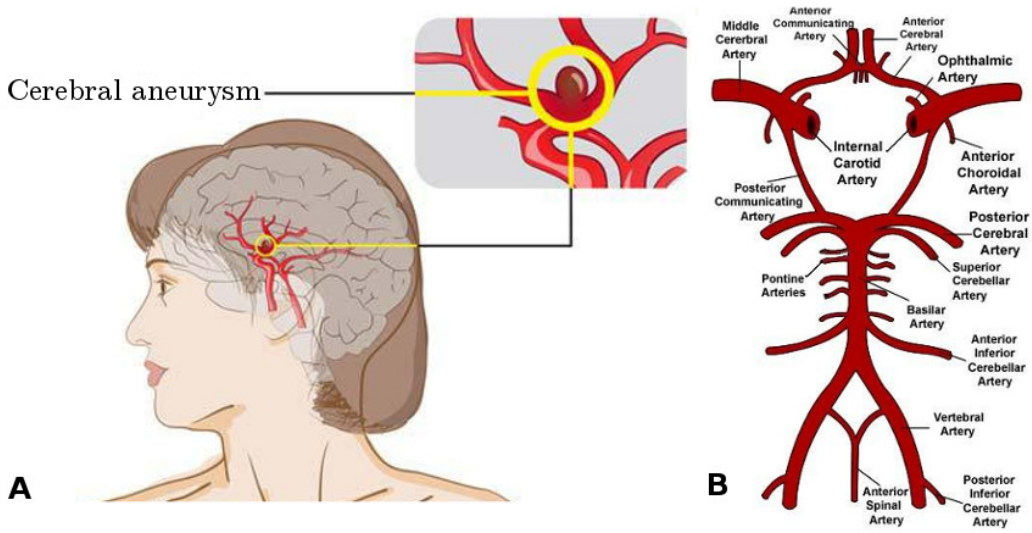

Figure 1.1: **A** Illustration of a cerebral aneurysm [5]. **B** Schematic representation of the Circle of Willis and surrounding arteries (Wikipedia Commons).

physiology of aneurysms is of great importance. Ultimately, further research can lead to improved detection of aneurysms, and advances in novel treatment methods, which can decrease the mortality rate, and improve recovery of patients.

A healthy artery consists mainly of three layers; the intima, the media, and the adventitia, with endothelial cells delimiting the intima from the lumen [7], see Figure 1.2. The endothelial cells are affected by the external stimuli exerted by the blood flow, causing them to signal muscle cells which adjusts the elasticity of the blood vessel and consequently dampens the variations in pressure during the cardiac cycle. This process is known as mechanotransduction [8], which happens continuously throughout the body.

It has previously been shown that hemodynamic forces regulate mechanotransduction [9]. Furthermore, previous studies have shown that high wall shear stress (WSS) and high WSS gradients (WSSG) are linked with vessel remodeling, and have consequently been hypothesized to be the cause of aneurysm initiation [10]. In order to study aneurysm initiation, we will investigate the hemodynamic stimuli in the ICA. Ideally, we would perform measurements of the forces on the arterial wall, giving insight into aneurysm initiation. However, we can not measure these parameters noninvasively. Therefore, we will use computational fluid dynamics (CFD) modeling to investigate the role of hemodynamic stimuli in arterial pathology. To gain insight into the mechanics of aneurysm initiation, we will perform CFD simulations of blood flow in the arteries, and perform computations of the WSS and WSSG. The results

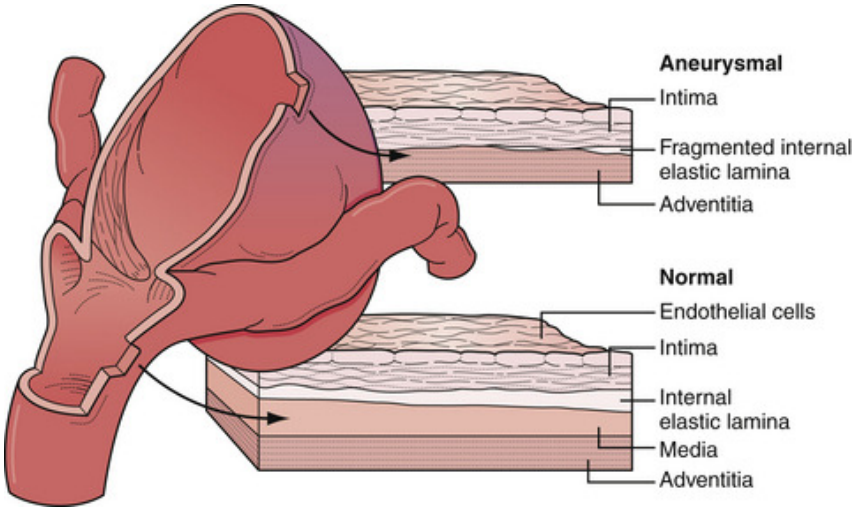

Figure 1.2: Layers of saccular cerebral arteries. Note the absence of endothelial cells, media and the fragmented internal elastic lamina in the aneurysm wall.

will give insight into which phenotypical hemodynamic stimuli are leading the unhealthy mechanotransduction causing adverse remodeling, being possible contributors towards aneurysm initiation.

The leading theory which explains the complex interactions of hemodynamic stimuli with intracranial aneurysm initiation is based on the results presented by Meng et al. (2006) and Metaxa et al. (2010). Meng et al. performed surgical interventions in canines [10, 11], where the left and right common carotid artery (CCA) were connected to create an arterial bifurcation, followed by introducing a considerably increased flow rate to induce aneurysm initiation, as illustrated in Figure 1.3 **A** and **B**. Metaxa et al. performed vessel ligation in rabbits, shutting off the left and right CCA to increase the basilar artery flow rate [12]. The ligation causes the flow rates to increase on average by 325%, causing aneurysm initiation in the subjects, following the procedure shown in Figure 1.4.

By impinging the blood flow, the experiments contain a major limitation, as the increased flow rates are not physiological in humans. There is also no way to assure that results based on animal models can be directly translated to human physiology, and there is no guarantee that the results from the surgically created bifurcation apply to the ICA bifurcation. Finally, Valen-Sendstad et al. (2013) and Khan et al. (2015) showed that the CFD solver used by Meng et al. was insufficient to capture possible flow instabilities [13, 14].

It has been previously shown that the transition from a steady, uniform flow

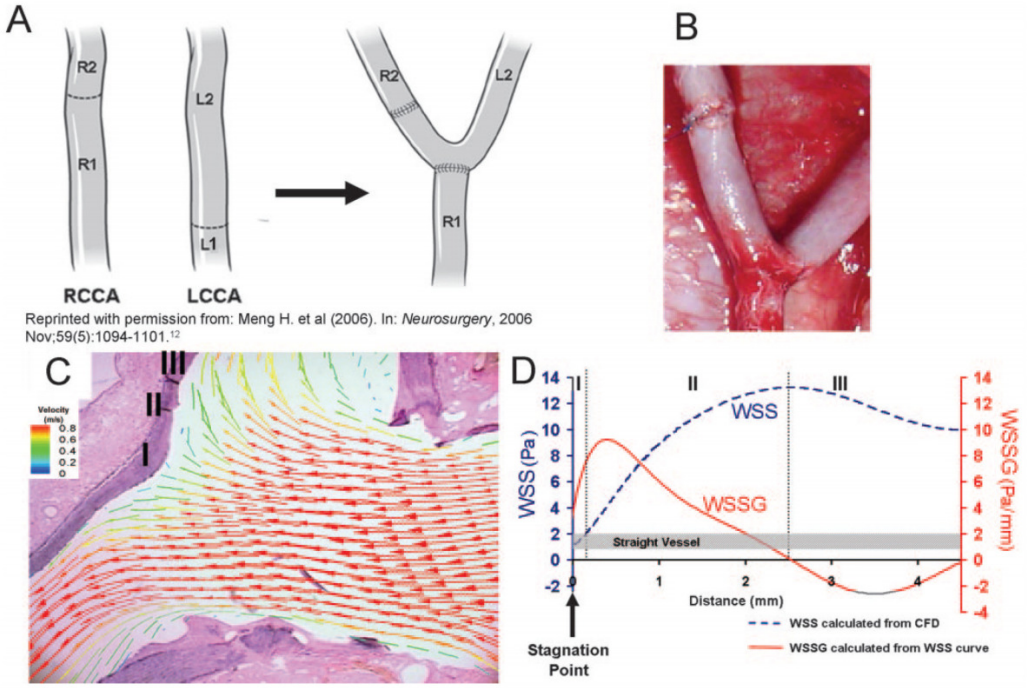

Figure 1.3: Illustration of vessel reconstruction from Meng et al. (2007) with the following caption: "**A**, Schematic of bifurcation creation. L (R)-CCA indicates left (right) common carotid artery. **B**, A created bifurcation. **C**, Over-lay of CFD-calculated velocity vectors (color indicates magnitude) on a histologic section of a bifurcation (from dog No. 4) 2 months after creation (van Gieson's staining). **D**, WSS and WSSG along the median wall of the bifurcation apex (left branch) reveal 3 regions with distinct flow characteristics: I, the impingement region; II, acceleration region; and III, recovery region. The range of normal physiologic WSS values for a straight vessel segment is indicated by the gray band."

to turbulent flow in a steady, straight pipe occurs at Reynolds number at approximately 2300, *in vitro*. The Reynolds number of flow in the arteries is substantially lower than 2300, which explains why most articles and textbook literature usually assume a laminar blood flow. However, it is questionable whether Reynolds' experiment is the best point of reference, considering it strictly applies to steady flow in a long, straight tube, whereas the carotid artery siphon is a tortuous segment of the ICA, consisting of sharp bends, pulsatile flow, and variable cross-sectional area. In spite of the consensus, Valen-Sendstad et al. (2013, 2014A, 2014B) controversially reported how blood flow in the carotid siphon could be characterized as unstable in some patients [16, 13, 17]. Following studies showed how solvers, time steps, and mesh resolution normally applied to cardiovascular problems were insufficient to detect

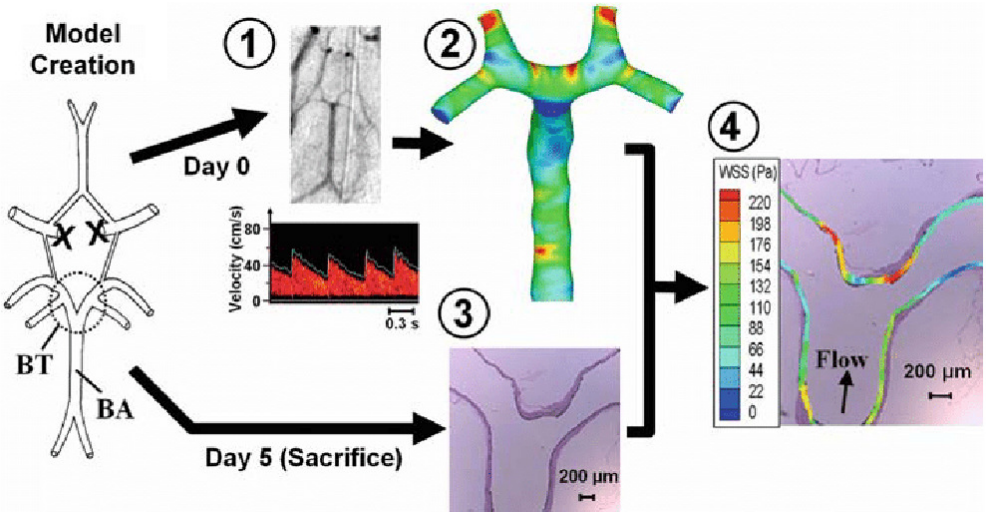

Figure 1.4: Experimental procedure from Metaxa et al. (2010), following Tremmel et al. (2010) [15], with the following caption: "Hemodynamics-histology co-mapping procedure applied to flow-induced destructive vascular remodeling in rabbits. Model creation entails bilateral common carotid artery ligation, inducing elevated flow in the basilar artery (BA). 1 Angiographic imaging of the BT bifurcation and transcranial Doppler (TCD) velocity measurement in the BA. 2 Image reconstruction and computational fluid dynamics (CFD). 3 Histology. 4 Co-mapping of start-point hemodynamics with end-point histology. WSS, wall shear stress; Pa, pascal."

blood flow instabilities [14, 13]. In addition, a successive report from Valen-Sendstad et al. (2014B) hypothesized that hemodynamic stimuli caused by unstable turbulent-like flow could eventually lead to aneurysm initiation [17].

In the light of the hypothesis of Valen-Sendstad et al., we seek to reexamine flow in the ICA by including possible flow instabilities. In addition, to investigate the theory by Meng et al., which proposed that high WSS and WSSG contributes to aneurysm initiation, a computation of WSS and WSSG is performed. To perform this validation, we will consider five morphological features of the internal carotid artery which have been statistically linked with the presence of cerebral aneurysms:

- Wider angles in the terminus bifurcation [18, 19]
- Area variations of the ICA [20]
- High peak curvature in the ICA [21]
- Narrow bend angle in the ICA siphon [22]
- Large torsion in the ICA [23]

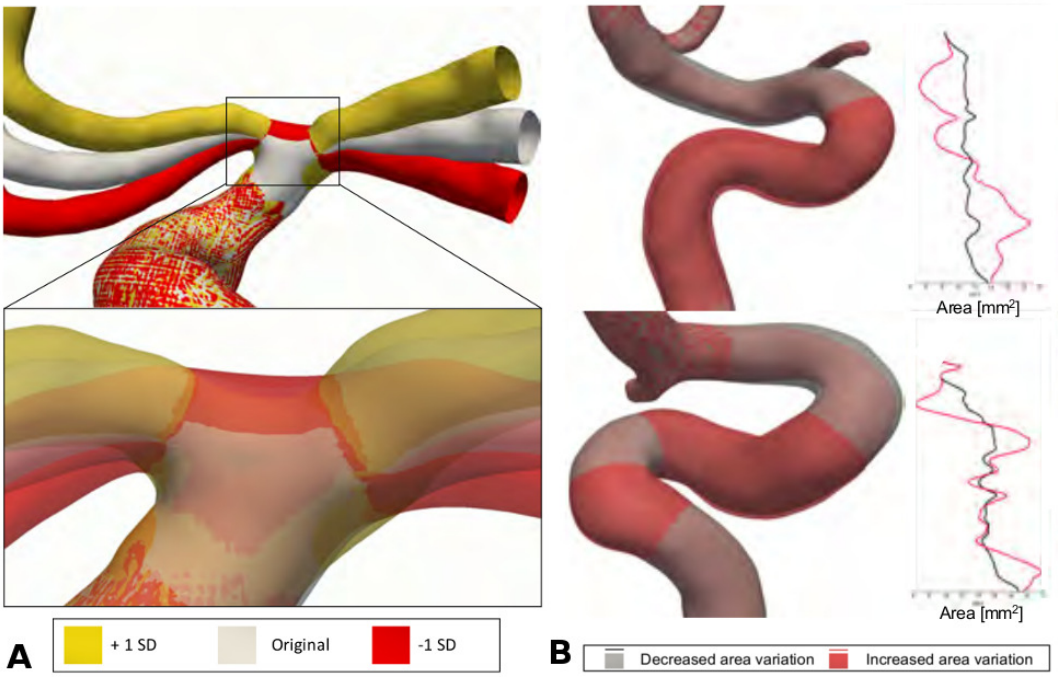

Figure 1.5: Illustration of vessel manipulations performed by Bergersen (2016) with the following caption: "**A** Rotation of daughter branches. The white geometries are the original surfaces, yellow are rotated upwards, and the red are rotated downwards. Each branch is rotated 18 degrees. **B** Result from two cases with varied area. The gray surface has a decreased area variation, and the red has an increased area variation. The plots next to each case is the area variation as a function of the length of the centerline."

By modifying the mentioned morphological features in patient-specific geometries, we can investigate the correlation between the hemodynamic stimuli and aneurysm initiation. In a previous study by Bergersen (2016), wider angles in the bifurcation and area variations were modified [24], as illustrated in Figure 1.5. By using a validated solver for biomedical applications, the relation to aneurysm initiation was investigated. However, there are still a number of features that can be examined.

The goal of this thesis is to extend the previous methods developed by Bergersen to manipulate morphology of patient-specific models, specifically the ICA. By performing CFD simulations in manipulated morphologies, we can investigate the correlation between hemodynamic stimuli at the terminus bifurcation with the initiation of aneurysms.

To achieve this goal, the thesis is split into five following chapters, including a mathematical background in Chapter 2:

- *Estimation of Discrete Curvature and Torsion*, which explores several methods used to estimate curvature and torsion. The methods will be applied for peak curvature estimation after geometric manipulation, and for geometric landmarking of the ICA.
- *Landmarking of the Internal Carotid Artery*, which considers two methods for objective subdivision of the carotid siphon into bends. By landmarking the ICA, we can define the anterior bend of the ICA, where the manipulations will be performed.
- *Measurement of the Anterior Bend Angle*, which examines multiple methods for angle measurement, specifically of the anterior bend angle located in the cavernous segment of the ICA. Angle measurements will be performed following geometric manipulation.
- *Geometric Manipulation of the Internal Carotid Artery*, which presents a framework for manipulation of patient-specific geometries, and proceeds by performing manipulations with respect to angle and curvature variations in the anterior bend.
- *A Computational Study on the Effects of Morphology Manipulations in the Internal Carotid Artery*, which investigates patient-specific geometries of healthy patients, and performs computational fluid dynamics simulations in the manipulated geometries. The computational results may enlighten the possible correlation between hemodynamic stimuli, and aneurysm initiation.

2. Mathematical Background

2.1 The Navier-Stokes Equations

The governing equations considered in this work are the incompressible Navier-Stokes equations. This set of nonlinear partial differential equations describe the motion of incompressible Newtonian fluids. The equations consist of conservation of mass and momentum, where the latter arises from Newton's second law [25]. The solutions $\mathbf{u} = \mathbf{u}(\mathbf{x}, t)$ and $p = p(\mathbf{x}, t)$ of the equations describe the fluid velocity field and the scalar pressure field in the fluid, respectively. Expressed as a single vector equation, the full Navier-Stokes equations for a viscous incompressible Newtonian fluid is

$$\frac{\partial \mathbf{u}}{\partial t} + \mathbf{u} \cdot \nabla \mathbf{u} = -\frac{1}{\rho} \nabla p + \nu \nabla^2 \mathbf{u} + \mathbf{f}, \tag{2.1}$$

$$\nabla \cdot \mathbf{u} = 0, \tag{2.2}$$

where ρ is the density of the fluid, ν is the kinematic viscosity of the fluid and $\mathbf{f}$ is a given body force, e.g. gravity. The equations (2.1) and (2.2) are commonly referred to as the momentum equation and the equation of continuity, respectively. At the time of writing, a proof of existence and smoothness of unique solutions of the Navier-Stokes equations is one of the seven millennium problems, and will result in a prize of one million dollars to whoever solves it [26]. Nevertheless, discretization of the equations throughout the past decades have enabled the possibility to use numerical solutions of Navier-Stokes equations for applications within science and engineering.

2.2 The Finite Element Method and FEniCS

The Navier-Stokes equations are a set of nonlinear partial differential equations. In the general case, few exact solutions of partial differential equations (PDE) are known, except for some special cases, often using a form of reduction technique to simplify the equation, such as separation of variables or the method of characteristics. Analytic solutions are scarce, and this is especially

true for nonlinear PDEs where there is no general method for finding exact solutions. Hence numerical techniques are used to find approximate solutions. One of the most widely used numerical methods is the finite element method. This technique involves deriving a weak formulation of a problem from the initial strong formulation. The procedure for deriving the weak form of a PDE is to multiply the equation by a function v, and integrate the resulting equation over the domain, often requiring integration by parts. The function v which multiplies the PDE is known as a test function, while the unknown function u, to be approximated, is referred to as a trial function. The formulation of a weak form can be described using Galerkin's method: find $u \in V$ such that

$$a(u, v) = L(v) \qquad \forall v \in \hat{V}, \tag{2.3}$$

where

$$V = \{v \in H^1(\Omega) \,|\, v = u_0 \text{ on } \partial\Omega\}, \tag{2.4}$$

$$\hat{V} = \{v \in H^1(\Omega) \mid v = 0 \text{ on } \partial\Omega\}. \tag{2.5}$$

In this formulation $\partial\Omega$ is the boundary of the domain, V is a trial space, $\hat{V}$ is a test space, $a(\,\cdot\,,\,\cdot\,)$ is a *bilinear form*, and $L(\cdot)$ a *linear form*. By identifying all the terms with the unknown function u and collecting them into the bilinear form, and similarly collecting all the terms with known functions in the linear form, the problem can be expressed directly into a finite element solver. The simulations in this thesis are performed by using the FEniCS finite element software library [27], including the open source solver *Oasis* [28], and post-processing using ParaView [29]. FEniCS is a tool designed for automated solution of PDEs, and is a collaborative project between several research institutes around the world. FEniCS is user friendly, and does not require a thorough understanding of the abstract mathematical theory behind the finite element method. Scripts can be implemented in Python and C++, and for our purposes, we will be developing code written in Python. The general way of solving a physical problem with FEniCS can be summarized into the following steps:

1. Identify the PDE and its boundary conditions.

2. Reformulate the PDE problem as a weak formulation.

3. Implement the problem, along with definitions of input data, and a mesh for the domain, Ω.

4. Solve the variational problem and analyze the results.

2.3 Discretization of Navier-Stokes Equations

To solve the Navier-Stokes equations, there are numerous algorithms which have been developed. This thesis will be utilizing the fractional-step algorithm, which solves the original equations (2.1) and (2.2) by splitting the equations into smaller well-studied problems, like the Poisson equation. Temporal discretization is performed by using a finite difference scheme, while the spatial coordinates are discretized by finite elements. By following Simo and Armero (1994), a general second-order algorithm can be written as [30]

$$\frac{u_k^\star - u_k^{n-1}}{\Delta t} + B_k^{n-1/2} = -\nabla_k p^\star + \nu \nabla^2 \tilde{u}_k + f_k^{n-1/2} \qquad \text{for } k = 1, \ldots, d, \quad (2.6)$$

$$\nabla^2 \phi = -\frac{1}{\Delta t} \nabla \cdot \mathbf{u}^\star \quad (2.7)$$

$$\frac{u_k^n - u_k^\star}{\Delta t} = -\nabla_k \phi \qquad \text{for } k = 1, \ldots, d, \quad (2.8)$$

where $u_k^n = u(x_k, t^n)$ is the k-th component of the velocity profile at a given time t^n. The number of spacial dimensions is d and $\phi = p^{n-1/2} - p^\star$ is defined as a correction of the pressure, where $p^\star$ is the tentative pressure. There is also the tentative velocity $u^\star$ being solved for, and we make the variable change $p = \frac{1}{\rho}\tilde{p}$ where $\tilde{p}$ is the physical pressure from Equation (2.1).

The Navier-Stokes equations include a non-linear term, the convective acceleration $\mathbf{u} \cdot \nabla \mathbf{u}$. Numerically, this can be linearized in several ways. We will apply a Adams-Bashforth projection to linearize the convected velocity,

$$B_k^{n-1/2} = (\mathbf{u}_k^{n-1/2} \cdot \nabla) u^{n-1/2} \approx \left(\frac{3}{2}\mathbf{u}^{n-1} - \frac{1}{2}\mathbf{u}^{n-2} \right) \cdot \nabla u^{n-1/2}, \quad (2.9)$$

and a midpoint Crank-Nicolson discretization for the term $u^{n-1/2}$ to keep the second order accuracy in time and avoid strict restrictions on the time step,

$$u^{n-1/2} \approx \frac{u^\star + u^{n-1}}{2}. \quad (2.10)$$

Using these discretizations lets us use a fractional step method to solve Equation (2.6) for all tentative velocity components, and Equation (2.7) for a pressure correction. In the general algorithm this procedure is performed a desired number of times before finally computing the velocity correction by solving Equation (2.8), which should satisfy the equation of continuity. The modified algorithm in *Oasis* preforms this procedure once. To summarize we can make an outline of the procedure of the fractional step method as shown in Algorithm 1.

Algorithm 1: Fractional Step Method. Rewritten following Mortensen et al. [28]

set initial condition;
$t = 0$;
while $t < T$ **do**
  $t = t + \Delta t$;
  while *error* $<$ *max_ error* ***and*** *iter* $<$ *max_ iter* **do**
    $\phi = p^{\star} = p^{n-1/2}$;
    solve 2.6 for $u_k^{\star}$ for $k = 0, \ldots, d$;
    solve 2.7 for $p^{n-1/2}$;
  end
  $\phi = p^{n-1/2} - \phi$;
  solve 2.8 for u_k^n for $k = 0, \ldots, d$;
  update to next time step;
end

2.4 Verification and Validation of *Oasis*

The algorithms presented in this thesis for solving the Navier-Stokes equations have no initial assurance of quality. We need some justification for the results generated in the following chapters. Therefore, we require performing verification and validation of the code and algorithms to evaluate the numerical models. Though often easily mistaken for being synonyms, the two evaluation processes have independent definitions, but with the same goal of assuring the quality of the product in question. With respect to the goal of this thesis, we separate the terms as:

- Verification: Ensuring that equations are implemented correctly into code and algorithms.
- Validation: Determining that the implemented equations and conditions are physically sound.

An additional distinction between the procedures is how computer code is handled. Although the code is considered verified, the performance may vary through validation using specific problems. Based on the performance and accuracy reported by Bergersen (2016), use of the Navier-Stokes solver *Oasis* was verified using the method of manufactured solutions [24].

Furthermore, validation of two different benchmarks was performed by Kvaal (2017), with the intention of validating that *Oasis* was well suited for computing turbulent flow in the human respiratory system [31]. The benchmarks

included the 2D laminar flow past a cylinder asymmetrically located in a channel, i.e., the von Karman vortex sheet, and the 3D Taylor-Green vortex. The 3D Taylor-Green vortex validation case was performed to verify that *Oasis* can, at a reasonable computation cost, and with limited numerical dissipation, describe turbulent transition and decay [32]. This is an appropriate validation case for our purpose, considering this thesis concerns the modeling of blood flow in the arteries, which have been reported to exhibit high-frequency flow fluctuations, characteristic of laminar vortex shedding, transitional or turbulent flow [13, 17].

Considering these are up to date verification and validation of the solver, this thesis will not perform any further verification or validation.

3. Estimation of Discrete Curvature and Torsion

There is a growing interest for estimation of three dimensional curves and its derivatives, starting from a discrete and noisy observation of the curve. Curvature is a geometric property measuring how much the curve deviates from a straight line and is computed from the first and second order derivatives of the curve. Estimation of curvature has two useful applications in this thesis. In Chapter 4 we segment the internal carotid artery (ICA) based on local curvature and torsion peaks, while Chapter 6 performs peak curvature computation within the carotid siphon to study the possible correlation between peak curvature, hemodynamic stimuli, and aneurysm initiation.

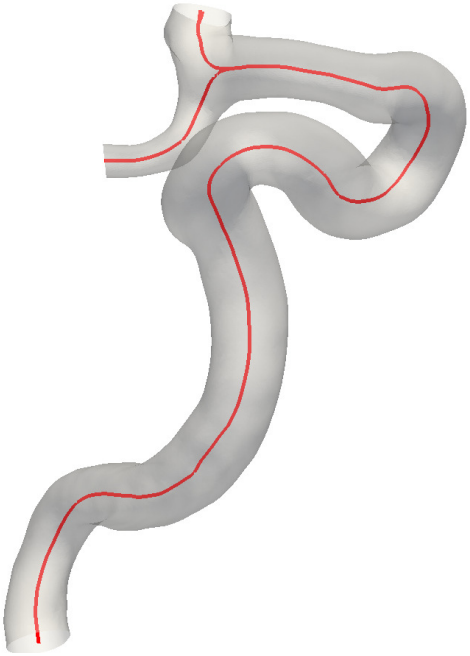

Figure 3.1: The centerline in a surface model of the ICA, colored in red.

Thus we need a robust method for computing the second order derivative of a noisy input curve while preserving the geometric features. There exists several algorithms for discrete curvature estimation, which requires us to perform a thorough comparison of a selected number of methods. The goal of this chapter is to present and compare methods for estimation of geometric properties of the ICA, in particular, curvature and torsion.

3.1 Introduction

3.1.1 The Centerline

Estimation of curvature and torsion is performed along the ICA centerline. A centerline is a representation of the shape of a vessel. The concept behind a centerline is more or less intuitive but has no unique mathematical definition. The algorithm implemented in the Vascular Modeling Toolkit (VMTK) computes the centerline starting from surface models of the artery lumen, and has the advantage that it is well characterized mathematically, and quite stable to perturbations on the surface [33]. Reconstruction of the artery yields a set of points in 3D which are computed as the centers of maximal spheres inscribed in the artery lumen. This set of points define the vessel centerline, as depicted in Figure 3.1.

3.1.2 Motivating Applied Problems

First, we consider the two landmarking algorithms presented by Bogunović et al. (2012) and Piccinelli et al. (2011) [23, 34]. Despite giving a thorough explanation for the landmarking procedure, neither provide any details on the smoothing procedure of the computed centerline, as landmarking relies on identifying local extremum of curvature and torsion of the ICA centerline. Naive approaches to this problem have only resulted in noisy centerlines, which produce unrealistic local extremum for curvature and torsion. The position of curvature and torsion peaks are used to objectively subdivide the carotid siphon into bends. Thus, the smoothing procedure, and estimation of geometric properties are crucial for determining the landmarks, as the proposed landmarking methods are highly sensitive to over-smoothing of the curvature and torsion.

Second, Chapter 5 presents a framework for manipulation of the anterior bend, located in the ICA. To study geometric properties, the centerline of the manipulated geometry is computed to measure peak curvature of the anterior bend, in comparison with measurements presented by Lauric et al. who proposed a correlation between curvature of the anterior bend with aneurysm initiation [21].

Thus, the goal is to investigate sophisticated methods for estimating geometric properties of the centerline, applied prior to landmarking, and succeeding geometric manipulation. In total, we tested five different existing methods. The following sections will provide an introduction to each of the methods, accompanied with a comparison of curvature estimations along the ICA centerline of a representative case.

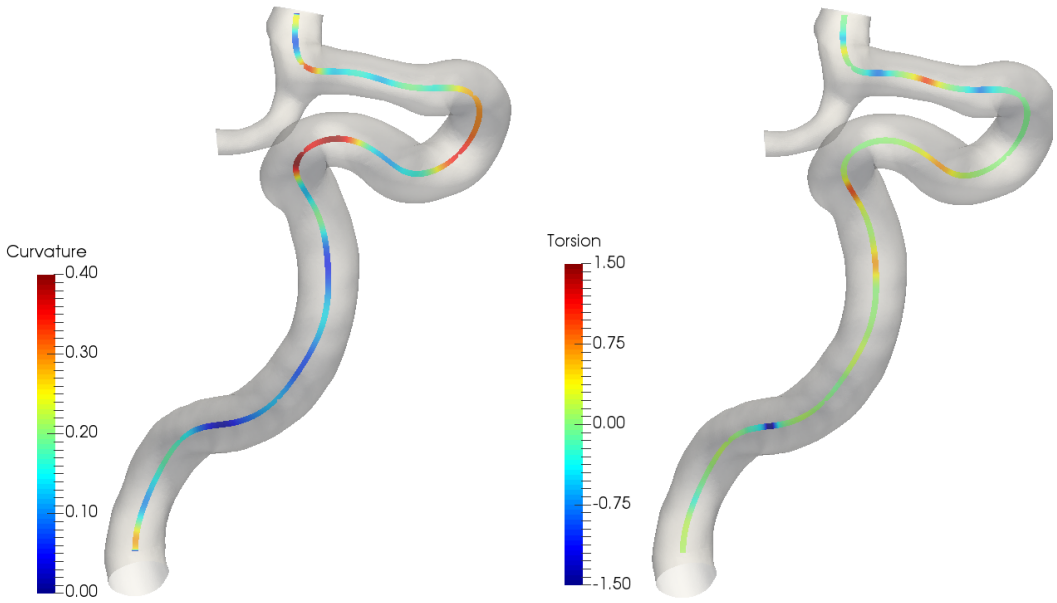

Figure 3.2: Curvature and torsion along the internal carotid artery centerline.

3.2 Method

3.2.1 Geometric Characterization of Centerlines

We will consider curvature and torsion as the relevant quantities for characterization of the ICA. Before proceeding, let us introduce a parametrization of the centerline in three dimensions,

$$\mathbf{r}(t) = (x(t), y(t), z(t)) \qquad t \in [0, 1]. \tag{3.1}$$

Furthermore, we can introduce the curvature of the curve $\mathbf{r}(t)$ as

$$\begin{aligned} \kappa &= \frac{\|\mathbf{r}'(t) \times \mathbf{r}''(t)\|}{\|\mathbf{r}'(t)\|^3} \\ &= \frac{\sqrt{(z''y' - y''z')^2 + (x''z' - z''x')^2 + (y''x' - x''y')^2}}{(x'^2 + y'^2 + z'^2)^{\frac{3}{2}}}, \end{aligned} \tag{3.2}$$

which measures the deviation of the curve from a straight line. The geometric definition of curvature at a given point $\mathbf{r}(t_i)$ is the inverse of the radius of the osculating circle, i.e., the circle that approximates the curve in $\mathbf{r}(t_i)$. In addition, the plane identified by the osculating circle is referred to as the osculating plane.

Finally, the torsion of a the curve $\mathbf{r}(t)$ is defined as

$$\begin{aligned}\tau &= \frac{\mathbf{r}'''(t) \cdot [\mathbf{r}'(t) \times \mathbf{r}''(t)]}{\|\mathbf{r}'(t) \times \mathbf{r}(t)\|^2} \\ &= \frac{x'''(y'z'' - y''z') + y'''(x''z' - x'z'') + z'''(x'y'' - x''y')}{(y'z'' - y''z')^2 + (x''z' - x'z'')^2 + (x'y'' - x''y')^2},\end{aligned} \tag{3.3}$$

which is a measure of how sharply the curve is twisting out of the plane of curvature, or equivalently its local deviation from lying on the osculating plane. Thus the sign of τ distinguishes between clockwise or counter-clockwise rotations to the osculating plane. Figure 3.2 displays the evaluation of curvature and torsion applied to the carotid siphon centerline extracted from an ICA model.

3.2.2 VMTK

An integrated method in VMTK is the script *vmtkcenterlinegeometry*, which computes geometric properties of the input centerline, including curvature and torsion [35]. Centerlines generated by VMTK are only guaranteed to be C^0 continuous [36], which motivates the use of finite differences for differentiation. For computation of curvature and torsion VMTK employs the use of central differences, which can be defined as follows.

Definition 3.2.1. Given a discrete centerline $\mathbf{r}_d(t_i) = (x_i, y_i, z_i)$, using the convention $x_i = x_d(t_i)$, with abscissa parameters t_i for $i = 1, \ldots, n$, an estimate of the first order derivatives is given by the *first central differences*

$$x_i' \approx \frac{x_{i+1} - x_{i-1}}{t_{i+1} - t_{i-1}}, \quad y_i' \approx \frac{y_{i+1} - y_{i-1}}{t_{i+1} - t_{i-1}}, \quad z_i' \approx \frac{z_{i+1} - z_{i-1}}{t_{i+1} - t_{i-1}}, \tag{3.4}$$

for $i = 2, \ldots, n-1$. Similarly, an estimate for the second order derivatives is given by the *second central differences*

$$x_i'' \approx \frac{\frac{x_{i+1}-x_i}{t_{i+1}-t_i} - \frac{x_i-x_{i-1}}{t_i-t_{i-1}}}{\frac{t_{i+1}-t_{i-1}}{2}}, \; y_i'' \approx \frac{\frac{y_{i+1}-y_i}{t_{i+1}-t_i} - \frac{y_i-y_{i-1}}{t_i-t_{i-1}}}{\frac{t_{i+1}-t_{i-1}}{2}}, \; z_i'' \approx \frac{\frac{z_{i+1}-z_i}{t_{i+1}-t_i} - \frac{z_i-z_{i-1}}{t_i-t_{i-1}}}{\frac{t_{i+1}-t_{i-1}}{2}}. \tag{3.5}$$

Although these approximations are of second order accuracy, a direct approach will not produce sufficient estimations due to the amount of noise of the computed centerlines. Thus the approximations are performed on a smoothed representation of the centerline, obtained using a Laplacian smoothing filter. The Laplacian smoothing filter performs the iteration

$$\mathbf{r}_d(t_i) \leftarrow \mathbf{r}_d(t_i) + \lambda \mathcal{L}(\mathbf{r}_d(t_i)), \tag{3.6}$$

a finite number of times, where $\mathcal{L}(\cdot)$ is the Laplace operator, discretized using finite differences as

$$\mathcal{L}(\mathbf{r}_d(t_i)) = \frac{\mathbf{r}_d(t_{i+1}) - 2\mathbf{r}_d(t_i) + \mathbf{r}_d(t_{i-1})}{2}, \tag{3.7}$$

and λ is a smoothing factor. In practice, the integrated Laplacian smoothing technique in *vmtkcenterlinegeometry* relies on two input parameters, namely the number of smoothing iterations and a smoothing factor. Without any advised values to use, other than the default values, we performed two separate comparisons; one for varying number of iterations and one for varying smoothing factor.

3.2.3 Splines

The method of spline interpolation combines several piecewise polynomial functions in order to approximate a finite number of points. We will, in particular, consider B-splines applied to the respective curvilinear coordinates of the centerline, implemented in the Python library SciPy [37]. Any spline curve of degree k can be written as a linear combination of B-splines. In the univariate case, the spline curve $f(x)$ can be expressed as

$$f(x) = \sum_{j=0}^{n-1} c_j B_{j,k;t}(x), \tag{3.8}$$

where c_j are coefficients, $B_{j,k;t}$ are B-spline basis functions of degree k, and knots t. The B-spline basis elements are defined as in [38].

Definition 3.2.2. Let k be a nonnegative integer and let $\mathbf{t} = (t_j)$ be a non-decreasing sequence of real numbers of length at least $k+2$, referred to as the knot vector. The jth B-spline of degree k, with knots $\mathbf{t}$, is defined as

$$B_{j,k}(x) = \frac{x - t_j}{t_{j+k} - t_j} B_{j,k-1}(x) + \frac{t_{j+k+1} - x}{t_{j+k+1} - t_{j+1}} B_{j+1,k-1}(x) \qquad \forall\, x \in \mathbb{R}, \tag{3.9}$$

where

$$B_{j,0}(x) = \begin{cases} 1, & \text{if } t_j \leq x < t_{j+1}, \\ 0, & \text{otherwise.} \end{cases} \tag{3.10}$$

Here, the convention that $0/0 = 0$ is used.

The advantage of using B-splines is that one can compute exact analytical expressions for the curvature and torsion, as the derivatives of splines are still splines. However, the drawback with using B-splines is choosing a suitable

polynomial degree and an appropriate number of knots. To compute torsion we need third order derivatives, which motivates choosing the polynomial degree equal to 4, representing cubic polynomials, C^4 differentiable at the knots.

Setting an appropriate number of uniform knots was initially performed with trial and error. With a purpose of not creating a too wiggly line, it was observed that the general outcome appeared to favor fewer knots. Regrettably, there is no general guideline for selection of the number of knots to use, as there is no easy way to determine which of the computed curvatures profiles are "correct", and when the line is sufficiently smooth.

3.2.4 Free-Knot Regression Splines

In contrast to other splining techniques where a fixed number of knots are uniformly distributed, the method of free-knot regression splines is based on regression splines where the number and position of knots are not set in advance. In the univariate case, we want to estimate the function $f(x)$, at a finite number of points, with the regression spline

$$\hat{f}(x) = \sum_{j=0}^{n-1} \hat{c}_j B_{j,k;t}(x), \tag{3.11}$$

where the coefficient vector $\hat{c} = (\hat{c}_0, \ldots, \hat{c}_{n-1})^T$ minimizes the sum of square error, defined as

$$SSE(\hat{c}) = \sum_{i=0}^{n-1} \Big(f(x_i) - \hat{f}(x_i) \Big)^2 . \tag{3.12}$$

Based on the original implementation for one-dimensional curves by Zhou and Shen [39], an extension for three-dimensional curves is presented by Sangalli et al. [40].

The free-knots are chosen in such a way that they minimize a penalized sum of squared errors criterion. The algorithm is initialized by an initial knot vector, before each subinterval is checked for addition of knots, followed by relocation and deletion of knots, based on the penalized sum of squares error criterion. Then the procedure repeats until no further knots are added, and the procedure ends.

An implementation of the algorithm for a three-dimensional case was written in MATLAB, as the splines used in the algorithm were not available in Python. Regrettably, the algorithm relies on three parameters as user input; the order of the spline, a penalization constant $\mathcal{C}$, and the number of initial

knots. The general consensus is to let the order of the spline to be of order $p+3$, where p is the order of the highest derivative that has to be computed. Considering the torsion is expressed by third order derivatives, p was set to 3 throughout the implementation. Sangilla et al. discussed the choice of penalization constant $\mathcal{C}$, and introduced the *Stein's unbiased risk estimate*, used as the main criterion for knot addition and relocation, and defined as

$$pSSE(\hat{c}) = \sum_{i=0}^{n-1} \Big(f(x_i) - \hat{f}(x_i) \Big)^2 + \mathcal{C}\hat{\sigma}^2(n-1), \tag{3.13}$$

where $\hat{\sigma}^2$ is an estimate of error variance. The application of the procedure presented by Sangilla et al. is analogous to our goal, with the intention of estimating individual ICA centerlines, and their respective curvature profile. Thus the advisatory choice of $\mathcal{C} = 4$ is supported, where they argue that the free-knot regression splines can accurately estimate the salient features of the centerline, without being too data-adapted. Relative to this selection, very high values of $\mathcal{C}$ can lead to centerline estimates which cannot fully capture the peaks and troughs in the first and subsequent derivatives, while very low values of $\mathcal{C}$ may instead yield estimates where the high frequency variations are fitted.

The final parameter is choosing the number of initial knots, where there is no in-depth argument for an optimal choice. One possibility for selection of initial knots is presented in the article by Zhou and Shen, although only intended to reduce the computational cost of the algorithm, and should not affect the result [39].

3.2.5 Discrete Derivatives

The final method for curvature estimation utilized discrete derivatives of discrete curves, as described by An et al. [41], and used by Lauric et al. for computation of the curvature reference data used during manipulation [21]. The definition of discrete derivatives as presented by An et al. is as follows.

Definition 3.2.3. Let $y_i = f_d(x_i), x_i \in \{x_1, x_2, \ldots, x_n\}$ be a discrete function. The value $y'_k = f'_d(x_k)$ given by

$$y'_k = f'_d(x_k) = \frac{\sum_{j=k-m_1}^{k+m_1}(x_j - x_k)(y_j - y_k)}{\sum_{j=k-m_1}^{k+m_1}(x_j - x_k)^2}, \tag{3.14}$$

is called the *discrete first derivative* of the discrete function $y_i = f_d(x_i)$ at the point $\mathbf{p}_k = (x_k, y_k)$ for $k = 1, \ldots, n$.

Similarly, the second order discrete derivative can be defined as

$$y''_k = f''_d(x_k) = \frac{\sum_{j=k-m_2}^{k+m_2}(x_j - x_k)(y'_j - y'_k)}{\sum_{j=k-m_2}^{k+m_2}(x_j - x_k)^2}. \tag{3.15}$$

In equations (3.14) and (3.15) m_1 and m_2 are the radius of the sliding neighborhood, corresponding to selecting m_1 or m_2 neighboring points around a given point $\mathbf{p}_k$. Expanding the definitions to a curve in 3D we can define a discrete parametrized curve $\mathbf{r}_d(t_i) = (x_d(t_i), y_d(t_i), z_d(t_i))$ for $t \in \{t_1, \ldots, t_n\}$, with t_i being the cumulative chord length defined as

$$t_i = \frac{\sum_{j=1}^{i-1} \|\mathbf{p}_{j+1} - \mathbf{p}_j\|}{\sum_{j=1}^{n-1} \|\mathbf{p}_{j+1} - \mathbf{p}_j\|} \qquad \text{for } i = 2, \ldots, n. \tag{3.16}$$

Combining the discrete derivatives and the differential geometry formula (3.2), we can define the geometric properties for a discrete curve.

Definition 3.2.4. Let $\mathbf{r}_d(t_i)$ be a discrete curve parametrized by a chord length. We can then define the properties

1. $\boldsymbol{t}_d(t_i) = \mathbf{r}'_d(t_i)/\|\mathbf{r}'_d(t_i)\|$ is the unit tangent vector of the discrete curve $\mathbf{r}_d(t_i)$.

2. $\kappa_d(t_i) = \|\boldsymbol{t}'_d(t_i)\|/\|\mathbf{r}'_d(t_i)\|$ is the curvature of the discrete curve $\mathbf{r}_d(t_i)$.

In essence, these definitions are derived by considering a constrained minimization problem using a Lagrange multiplier. Hence the computations of higher order discrete derivatives are equivalent to a least squares fitting.

The algorithm depends only on the radius of the sliding neighborhood, where we let $m = m_1 = m_2$ for convenience. An et al. illustrates how the algorithm handles noisy discrete curves by adding a zero-mean Gaussian noise to five discrete planar curves. The experimental results of curvature estimation show how the RMS errors is reduced as the radius m increases.

One can argue that an additional parameter of the algorithm is how the line is sampled. A resampled centerline with finer spacing would require an increased number of neighborhood points, without altering the curvature profile. In the presented results, the centerline was resampled in order to assure that the line was uniformly sampled, without altering the number of discrete points.

3.3 Comparison of Methods and Concluding Remarks for Estimation of Geometric Properties

The results along one of the centerlines in case P0157, used as the representative case, are shown in Figure 3.3. In Figure 3.4, an emphasis on the anterior bend is shown for all the proposed methods. Finally, the model and centerline, used as the representative case, are illustrated in Figure 3.5 **A**, along with a comparison between all the presented methods in Figure 3.5 **B**.

The results of smoothing in VMTK are shown in Figure 3.3 **A** and **B**, along with an emphasis on the anterior bend in Figure 3.4 **A** and **B**, for iteration and smoothing factor variation, respectively. Varying the number of iterations effects the curvature less compared to variation in the smoothing factor, by comparing curvature profiles generated by changing the number of iterations and the smoothing factor. Notice how the method produces several minor curvature peaks along the centerline, and is the only method to consistently detect two peaks within the anterior bend. Nonetheless, the comparison gave no further insight into the recommended choice of parameters, although a high number of iterations reduced the number of curvature extremum, which is favorable for landmarking.

A comparison of curvature profiles using B-splines for a varied number of knots is illustrated in Figures 3.3 **C** and 3.4 **C**. Notice how the peak curvature locations along the siphon are shifted, and do not converge. Furthermore, large variations in peak curvature can be observed, in particular between using 10 and 15 knots where the difference in peak curvature is approximately 0.2 mm^{-1} within the anterior bend.

The free-knot regression splines generates the curvature profile as illustrated in Figures 3.3 **D** and 3.4 **D**. Applying the algorithm to our data using a varying number of initial knots, within a small neighborhood, produced large variations in curvature, following no particular trend. As observed using B-splines, the peak curvature locations do not appear to converge, and there are large peak curvature differences throughout the centerline.

Figures 3.3 **E** and 3.4 **E** show the curvature profile using discrete derivatives, where we varied the radius of the sliding neighborhood. The results show an evident trend as the radius increases, and much higher stability compared to previous methods. We also observe a slight dampening effect for increasing number of neighbors, and the number of curvature extremum appear to

converge when the radius of the sliding neighborhood exceeds 20. Further increasing of the radius shows little change in curvature magnitude, and no obvious change in curvature peak position.

Finally we generate an overall comparison between the methods presented in this chapter, shown in Figure 3.5 **B**. The comparison shows how VMTK and B-splines generate small instabilities in curvature along the centerline, while the free-knot spline method and discrete derivative method generally produces a smoother line mainly capturing the dominant extremum. A concerning observation is the generation of two peaks along the siphon, generated by the integrated method in VMTK. Besides, most methods appear to collaboratively capture the first curvature peak, but sidetracks for following downstream peaks.

Tables 3.1 and 3.2 show the peak curvature within the anterior bend of the carotid siphon, using carefully selected input arguments. Table 3.1 shows the difference for models where we expect an increase in curvature, however only the method of discrete derivatives and free-knot splines show correspondence with the excepted outcome. Similarly, Table 3.2 shows the difference in models where the curvature is expected to increase. The results support the expected outcome, although there are large variations in the reported curvature values. Judging by these results, only discrete derivatives and free-knot splines are applicable for peak curvature measurements.

Nonetheless, during landmarking, the only area of interest is located along the carotid siphon which is generally well captured. Therefore we are motivated to perform a comparison using all the methods presented in this chapter in Chapter 4. On the other hand, for computation of peak curvature, we require a stable and consistent procedure. As shown in the previous comparisons, the method of discrete derivatives is considerably more stable, and appears to converge for increasing radius of the sliding neighborhood. Thus we will apply the method of discrete derivatives for peak curvature measurements in Chapter 6. Conveniently, this is the same method implemented in the reference article by Lauric et al., used for geometric analysis of the ICA [21].

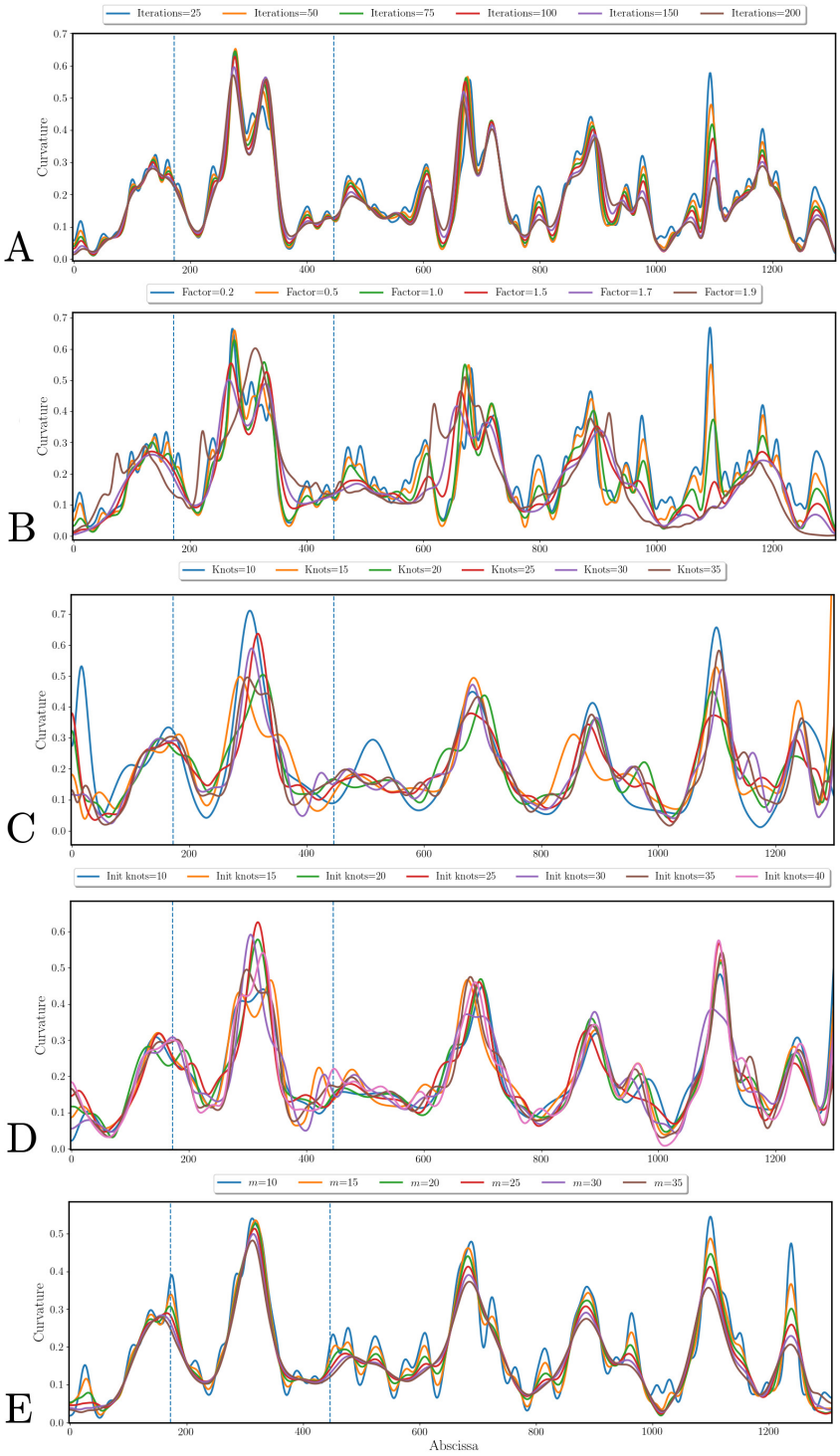

Figure 3.3: Comparison of curvature computation along the centerline using the following methods: **A** VMTK, Iteration variation. **B** VMTK, Smoothing factor variation. **C** B-Splines with knot variation. **D** Free-knot regression splines with initial knot variation. **E** Discrete derivatives with radius variation.

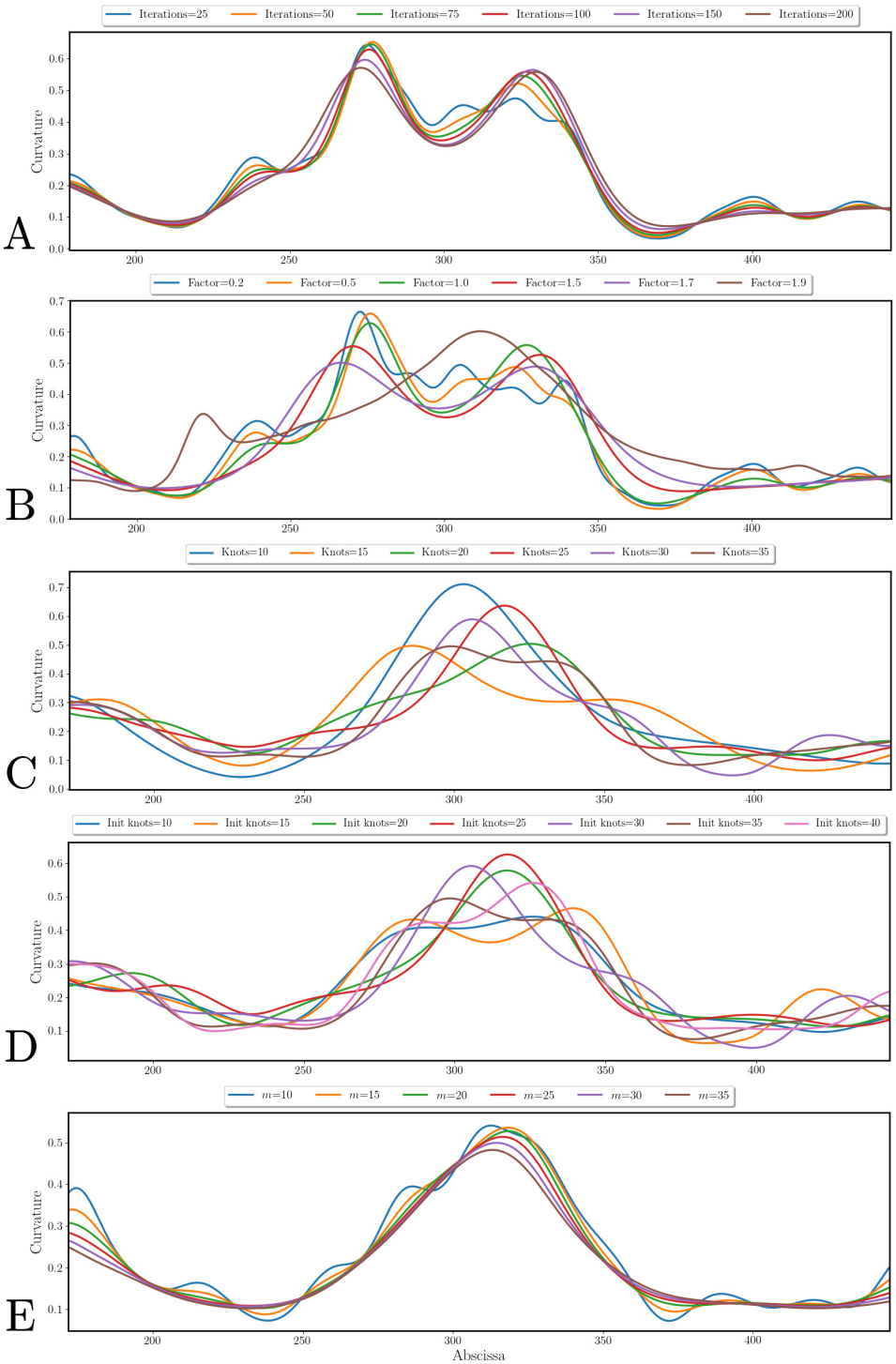

Figure 3.4: Comparison of curvature computation along the anterior bend using the following methods: **A** VMTK, Iteration variation. **B** VMTK, Smoothing factor variation. **C** B-Splines with knot variation. **D** Free-knot regression splines with initial knot variation. **E** Discrete derivatives with radius variation.

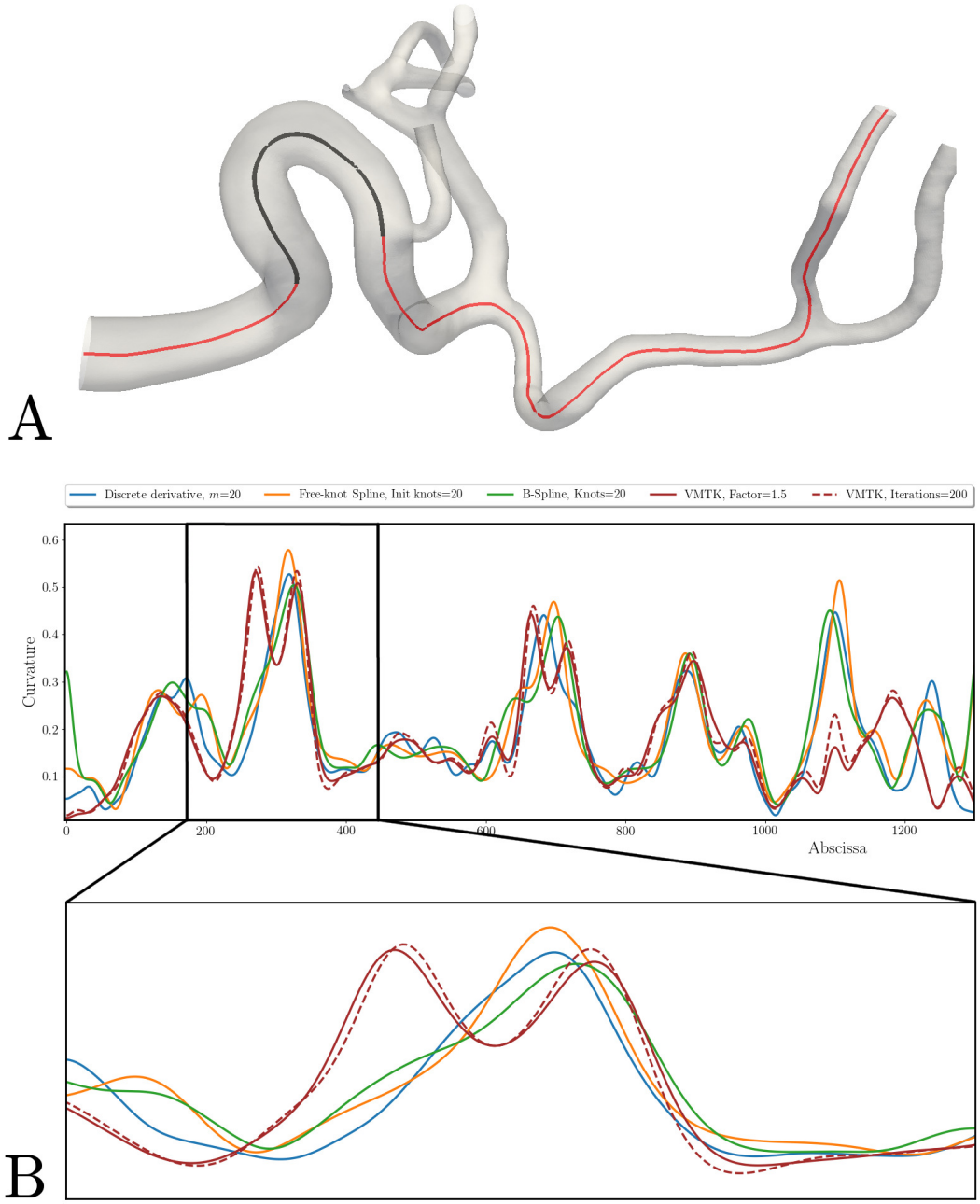

Figure 3.5: **A** The centerline of case P0157 used for curvature comparison in red, including the anterior bend in black. **B** A complete comparison of all the presented methods for curvature computation, using carefully selected parameters for each algorithm, with emphasis of the anterior bend below.

Method	$\kappa_{Initial}$	κ_{New}	$\Delta\kappa$
VMTK, Factor: 1.5	0.450±0.108	0.433±0.124	-0.017
VMTK, Iterations: 200	0.439±0.099	0.433±0.124	-0.005
B-splines, Knots=20	0.496±0.086	0.486±0.096	-0.009
Free-Knot Splines, Knots=20	0.444±0.085	0.463±0.116	0.020
Discrete Derivatives, m=20	0.397±0.069	0.430±0.067	0.033

Table 3.1: Peak curvature values within the anterior bend, mean ± SD for increased curvature.

Method	$\kappa_{Initial}$	κ_{New}	$\Delta\kappa$
VMTK, Factor: 1.5	0.450±0.108	0.354±0.094	-0.096
VMTK, Iterations: 200	0.439±0.099	0.354±0.094	-0.085
B-splines - Knots=20	0.496±0.086	0.329±0.088	-0.167
Free-Knot Splines, Knots=20	0.444±0.085	0.321±0.076	-0.122
Discrete Derivatives, m=20	0.397±0.069	0.324±0.064	-0.073

Table 3.2: Peak curvature values within the anterior bend, mean ± SD for decresed curvature.

4. Landmarking of the Internal Carotid Artery

High peak curvature, and a narrow angle in the anterior bend of the internal carotid artery (ICA) has been shown to be statistically correlated with the presence of aneurysms. Therefore, we need an objective method for identifying the anterior bend segment, before we can perform manipulation of the geometry. An objective subdivision of the ICA into bends can be achieved by identifying the different segments of the ICA, referred to as landmarking of the ICA. The goal of this chapter is to present a framework for an objective landmarking of the ICA siphon. We will be implementing two methods for automatic landmarking of the ICA. Both methods require the ICA centerline as input, followed by estimation of curvature and torsion. Regrettably, estimation of geometric features of the centerline is not addressed by the authors who described landmarking of the ICA, which require us to apply and compare the smoothing techniques from Chapter 3. With a sufficiently smooth centerline, segments are detected based on geometric properties of the centerline. Landmarking of the ICA allows for comparison of patient-specific carotid siphons. Analysis of the variability in the carotid siphon may enable us to identify specific geometric risk factors in correlation to aneurysm initiation.

With a reproducible and scalable method for automatic detection of specific segments, we can manipulate specific morphology of the ICA, as proposed in the goal of this thesis. Using the manipulated geometries, CFD simulations can be performed in order to study hemodynamic stimuli at the terminus bifurcation of the ICA. The results can provide insight into the possible association between hemodynamic stimuli, and aneurysm initiation.

Landmarking of the carotid siphon has its origin in the paper by Ficher (1938), where the segments of the ICA were defined based on its angiographic course [42]. In the following years, several classifications of the ICA have since been proposed. Nowadays the classification by Bouthilier et al., which includes the entire ICA, is the most commonly used classification [43]. The majority of methods for geometric characterization of arteries represents the vessel

shape with a set of geometric indices. Apart from limiting characterization to a set of geometric features, the current state-of-the-art methods require user-interaction. Thus we are motivated to implement a robust and fully automated landmarking pipeline. In this thesis, we will be implementing two methods for automatic landmarking of the ICA.

The first method presented was introduced by Piccinelli et al. (2011) and is an intuitive way of identifying each bend, based on the mathematical concepts of curvature and torsion [23]. Because of anatomic differences among the cases, there are variations in the number of curvature and torsion maximum, consequently varying the number of bends.

A second approach was proposed by Bogunović et al. (2012). With a more anatomical division in mind, the siphon is consequently divided as a sequence of four bends, based on angles formed by a curvature vector expressed in a parallel transport frame [34]. In addition to finding the interface, the method proceeds to identify the centers of the bend, for an additional four landmarks. However, only the interfaces are relevant for our purpose.

4.1 Method

Prior to landmarking, the reconstructed centerline may be a rough estimation, and requires smoothing. In particular, the second and third order derivatives are needed in the computation of the curvature and torsion. Different methods for smoothing the centerline were presented in Chapter 3. In this chapter, we will apply all the proposed methods with the optimal smoothing parameters. With an adequately smoothed curve and derivatives, we can perform automatic subdivision of the ICA into individual siphon bends.

4.1.1 The Fernet-Serret Frame

The geometry of the reconstructed models is analyzed using the approach described by Piccinelli et al. (2009) [36], where the Fernet-Serret frame is introduced for an intrinsic description of the local geometry. The Fernet-Serret formulas describe the kinematic properties of a particle moving along a curve Γ in $\mathbb{R}^3$ parametrized by the normalized arc length parameter t,

$$\mathbf{r}(t) = (x(t), y(t), z(t)) \qquad t \in [0, 1]. \tag{4.1}$$

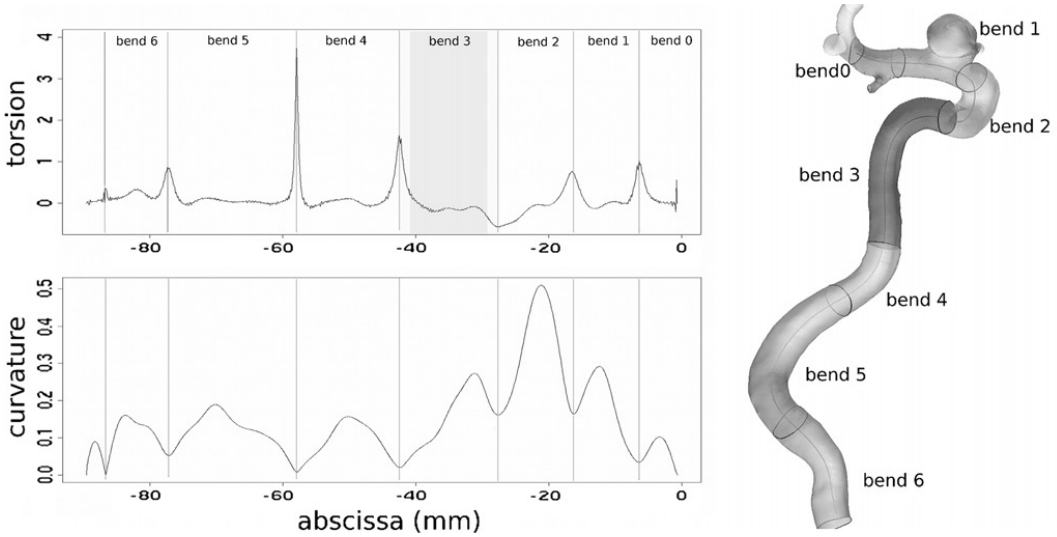

Figure 4.1: Landmarking as presented by Piccinelli et al. with the following caption: "Subdivision of the internal carotid artery siphon in bends. Each bend is identified by a curvature peak and is delimited by 2 enclosing (proximal and distal) torsion peaks. For bend 3, the regions of the definition of the bend-torsion ratio are highlighted: the inner part of the bend (gray) and the 2 boundary regions close to the torsion peaks (light gray), set to 10% of the bend length. Right, subdivision of the siphon centerline in bends applied to the corresponding 3-dimensional model."

The frame consists of the tangent vector $\mathbf{T}$, normal vector $\mathbf{N}$, and binormal unit vector $\mathbf{B}$, defined as

$$\mathbf{T}(t) = \mathbf{r}'(t), \tag{4.2}$$

$$\mathbf{N}(t) = \frac{\mathbf{T}'(t)}{\|\mathbf{T}'(t)\|} = \frac{\mathbf{r}''(t)}{\|\mathbf{r}''(t)\|}, \tag{4.3}$$

$$\mathbf{B}(t) = \mathbf{N}(t) \times \mathbf{T}(t) = \frac{\mathbf{r}'(t) \times \mathbf{r}''(t)}{\|\mathbf{r}'(t) \times \mathbf{r}''(t)\|}. \tag{4.4}$$

4.1.2 Approach Following Piccinelli et al.

Piccinelli et al. use curvature and torsion to determine the bends of the ICA. The subdivision is performed by identifying the location of curvature and torsion peaks along the siphon [23]. By identifying curvature and torsion peaks along the siphon, a bend is defined for each curvature peak bounded by two enclosing torsion peaks as shown in Figure 4.1, including a successfully landmarked model.

Regrettably, there are certain issues using this method as the torsion profile is very sensitive to the amount of noise of the centerline, since it requires the third order derivative of the curve. This implies that the number of bends generated depends both on the length of the centerline, and the degree of smoothness of the centerline and its derivatives. Thus, a challenge arises when choosing between smoothing methods, as well as the amount of smoothing, as no particular technique is specified in the paper.

4.1.3 Approach Following Bogunović et al.

Bogunović et al. aims to provide an objective, robust, and automated framework for landmarking of the ICA, which guarantees correspondence of the bends [34]. The approach divides the ICA into four bends: superior, anterior, posterior and inferior, along the artery upstream direction from the ICA terminal bifurcation, as illustrated in Figure 4.2.

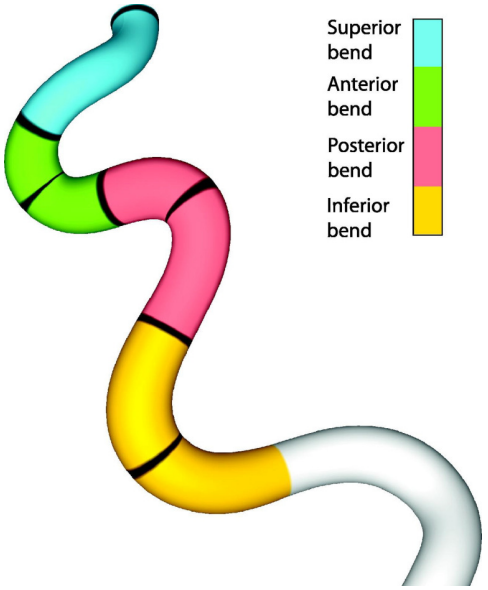

Figure 4.2: Landmarking by Bogunović et al. (2012), with the caption: "Carotid siphon with the four bends (in color) and the seven landmarks (in black). White area denotes: outside the region of interest."

The bends are located along the centerline, where the center and interfaces between them are identified. Bends are separated by a local curvature minimum at their ends. However, the number of curvature extrema may vary across the population. Thus, bends are detected from the trajectory of the curvature vector, which is expressed in the parallel transport frame presented by Bishop (1975) [44], in combination with the Fernet-Serret frame. The curvature vector $\mathbf{T}'(t)$ is defined as

$$\mathbf{T}'(t) = \kappa(t)\mathbf{N}(t) = k_1(t)\mathbf{E}_1(t) + k_2(t)\mathbf{E}_2(t), \tag{4.5}$$

where $\kappa(t)$ is the scalar curvature, and k_1 and k_2 are the components of $\mathbf{T}'(t)$, with respect to the orthonormal basis $\{\mathbf{E}_1, \mathbf{E}_2\}$. Thus we avoid computation of torsion. Using splines to estimate the geometric features will consequently only require the splines to be twice continuously differentiable. Thus the representation is more stable and robust to centerline noise.

The representation of the curvature vector in the (k_1, k_2) space has the property of changing orientation at bend transitions. Thus the ICA is landmarked by detecting bend transitions based on local curvature maximums which create a large angle between their vectors.

4.1.4 Selection of Smoothing Parameters

Estimation of curvature and torsion was introduced in Chapter 4, and in this chapter, we will present results where all methods have been implemented. However, each method relies on one or multiple input parameters.

The integrated method in VMTK required two parameters; the number of smoothing iterations, and the smoothing factor. In addition, there was the option to resample the centerline, which relied on a resampling length. Landmarking was performed using a number of smoothing iterations, and a smoothing factor provided by Piccinelli, subsequent of the landmarking article, whereas a resampling step of 0.2-0.3 mm was found to produce the most optimal landmarking.

Centerline smoothing using B-splines relied on a polynomial degree and the number of knots. Splines were only applied to the landmarking procedure of Bogunović et al. Thus, we require the splines to be of polynomial degree 2, in order to compute curvature. Setting an appropriate number of uniform knots was initially performed by trial and error. Using a large number of knots would only lead to instabilities, as shown in Chapter 3, which would affect the amount of curvature and torsion extremum along the curve, and furthermore segment the siphon at improbable locations. Through several investigations, we observed a correlation between the length of the carotid siphon centerline, and the observed number of optimal knots across all cases. Thus the following relation between the number of knots and length of the carotid siphon was proposed, by linear regression,

$$\text{Number of knots} = \left\lceil \frac{\mathfrak{L}}{20} + \frac{26}{3} \right\rceil, \tag{4.6}$$

where $\mathfrak{L}$ is the length of the centerline, and $\lceil \cdot \rceil$ is the ceiling function. Equation (4.6) determines the relative number of knots for a given case. A comparison between using the relative number of knots, and a constant number of knots was performed during the landmarking.

The method of free knot regression splines relied on the number of initial knots [40]. In the following results, our implementation selected the number

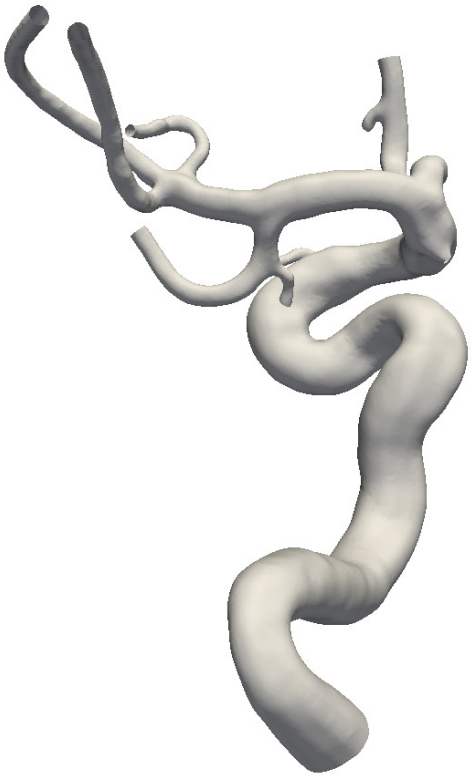

Figure 4.3: A healthy model of the ICA, case P0134.

of initial knots based on the relative number of knots formula, considering the relation was constructed for splines.

Finally, the method of discrete derivatives depends on the radius of the sliding neighborhood, m. As previously shown, we can expect convergence for this method using $m \geq 20$. Therefore, we let the input radius for landmarking be $m = 20$.

In the following results, the landmarking was performed on ten healthy patient-specific cases from the Aneurisk database [45], with an example of a healthy model illustrated in Figure 4.3. Centerlines were successfully extracted for each case, before undergoing a smoothing procedure, using one of the proposed methods. Detection of landmarks was subsequently performed, based on the proposed method by Bogunović et al. and Piccinelli et al.

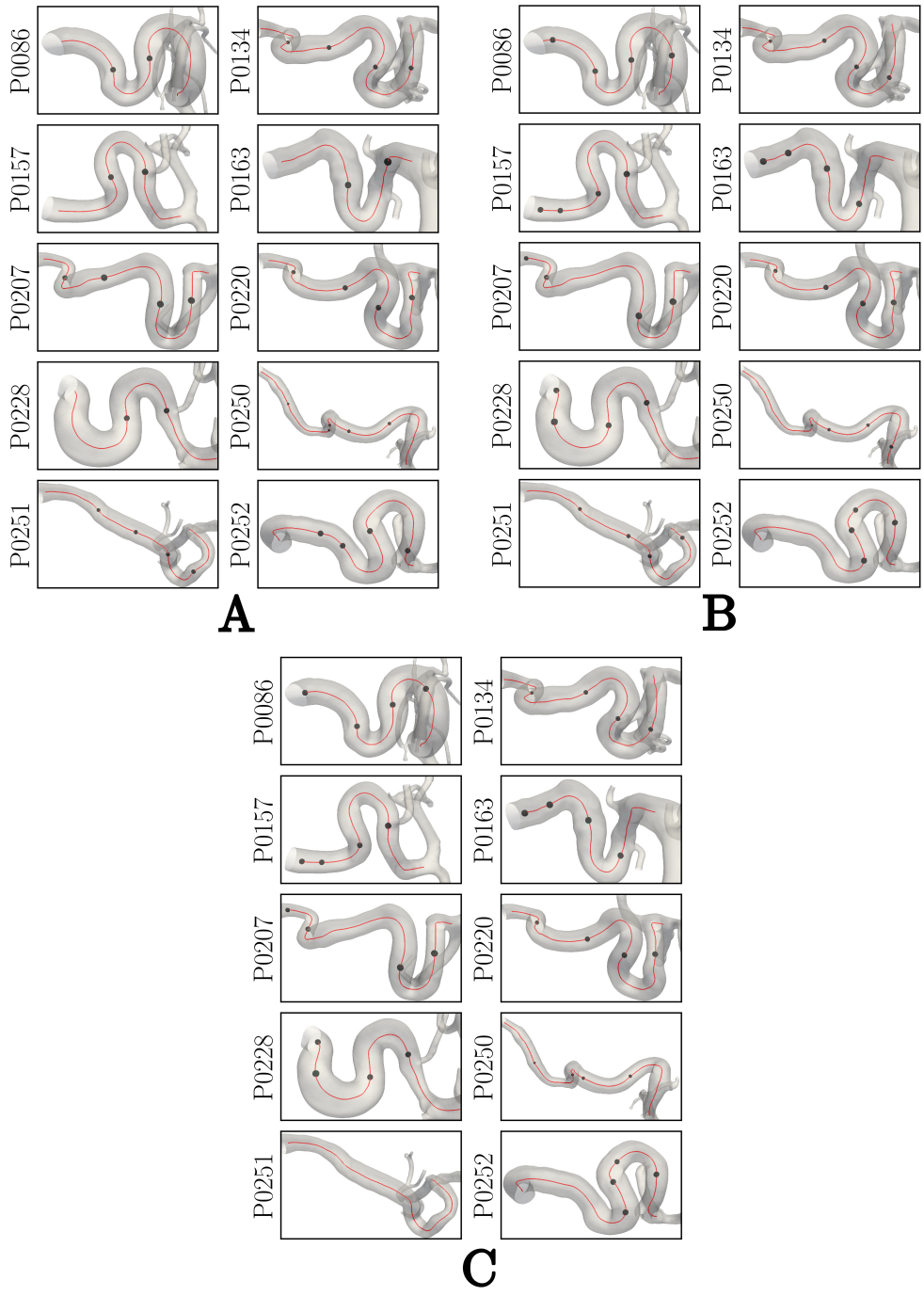

Figure 4.4: **A** Result of Piccinelli's method using the optimal resampling length for each case. **B** Result of Bogunović's method using the relative number of knots. **C** Result using Bogunović's method using a constant number of knots, set to 11. Notice in particular how 11 knots was not enough to landmark the geometry of case P0251.

4.2 Results

First off, we consider the landmarking using the method proposed by Piccinelli et al., presented in Figure 4.4 **A**. Piccinelli's method shows inconsistent results, even though it adapts to the geometry's length by introducing additional or reducing the number of bends along the centerline. We are especially interested in the two interfaces proximal to the ICA terminus, which defines the anterior bend, recognized by its characteristic bend upstream of the ICA terminus. However, the points proximal to the ICA terminus are generally not favorable for our purpose, with the worst-case represented in case P0086 and P0250. Although Piccinelli et al. reported an average of five bends per case, we observe six cases with four bends, and four cases with two bends.

For the landmarking method described by Bogunović et al., we present the main results in Figure 4.4 **B**. It appears that Bogunović's method is generally more reliable in comparison to Piccinelli's method. With the exception of case P0252, the landmarking using Bogunović's method results in an adequate landmarking of the siphon, regardless of the geometry's length.

To ensure that the proposed relation between the number of knots, and the length of the carotid siphon centerline produced the optimal landmarking, using the relative number of knots for landmarking was compared with landmarking using a constant number of knots. A total of 11 knots were used across all cases, resulting in the segmentation shown in Figure 4.4 **C**. By studying the different cases, it appears that only the cases P0086, P0250 and P0251 were affected. In P0086 the region of the anterior bend appears shorter, while the interfaces in case P0250 are driven further upstream, in comparison to the landmarking using the relative number of knots. It should be specially noticed that the landmarking points in case P0251 are missing, which means the algorithm failed. As stated by the algorithm, the fault is caused by the centerline being too short to be classified into four bends.

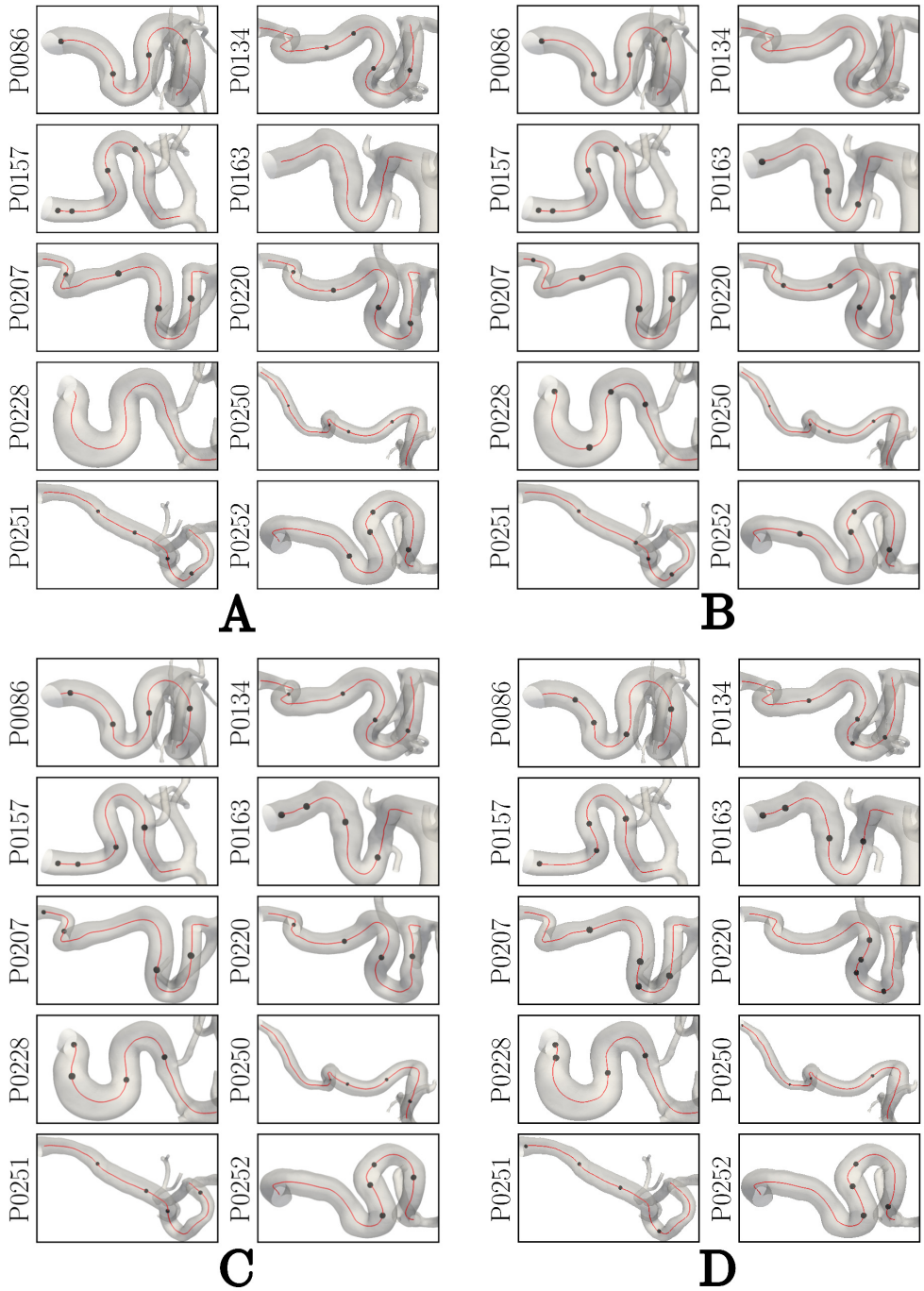

Figure 4.5: Results using Bogunović's method using the following methods for centerline smoothing: **A** Smoothing in VMTK and curvature computation using discrete derivatives, with a radius of the sliding neighborhood set to 20. **B** Discrete derivatives, with a radius of the sliding neighborhood set to 20. **C** B-splines with the relative number of knots. **D** Free knot spline regression, using the relative number of knots as number of initial knots.

Results from the implementation of discrete derivatives used in the landmarking algorithm by Bogunović et al., is shown in Figure 4.5 **A** and **B**. For comparison, we include the landmarking where splines with the relative number of knots were used, shown in Figure 4.5 **C**. Although the initial implementation of discrete derivatives by Lauric et al. was intended for curvature measurement in the carotid siphon, the procedure generally appears robust for landmarking. In Figure 4.5 **A** we performed a combination of smoothing the centerline using VMTK, followed by curvature estimation using discrete derivatives. The algorithm is unsuccessful for case P0163 and P0228, but produces sufficient results otherwise, except for case P0250, where the interface is driven too far upstream. The results shown in Figure 4.5 **B** uses discrete derivatives explicitly. Landmarking is unsuccessful for P0134, and the interfaces of P0250 is suboptimal. Excluding these exceptions, the landmarking using discrete derivatives is generally adequate, although the interfaces of P0163 are arguably too close.

The method of free knot spline regression produced the results presented in Figure 4.5 **D**. Although the algorithm successfully landmarks all cases, the position of the interfaces are often skewed in comparison to Bogunović's method using the relative number of knots. In particular, the landmarking of case P0250 and P0251 does not capture the anterior bend, which is of interest.

4.3 Discussion

The goal of this chapter was implementing and comparing algorithms for automated detection of vessel bends, and landmarking of the ICA, using computationally generated centerlines in the ICA smoothed using one of the proposed smoothing techniques.

4.3.1 Smoothing Input Parameters

The methods for estimation of curvature and torsion relied on one or multiple input parameters. In addition, we considered a smoothing technique only applicable for landmarking.

The integrated method in VMTK required three parameters; the number of smoothing iterations, the smoothing factor, and a resampling length. In the presented landmarking, a constant smoothing factor and number of iterations were provided, while the resampling length was varied. Multiple computations of the centerline seemed to show a trend where small resampling steps eventually produced a surplus of segments along the line and vice versa using larger steps. Hence the most optimal results among ten cases ended up using a resampling step of 0.2-0.3 mm.

An additional smoothing technique only applicable for landmarking was based on extensively smoothing the surface of each case, motivated by the Laplacian over-smoothing applied to the surfaces presented by Bogunović et al. Extensive smoothing of the initial Voronoi diagram should, in theory, generate a smoother surface, and consequently a smoother centerline. The smoothing was performed by computing the Voronoi diagram of the model, followed by smoothing the Voronoi diagram based on a given smoothing factor as the input parameter. This factor determined which points from the initial Voronoi diagram to be carried over to the new, and smooth diagram. Having generated a new diagram, a smoothed version of the surface was reconstructed. Finally, the centerline to be landmarked was computed from the reconstructed surface, and used directly in Bogunović's method. Even though this procedure was only tested for two cases, with smoothing factors ranging from 0.01 to 0.25, the general trend was that the points clustered up together, somewhere along the anterior bend. Due to the amount of noise in the computed centerline, an unreasonable number of torsion and curvature maximum were calculated, consequently producing unsatisfactory results during landmarking.

4.3.2 Resampling of the Centerline

With resampling being introduced for the integrated method in VMTK, we were urged to investigate the effect of resampling in combination with the method of splines. Though the initial sampling of the centerline was not generally a problem during landmarking along the curve, it could potentially have an impact on the part of the algorithm which performed detection of curvature saddle points, consequently leading to different landmarks.

Using resampling steps of 0.1, 0.3, and 0.5 mm, the landmarking method proposed by Bogunović et al. produced the landmarks presented in Figure 4.6. To further ensure that using the relative number of knots was optimal, an additional landmarking using a constant number of knots was performed, with a resampling step of 0.1 mm. The results in Figure 4.6 **A** using a constant number of knots, set to 11, are relatively similar to those presented in Figure 4.4 **B**. Cases P0086, P0220, and P0250 are affected negatively, with case P0251 being the exception of not passing the algorithm.

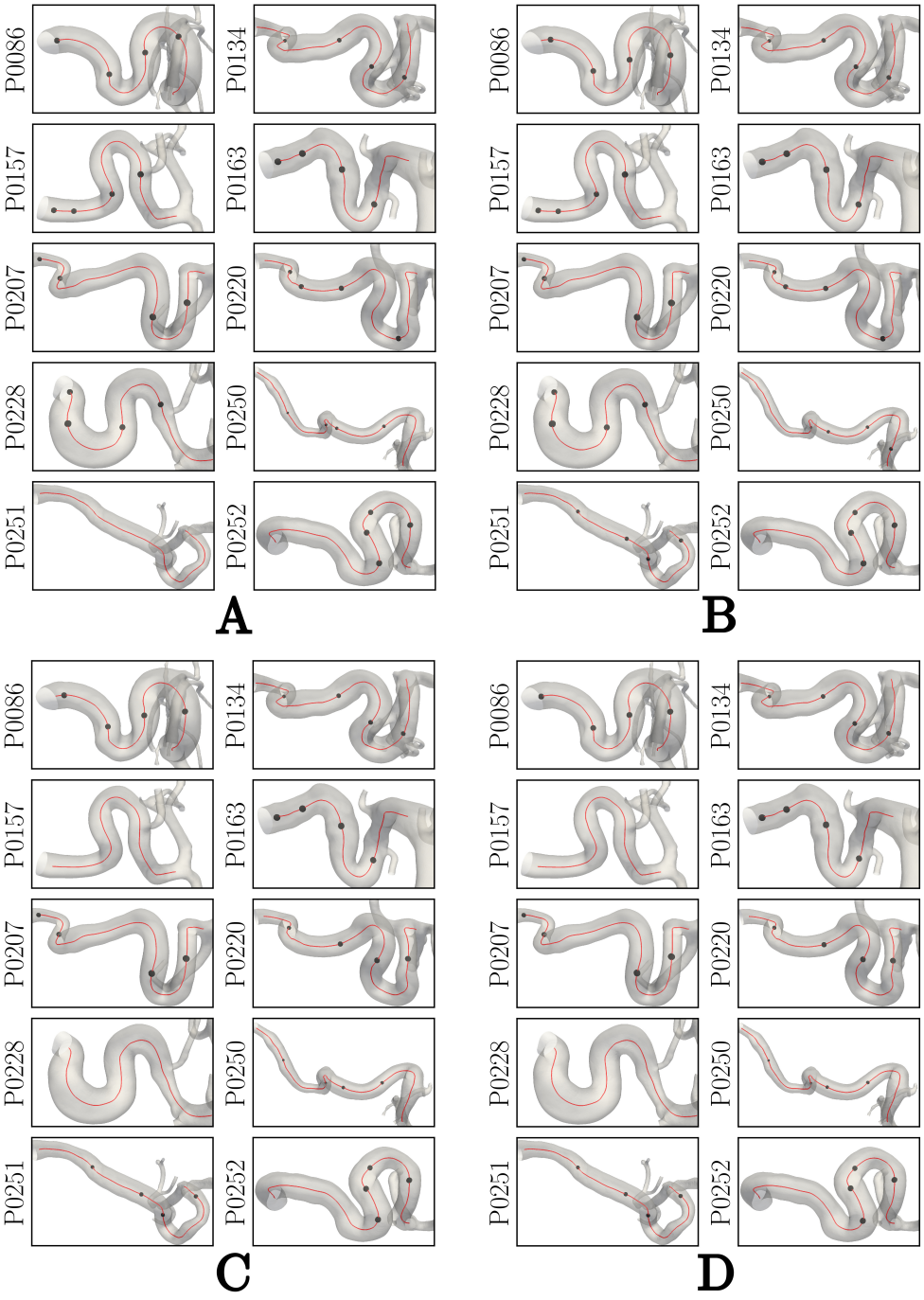

Figure 4.6: Results using Bogunović's method with the following input parameters: **A** Resampling step of 0.1 and 11 knots for spline computation. **B** Resampling step of 0.1 and the relative number of knots. **C** Resampling step of 0.3 and the relative number of knots. **D** Resampling step of 0.5 and the relative number of knots.

Figure 4.6 **B** presents landmarks by Bogunović's method, using a resampling step of 0.1 mm, but varying number of knots. There are no visible changes compared to the non-resampling method in Figure 4.4 **B**, except for case P0220 which presents an undesired landmarking. Figure 4.6 **C** and **D** presents the results for larger values of the resampling step, namely 0.3 and 0.5. The results using larger resampling steps show the vulnerability of the algorithm for under-sampled centerlines, whereas the algorithm fails for case P0157 and P0228. Compared with Bogunović's method with no resampling, only case P0250 appears noticeably different for resampling steps equal to 0.3 and 0.5, while case P0220 is affected when using 0.1 as resampling step.

4.3.3 Landmarking of the Internal Carotid Artery

Direct implementation of the landmarking method by Piccinelli et al. was not a suitable method as it does not produce correspondence among siphon segments, and the results are too sensitive based on the smoothing procedure. The presented results applied resampling using carefully selected resampling steps in order to obtain an optimal landmarking of the ICA. An earlier proposed smoothing technique was splines, in combination with Piccinelli's approach. However, due to the algorithm's sensitivity to the number of knots, the results were not applicable for our purposes and thus not included in the report.

The landmarking results using the method by Bogunović et al. provided adequate results. The disadvantage of the method is the potential failure in short geometries, or in geometries where the centerline has been resampled into few intervals, as shown in the landmarking which applied resampling of the centerline. An explanation for why the algorithm failed is the assumption that all ICAs can be subdivided into four bends. If the landmarking perceives two neighboring bends as one larger bend, the algorithm fails. Alternatively, the following procedure is proposed in Bogunović's paper:

> *"Apart from the superior bend, the other three bends were modeled as planar. An alternative would be to split the superior bend into two smaller quasi-planar bends, but we observed that those two bends are not consistently present between subjects."*

Furthermore, the validation performed in the study by Bogunović et al. showed that the automatically obtained landmarks were in agreement with the ones selected manually, and that they did not affect the obtained geometric quantities [34].

All cases presented in Figure 4.4 **B** provide adequate landmarking of the ICA, defining the anterior bend used in the geometric manipulation presented in

Chapter 6. The only inconsistency is the location of the upstream anterior-superior interface. In a majority of the cases this interface is placed about halfway between the curvature peak of the anterior bend, and the end of the centerline. For cases P0163 and P0251, this interface is located slightly up- and down-stream, respectively. For improvement, a thorough investigation of the optimal number of initial knots should be performed, whereas our implementation based the selection of knots on the relative number of knots formula, presented in Equation (4.6). Nonetheless, the anterior bend is sufficiently landmarked.

Construction of an automated approach for landmarking provides us with a generalized algorithm which enables high reproducibility among a set of patient-specific geometries, essential for performing larger cohort studies. Although the framework is implemented with the ICA in mind, the algorithm can be adapted to other vascular bends. However, application to other vessels or tubular structures might result in an inconsistent number of bends, or type of bends, considering the algorithm is meant for landmarking of the ICA. Nonetheless, by following the approach presented by Bogunović et al. we successfully managed to segment the ICA into reasonable segments, applicable for our purposes throughout the geometric manipulation.

4.4 Conclusion

The results, and the following discussion shows how the approach presented by Bogunović et al. in combination with B-splines for centerline smoothing is the most reliable method for landmarking of the ICA. The method is consistent, independent of geometric attributes, and produces the most realistic landmarking, with satisfactory results for our purposes. Therefore we will proceed by using the landmarking algorithm presented by Bogunović et al., in combination with B-splines and the relative number of knots, for geometric manipulation.

Future work includes performing a larger cohort study with landmarks defined by clinicians in advance, in order to validate the method proposed by Bogunović et al.

5. Automated Measurement of the Anterior Bend Angle

High peak curvature and a narrow angle of the anterior bend of the internal carotid artery (ICA) are morphologic features shown to be statistically correlated with the presence of aneurysms. In Chapter 3 we presented methods for measuring the curvature, followed by Chapter 4 where we performed landmarking of the ICA, to identify the anterior bend. Having identified the anterior bend, we can perform geometric manipulations in order to adjust the bend angle. However, this requires an objective method for measuring the angle of the anterior bend. The goal of this chapter is to present and compare methods for measurement of the anterior bend angle, also referred to as the carotid siphon angle, located in the cavernous segment of the ICA.

Silva et al. have previously shown that narrow angles of the anterior bend are statistically linked with the formation of aneurysms, concluding that narrow angles may influence the hemodynamic stress [22]. In addition, Waihrich et al. performed angle measurements in the same region and showed there was a significant independent direct relation between the anterior bend angle, and aneurysms located distal to the carotid siphon [46].

5.1 Background

Silva et al. and Waihrich et al. performed manual angle measurements from two-dimensional lateral view angiographic images. Angle measurement in both studies were based on the angle at the intersection of two straight lines traced through the midpoints of the diameter of each straight segment of the siphon. The straight segments include the (horizontal) intracavernous and the supraclinoid segment of the carotid siphon, as illustrated in Figure 5.1, whereas Waihrich et al. included additional measurements in the vertical intracavernous segment and the petrous segment, as shown in Figure 5.2. Waihrich et al. specified that the lateral view was at the same level as the external acoustic meatus, while Silva et al. specified that the *Image J Version 1.42p* program was used to draw the straight lines.

Although the procedures of angle measurement were similar, the purpose and application differed between the articles. Silva et al. studied effects of bend angle in correlation to aneurysm initiation, between 169 patients with cerebral aneurysms and a control group consisting of 256 healthy individuals. Waihrich et al. studied the correlation between bend angle and aneurysm rupture, where the study consisted of a total of 640 patients, and a total of 692 cerebral aneurysms, with 225 and 467, ruptured and unruptured, respectively.

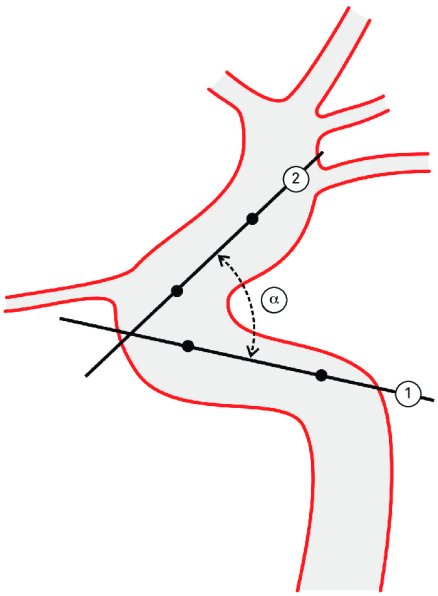

Figure 5.1: Method for anterior bend angle measurement presented by Silva et al. [22], with the following caption: "Carotid siphon angle (α) formed by the intersection of two lines traced from intracavernous (1) and supraclinoid (2) points through the artery."

5.2 Method

5.2.1 Measuring the Anterior Bend Angle

As Silva et al. admit, the measurement procedure may be biased and of little reproducibility. Therefore, we tried to construct a more general and robust method for angle measurement. Our general approach for measuring the angle was by expressing two lines as vectors, starting from the clipping points, as defined by the landmarking method by Bogunović et al., and passing through the tracing points along the siphon centerline. An illustration of this procedure is shown in Figure 5.3, where we denote the lines as $\mathbf{a}$ and $\mathbf{b}$.

The angle, θ, was measured at the intersection of these straight lines, represented as vectors in $\mathbb{R}^3$, by the classical formula

$$\theta = \arccos\left(\frac{\langle \mathbf{a}, \mathbf{b} \rangle}{\|\mathbf{a}\|\|\mathbf{b}\|}\right),$$

where $\|\cdot\|$ is the norm and $\langle \cdot, \cdot \rangle$ is the inner product in Euclidean space. Thus it remains to discuss possible procedures to measure the anterior bend angle using only the clipping points and the carotid siphon centerline as input. In addition, we will perform a comparison, and try to replicate the methods

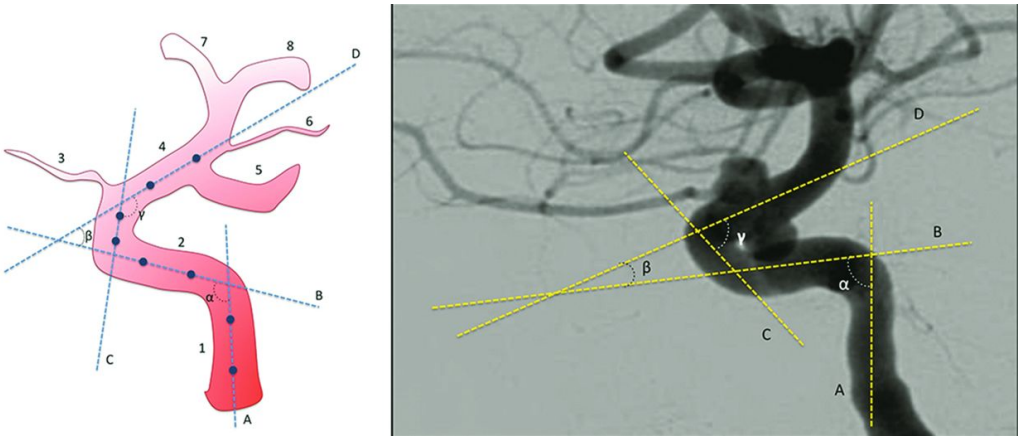

Figure 5.2: Method for anterior bend angle measurement following Waihrich et al. [46]. On the left, an illustration of a carotid siphon with lines traced to cross the midpoints of the diameters of the straight segments of the siphon. On the right, an example of an actual measurement process.

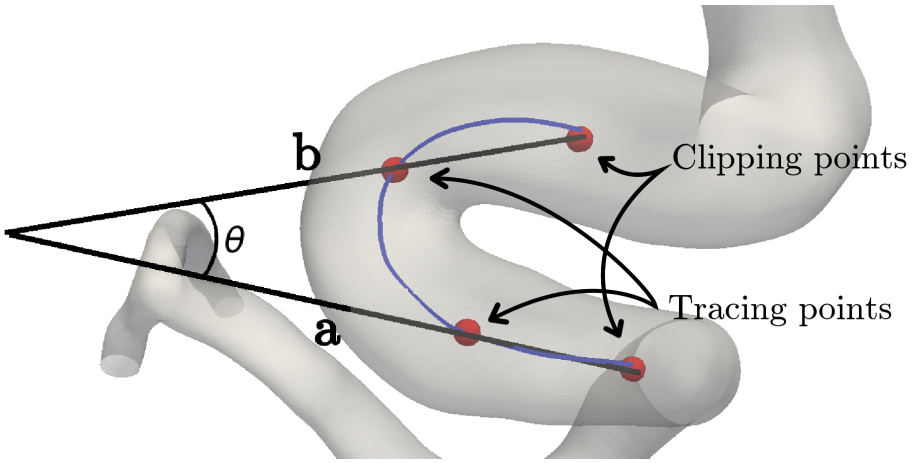

Figure 5.3: Anterior bend angle (θ) formed by the intersection of two lines starting from each clipping point traced through the tracing points.

presented in the literature, with the intention of presenting a more robust and reproducible method for angle measurement.

It should be noted that the carotid siphon is characterized as one of four type of shapes; a V-shape, a U-shape, a C-shape, and a S-shape. An illustration of the different shapes is shown in Figure 5.4. However, the shape of the artery was not taken into consideration throughout the angle measurements, neither in this study nor the measurements by Silva et al., or Waihrich et al.

In addition, the angle measurements presented in both papers were performed

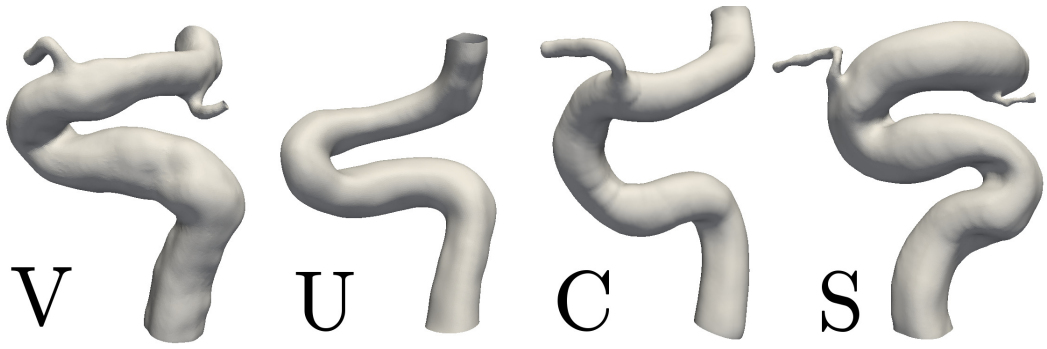

Figure 5.4: The four shape characteristics of the anterior bend of the ICA; V, U, C and S.

in a two-dimensional plane, in comparison to our three-dimensional measurements.

In total, we have proposed six different methods for measuring angles, which we will compare against the literature and manual measurements.

5.2.2 Orthogonal Distance Regression

In order to reproduce the method presented in the two articles, we would need to find the lines which approximate the cavernous and supraclinoid segment of the ICA. To approximate these lines, we applied the method of orthogonal distance regression (ODR), a line fitting technique in 3D. The points to be fitted were selected based on curvature profiles of the carotid siphon centerline using one of two suggested termination criteria. For estimation of curvature, we applied B-splines using the relative number of knots, as ODR relied on the clipping points from landmarking.

The first approach iterated though points along the centerline up- and downstream starting at the two clipping points, until the cumulative curvature reached a selected cumulative limit. A visualization of this method is shown in Figure **??** **A** and **B**, for a successful, and unsuccessful measurement, respectively.

A second approach performed a similar iteration, but included the 10 neighboring points around each clipping point before proceeding with iteration. Using this approach the limit was defined as the upper endpoint of the 95% confidence interval, using the mean curvature of 11 points surrounding, and

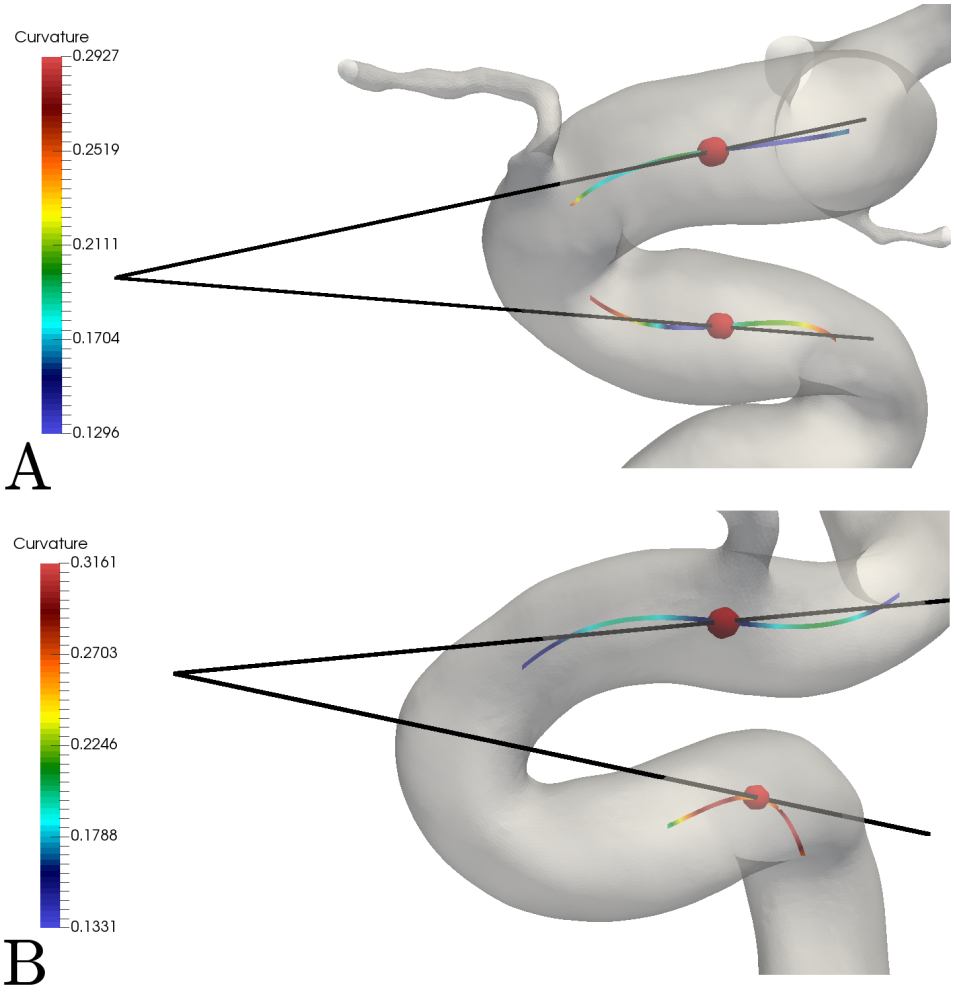

Figure 5.5: Method for anterior bend angle measurement based on orthogonal distance regression. **A** Successful approximation of the straight segment of the carotid siphon in case P0086, using the cumulative curvature as criteria. **B** Unsuccessful approximation of the straight segment of the carotid siphon in case P0157, using the cumulative curvature as criteria.

including the clipping point,

$$\text{Limit} = \frac{1}{11}\sum_{i=-5}^{5}\kappa_i + \text{SD} \times 1.96, \tag{5.1}$$

where κ_0 corresponds to the curvature at the clipping point, and SD $= 0.045$ mm^{-1} is the standard deviation from [22]. This constructs a limit which is based on the concept of a confidence interval, such that in 95% of the curvature measurements will be below this limit.

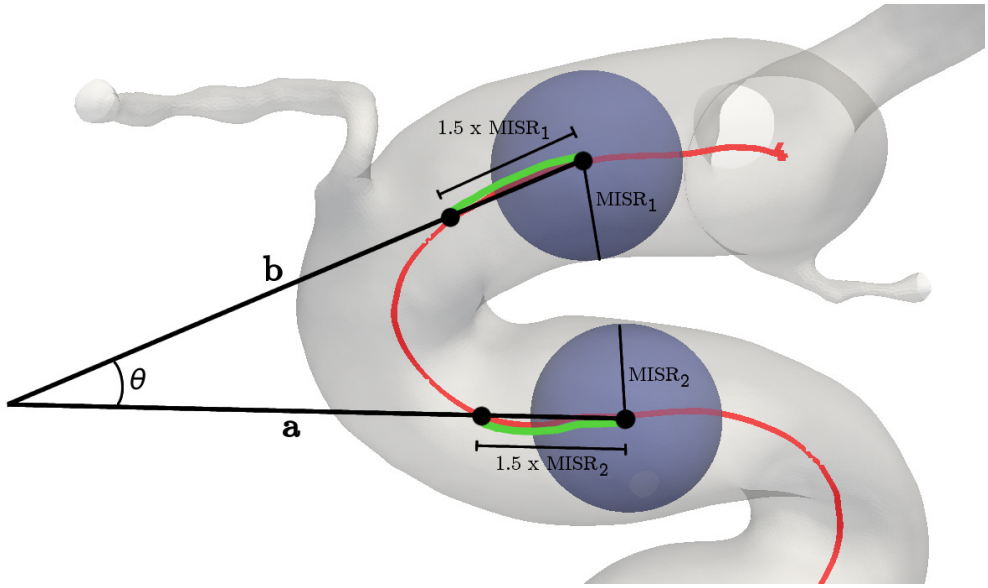

Figure 5.6: Selection of points based on the maximum inscribed siphere radius (MISR).

5.2.3 Tracing Point Methods

5.2.3.1 Maximum Inscribed Sphere Radius

Instead of approximating the straight segments using a line fitting technique, we now propose possible selection of the tracing points along the centerline. One approach was placing the tracing points a specific distance along the centerline based on the maximum inscribed sphere radius (MISR) at the clippings points, as shown in Figure 5.6.

5.2.3.2 Fractional Centerline Distance

Another method for selecting the tracing points was based on fractional distances along the centerline. We performed measurements using a pair of five different fractional distances along the centerline: ⅓ and ⅔, ⅕ and ⅘, ⅐ and ⅙, ⅖ and ⅗, and ⅔ and ⅚. In addition, the pairs of fractional distances were applied to several of the angle measurement methods presented in this chapter. However, this approach did not consider how the clipping points were positioned relative to each other, and the middle of the siphon was selected as the midpoint of the clipping points.

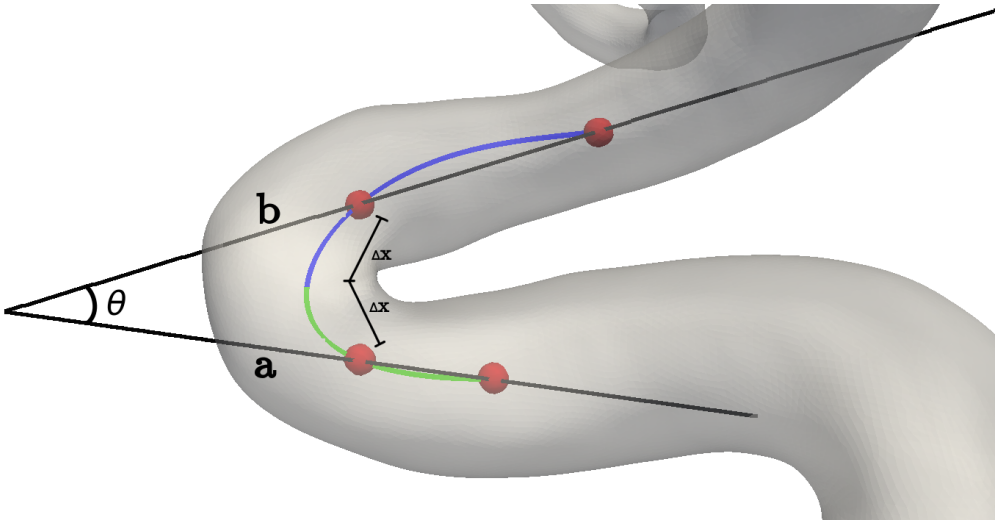

Figure 5.7: Anterior bend angle (θ) formed by the intersection of two lines starting from each clipping point through two symmetricly place points along the siphon.

5.2.4 Relative Tracing Point Methods

5.2.4.1 Midpoint Selection from Peak Curvature

In this approach, the middle of the siphon was selected as the location of peak curvature. This could either be defined as the maximum curvature value along an unsmoothed curvature profile, or as the single curvature peak of an over-smoothed curvature profile using a Gaussian filter, in case the siphon initially consisted of multiple curvature peaks. For comparison, curvature profiles were generated through both the method of B-splines and discrete derivatives. Based on the new midpoint, the tracing points were selected as fractional differences of the green and blue curves shown in Figure 5.7.

The tracing points were selected by two approaches. One approach was based on fractional distances along each of the two distinct curves. An alternative method was selecting one of the two tracing points based on a fractional length of the shortest line, followed by selecting the corresponding point along the longer curve, positioned at the same distance from the midpoint as the first point. An illustration of this "symmetry" procedure is shown in Figure 5.7.

5.2.4.2 Midpoint Selection from Maximal Point Distance

Another proposed approach was selecting the midpoint as the point located most distal to the clipping points. Given any point $\mathbf{p}_i$ along the siphon, and

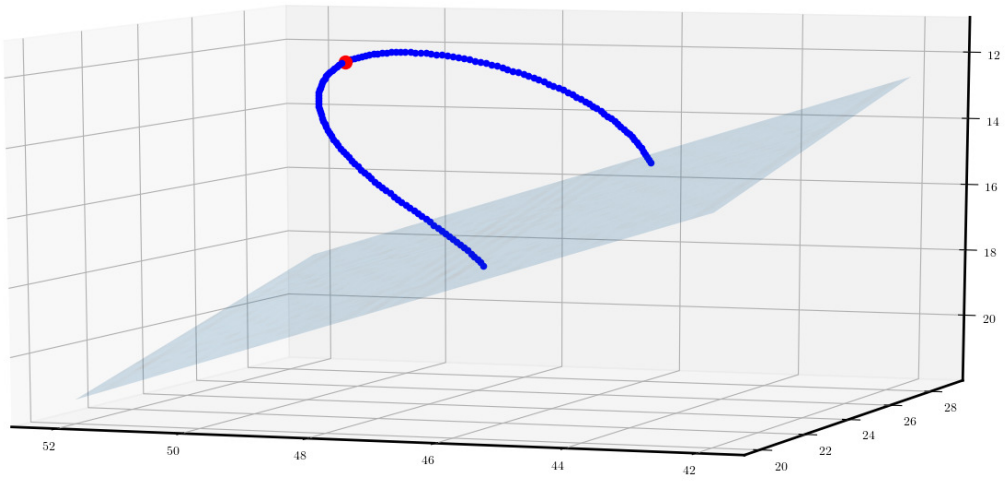

Figure 5.8: Midpoint selection based on the point along the siphon located most distal to the plane going through both clipping points.

clipping points $\mathbf{p}_0$ and $\mathbf{p}_N$, the distances

$$d_{i,1} = \|\mathbf{p}_i - \mathbf{p}_0\|, \qquad d_{i,2} = \|\mathbf{p}_i - \mathbf{p}_N\|, \qquad d_i = d_{i,1}^2 + d_{i,2}^2, \tag{5.2}$$

were computed. Thus the midpoint was set to be the point where $d_M > d_i$ for all $i = 1, \ldots, N, i \neq M$.

5.2.4.3 Midpoint Selection from Maximal Line-Point Distance

An alternative method for selecting the midpoint made use of the line through the clipping points. The midpoint, shown as a red sphere in Figure 5.8, was selected based on the point along the siphon located most distal to the line going through both clipping points. Given the midpoint, we selected fractional distances along each of the two distinct lines to place the two tracing points.

5.2.5 Midpoint Selection from Maximal Fernet Plane-Point Distance

To take into account the position of the clipping points relative to each other, a variation of the previous method was proposed, based on the algorithm shown in Figure 5.9. The method used the direction of the Frenet tangent vector in each of the clipping points as a normal vector, to define two planes perpendicular to the centerline. We proceeded to check where the plane, defined at the first clipping point, intersected the centerline close to the second clipping point, and similarly with the second plane. Intersections located behind the

clipping points relative to the middle of the curve, were treated as if they intersected the line at the clipping point, while intersections in front of the clipping points defined a temporary clipping point. The two intersections defined a vector, and in combination with the Fernet binormal, the cross product of the two vectors defined a third plane. This plane was used to find the midpoint, selected as the point along the siphon located most distal to the plane. Given the midpoint, we proceeded by selecting various fractional distances along each of the two distinct lines for tracing point placement. Placement of the tracing points where performed using either the old clipping points, or the new clipping points, denoted as *Oldclip* and *Newclip* in the results, respectively.

5.2.6 Manual Angle Measurement in *3D Slicer*

Finally, a manual measurement was performed. Two observers (the author and a supervisor) randomly, and blindly selected a total of thirty cases to perform the interobserver reproducibility of the manual measurements, including ten cases comprised of smaller angles, ten cases comprised of larger angles, and the initial ten cases. The manual measurements were executed in the *3D Slicer* tool [47], where we used an improved version of an already existing angle measurement module [48]. It should be noted that the angles were still measured in 3D, and each participant was given the opportunity to select their preferred view of the anterior bend for optimal angle measurement. The angles were measured where two user-selected lines intersected, denoted as a *ruler* in *3D Slicer*. The only guideline for the observers was that the selected points had to lie inside the model, approximately placing them along the centerline. For each measurement, the angle between the lines was measured, and recorded.

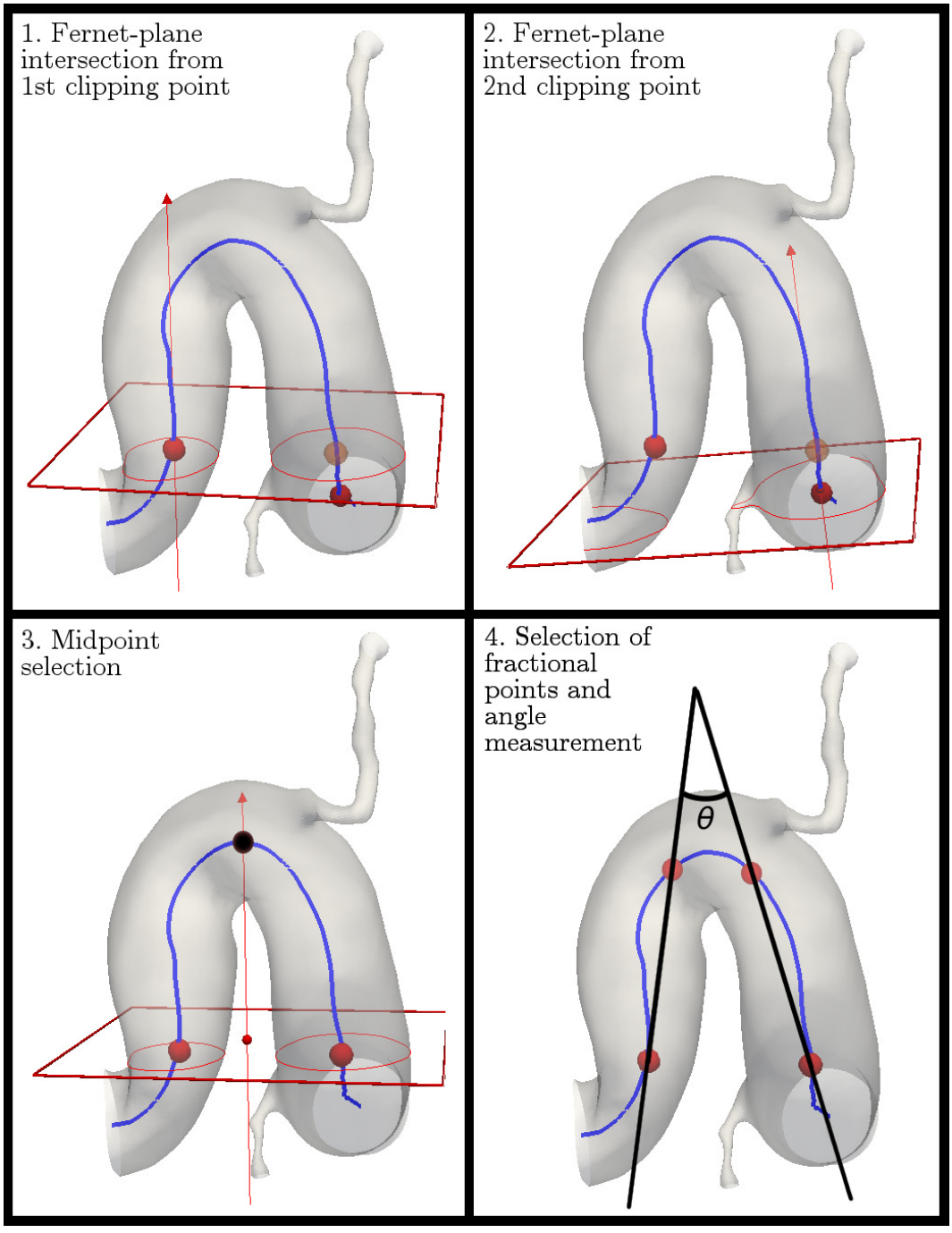

Figure 5.9: Steps of the algorithm used to find the midpoint of the anterior bend based on the maximal Fernet plane-point distance.

Method	Naming convention
Orthogonal distance regression	ODR
Maximum inscribed sphere radius	MISR
Fractional centerline distance	Fraction
Peak curvature of unsmoothed curvature profile, with splines	Max curv
Peak curvature of unsmoothed curvature profile, with discrete derivatives	Discrete
Peak curvature of over-smoothed curvature profile	Oversmooth
Maximum line-point distance	Line
Fernet plane-point distance, with placement of tracing points based on old clipping points	Plane, Oldclip
Fernet plane-point distance, with placement of tracing points based on new clipping points	Plane, Newclip
Manual measurement in *3D Slicer*	Manual

Table 5.3: Naming conventions for the different angle measurement methods.

5.3 Results

We have included visualizations of the procedures for a limited selection of the methods, whereas quantitative results are presented in this section. In Tables 5.5 - 5.8 we have used the naming conventions listed in 5.3 The mean ± SD for angle reference is shown in Table 5.4, presenting the measurements by Silva et al. A complete comparison is listed in Tables 5.5 and 5.7, for increase and decrease in the anterior bend angle, respectively. In addition, a list of the most relevant choices for increase and decrease in angle is shown in Tables 5.6 and 5.8, respectively.

The method of ODR is illustrated in Figure 5.5 **A**, using a successive case, where the contributing points along the centerline have been included with corresponding curvature values. Unfortunately, both approaches fail to produce adequate lines consistently. The first approach relies on selecting a cumulative limit, where both the sampling of the centerline, and the curvature of the neighboring points around the clipping points should be taken into consideration; factors which vary across all cases. Using the same limit for all cases produced successive cases as shown in Figure 5.5 **A**, but also unsuitable lines as shown in Figure 5.5 **B**, possibly explained by the clipping point being located at a curvature saddle point along the centerline. As Figure 5.5 **B** shows, the line through the supraclinoid segment is sufficiently approximated, while the line through the cavernous segment should be generated from a larger sample

Method	$\theta_{Initial}$
Reference (Aneurysm)	26.3±19.1
Reference (No aneurysm)	33.8±22.6

Table 5.4: Mean ± SD for angle reference

of points downstream for an optimal measurement.

Two problems arose by using the second approach with ODR, where the chosen points were delimited by the upper limit of the one-sided 95% confidence interval. First, part of the measurements resulted in an unrealistic amount of points being used for the ODR, as a result of no points surpassing the upper limit. Second, an issue was introduced by initial points being located too close to a curvature extremum, due to saddle points along the curve, which triggered the limit too early.

The procedure and results of a particular case using the MISR method are shown in Figure 5.6. For comparison the distances 1.0×MISR, 1.5×MISR, 2.0×MISR and 2.5×MISR were used. However, as observed in Tables 5.5 and 5.7 the angle difference was generally low, and did not always produce the expected difference in angle.

Using the method of fractional centerline distances, a selection of fractions were tested, as reported in Table 5.5 and 5.7. Here the pair of fractions is denoted by only the first of the two fractions. A similar convention is used for all of the traction point methods.

The remaining traction point methods appear to capture the decrease and increase in anterior bend angle. However, there are substantial differences in the change of angle, $\Delta\theta$. For increase in anterior bend angle, the maximum and minimum changes are $\Delta\theta = 35.77°$ and $\Delta\theta = -2.86°$, respectively. Decreased angle shows slightly less deviation, with a maximum and minimum change in angle of $|\Delta\theta| = 17.04°$ and $|\Delta\theta| = 4.47°$, respectively. Compare to the reference values of Table 5.4, the mean anterior bend angle of our measurements are generally more significant, with an increase of 30-40%. However, the SD of our measurements is of similar magnitude to the reference SD, at approximately 20°.

Method	$\theta_{Initial}$	θ_{New}	$\Delta\theta$
ODR - Cumulative	40.01±20.61	41.98±26.50	1.97
ODR - SD limit	49.74±21.10	44.79±25.47	-4.95
MISR×1.0	45.32±26.70	42.46±27.95	-2.86
MISR×1.5	43.57±24.95	43.48±28.08	-0.09
MISR×2.0	44.20±23.20	45.49±27.84	1.30
MISR×2.5	46.76±23.21	48.59±28.06	1.82
Fraction - 1/3	42.10±17.39	50.37±23.61	8.27
Fraction - 1/5	38.49±18.74	41.61±24.16	3.12
Fraction - 1/7	40.55±20.21	40.97±24.74	0.42
Fraction - 2/5	48.96±18.37	60.33±23.10	11.36
Fraction - 2/7	39.43±17.08	45.79±23.49	6.36
Max curv - 1/4	38.28±20.22	53.21±29.31	14.93
Max curv - 3/10	39.29±20.71	45.86±25.88	6.57
Max curv - 2/5	45.68±16.81	66.41±25.66	20.73
Discrete - 1/4	37.22±20.67	72.99±42.32	35.77
Discrete - 3/10	35.60±18.31	70.26±34.65	34.66
Discrete - 2/5	45.80±17.06	64.99±22.21	19.20
Oversmooth - 1/4	38.43±19.82	47.65±25.20	9.22
Oversmooth - 3/10	37.19±17.30	47.75±24.99	10.56
Oversmooth - 2/5	46.02±16.65	61.43±21.21	15.41
Line - 1/4	37.19±17.13	45.42±23.65	8.23
Line - 3/10	38.76±16.27	48.77±23.61	10.01
Line - 2/5	49.11±18.42	61.57±23.41	12.46
Plane, Oldclip - 1/4	34.96±16.97	42.15±23.40	7.18
Plane, Oldclip - 3/10	36.80±16.49	45.84±22.93	9.03
Plane, Oldclip - 2/5	46.32±16.67	59.36±22.08	13.04
Plane, Newclip - 1/4	33.45±18.33	41.20±19.40	7.75
Plane, Newclip - 3/10	38.24±18.57	46.56±19.28	8.33
Plane, Newclip - 2/5	52.04±18.12	62.49±17.70	10.45
Manual - Observer 1 (1st)	27.84±17.54	30.24±16.84	2.40
Manual - Observer 1 (2nd)	30.00±14.53	36.69±14.67	6.68
Manual - Observer 2 (1st)	30.43±14.09	36.53±11.75	6.10
Manual - Observer 2 (2nd)	26.55±7.09	42.47±9.45	15.92

Table 5.5: Mean ± SD for angle measurement of increase in angle.

Method	$\theta_{Initial}$	θ_{New}	$\Delta\theta$
Fraction - $^2/_5$	48.96±18.37	60.33±23.10	11.36
Max curv - $^1/_4$	38.28±20.22	53.21±29.31	14.93
Max curv - $^2/_5$	45.68±16.81	66.41±25.66	20.73
Discrete - $^2/_5$	45.80±17.06	64.99±22.21	19.20
Oversmooth - $^3/_{10}$	37.19±17.30	47.75±24.99	10.56
Oversmooth - $^2/_5$	46.02±16.65	61.43±21.21	15.41
Line - $^3/_{10}$	38.76±16.27	48.77±23.61	10.01
Line - $^2/_5$	49.11±18.42	61.57±23.41	12.46
Plane, Oldclip - $^2/_5$	46.32±16.67	59.36±22.08	13.04
Plane, Newclip - $^2/_5$	52.04±18.12	62.49±17.70	10.45
Manual - Observer 1 (1st)	27.84±17.54	30.24±16.84	2.40
Manual - Observer 1 (2nd)	30.00±14.53	36.69±14.67	6.68
Manual - Observer 2 (1st)	30.43±14.09	36.53±11.75	6.10
Manual - Observer 2 (2nd)	26.55±7.09	42.47±9.45	15.92

Table 5.6: Mean ± SD for angle measurement of increase in angle.

Method	$\theta_{Initial}$	θ_{New}	$\Delta\theta$
ODR - Cumulative	40.01±20.61	30.55±17.40	-9.45
ODR - SD	49.74±21.10	31.60±19.14	-18.14
MISR ×1.0	45.32±26.70	36.29±18.71	-9.03
MISR×1.5	43.57±24.95	35.77±18.46	-7.80
MISR ×2.0	44.20±23.20	35.07±18.85	-9.12
MISR ×2.5.5	46.76±23.21	34.17±20.10	-12.60
Fraction - 1/3	42.10±17.39	29.78±14.98	-12.32
Fraction - 1/5	38.49±18.74	28.87±14.04	-9.62
Fraction - 1/7	40.55±20.21	31.85±14.66	-8.71
Fraction - 2/5	48.96±18.37	35.68±15.94	-13.29
Fraction - 2/7	39.43±17.08	27.60±15.12	-11.83
Max curv - 1/4	38.04±19.90	33.57±18.59	-4.47
Max curv - 3/10	39.50±21.01	29.35±14.19	-10.15
Max curv - 2/5	45.68±16.81	36.11±15.21	-9.57
Discrete - 1/4	38.67±23.09	25.58±15.32	-13.09
Discrete - 3/10	35.60±18.31	26.83±14.80	-8.77
Discrete - 2/5	45.80±17.06	34.67±15.25	-11.13
Oversmooth - 1/4	42.93±20.91	32.69±18.61	-10.23
Oversmooth - 3/10	37.19±17.30	28.56±13.85	-8.63
Oversmooth - 2/5	46.02±16.65	35.58±14.93	-10.45
Line - 1/4	37.19±17.13	26.54±14.88	-10.64
Line - 3/10	38.76±16.27	27.31±14.80	-11.45
Line - 2/5	49.11±18.42	35.01±15.56	-14.01
Plane, Oldclip -1/4	34.96±16.97	24.71±15.57	-10.26
Plane, Oldclip -3/10	36.80±16.49	26.20±15.25	-10.61
Plane, Oldclip - 2/5	46.32±16.67	34.31±15.29	-12.02
Plane, Newclip - 1/4	36.98±20.57	25.54±16.08	-11.44
Plane, Newclip - 3/10	41.92±21.04	28.38±16.66	-13.55
Plane, Newclip - 2/5	55.63±20.51	38.59±17.87	-17.04
Manual - Observer 1 (1st)	27.84±17.54	21.85±15.35	-5.41
Manual - Observer 1 (2nd)	30.00±14.53	26.29±15.46	-3.71
Manual - Observer 2 (1st)	30.43±14.09	21.42±9.99	-9.01
Manual - Observer 2 (2nd)	26.55±7.09	16.85±5.56	-9.70

Table 5.7: Mean ± SD for angle measurement of decrease in angle.

Method	$\theta_{Initial}$	θ_{New}	$\Delta\theta$
MISR ×2.5.5	46.76±23.21	34.17±20.10	-12.60
Fraction - 1/3	42.10±17.39	29.78±14.98	-12.32
Fraction - 2/5	48.96±18.37	35.68±15.94	-13.29
Fraction - 2/7	39.43±17.08	27.60±15.12	-11.83
Max curv - 3/10	39.50±21.01	29.35±14.19	-10.15
Discrete - 1/4	38.67±23.09	25.58±15.32	-13.09
Discrete - 2/5	45.80±17.06	34.67±15.25	-11.13
Oversmooth - 1/4	42.93±20.91	32.69±18.61	-10.23
Oversmooth - 2/5	46.02±16.65	35.58±14.93	-10.45
Line - 1/4	37.19±17.13	26.54±14.88	-10.64
Line - 3/10	38.76±16.27	27.31±14.80	-11.45
Line - 2/5	49.11±18.42	35.01±15.56	-14.01
Plane, Oldclip -1/4	34.96±16.97	24.71±15.57	-10.26
Plane, Oldclip -3/10	36.80±16.49	26.20±15.25	-10.61
Plane, Oldclip - 2/5	46.32±16.67	34.31±15.29	-12.02
Plane, Newclip - 1/4	36.98±20.57	25.54±16.08	-11.44
Plane, Newclip - 3/10	41.92±21.04	28.38±16.66	-13.55
Manual - Observer 1 (1st)	27.84±17.54	21.85±15.35	-5.41
Manual - Observer 1 (2nd)	30.00±14.53	26.29±15.46	-3.71
Manual - Observer 2 (1st)	30.43±14.09	21.42±9.99	-9.01
Manual - Observer 2 (2nd)	26.55±7.09	16.85±5.56	-9.70

Table 5.8: Mean ± SD for angle measurement of decrease in angle.

5.4 Discussion

To summarize the proposed methods in this chapter, we compared an automated approach based on selecting points along the centerline with a manual approach where the measurement instrument was constructed in *3D Slicer*. The manually performed measurements were arguably the most similar approach to that of Silva et al. and Waihrich et al. Regrettably, a manual measurement is often biased, and of little reproducibility. To produce more reliable measurements, we compared our manual measurements with the results of the automated measurements in order to select an automated procedure closest in agreement with the manual results.

Based on the results, we carefully selected particular methods with certain input parameters in order to determine a final method. After extensively testing the methods presented in this chapter, the consensus between the observers was that the midpoint selection using the most distal point to the clipping points line was an adequate method, thus becoming the choice for angle measurement as presented in Chapter 6.

Reliability and validity of the proposed methods have been an important consideration for achieving research quality. Using only two observers is a limiting factor, especially when reviewing interobserver discrepancies. In hindsight, an increased number of well-trained observers with relevant insight and validated measurement instruments would have improved the quality of the measurements.

The shape of the anterior bend angle may also be a contributing factor, which may produce biased results. However, the shape of the anterior bend was not considered in the presented measurements.

5.5 Conclusion

The idea of a robust, reliable, and reproducible way of measuring the anterior bend angle is a challenging task due to the large variations in bend characteristics. With no initial starting point for angle measurement, we aimed at proposing a more reproducible method compared to the biased methods by Silva et al. and Waihrich et al.

We propose that a method combining the clipping points from landmarking, and the vessel centerline is a more stable procedure for angle measurement. With the exception of the manual measurements, all the presented methods were automated, which is an improvement. Although we have increased the

reproducibility of angle measurement, the method may still be biased, considering as the final selection was based on manual measurements performed by only two observers. The validity and reliability of the proposed method would increase with an increased number of observers. Increased quality of the measurement instrument would also contribute to producing quality results.

6. Geometric Manipulation of the Internal Carotid Artery

Several geometric features of the internal carotid artery (ICA) have been statistically linked with the presence of aneurysms. This thesis considers the peak curvature and angle of the anterior bend. In Chapter 4 we successfully landmarked the ICA, which defined the anterior bend. In Chapter 3 and Chapter 5 we presented methods for measuring the curvature and angle of the anterior bend, respectfully. The goal of this chapter is to present a framework for objective manipulation of the ICA, specifically of the anterior bend in the ICA. The manipulation will be performed on the landmarked geometries from Chapter 4.

Recent advances in medical imaging and computational fluid dynamics (CFD) have made it possible to computationally reconstruct blood flow patterns in anatomically realistic models. Studies of hemodynamic stimuli in the pathogenesis of aneurysms require knowledge of the pre-aneurysmal vasculature, which motivated development of automated techniques for removal of aneurysms located in the ICA [49, 21]. This has enabled studies to analyze the hemodynamic conditions before and after aneurysm formation, in order to discuss the possible hemodynamic influences in the formation of aneurysms [50]. Additional manipulations include variations of the ICA terminus bifurcation angle and area variations in the ICA of patient-specific morphologies as performed by Bergersen (2016), in order to study how shape variations can impact hemodynamic stimuli [24].

To the author's knowledge, there has not been performed geometric manipulations of the anterior bend in patient-specific models. This motivates manipulation of the anterior bend, followed by CFD simulations in order to explore possible correlations between anterior bend morphology, hemodynamic stimuli, and aneurysm initiation.

6.1 Mathematical Background

6.1.1 The Voronoi Diagram

The Voronoi diagram can be used as an alternative representation of the ICA surface. This enables us to manipulate the surface through the Voronoi diagram. The Voronoi diagram of a set of points P which eventually samples the boundary $\partial\Omega$, can be defined as in [51]

$$\mathrm{Vor}(P) = \bigcup_{\mathbf{p}\in P} \partial V(\mathbf{p}), \tag{6.1}$$

where $V(\mathbf{p})$ is the Voronoi region associated with the point $\mathbf{p}$, defined as

$$V(\mathbf{p}) = \{\mathbf{x} \in \mathbb{R}^3 \,:\, \mathrm{dist}(\mathbf{p},\mathbf{x}) \leq \mathrm{dist}(\mathbf{q},\mathbf{x})\} \qquad \forall\, \mathbf{q} \in P, \tag{6.2}$$

where $\mathrm{dist}(\cdot,\cdot)$ is the Euclidean distance. Hence $V(\mathbf{p})$ is the neighborhood closest to $\mathbf{p}$ than any other element in P. It is clear that points on $\mathrm{Vor}(P)$ have multiple nearest points in P, with the Voronoi diagram lying on the ridge of the distance transform associated with the set P, showing a close relation between the Voronoi diagram and the centerline.

Manipulation of the morphology will be performed using patient-specific models of the ICA, based on using the Voronoi diagram as presented in this chapter, and the centerline as introduced in Chapter 3. The Voronoi diagram and centerline of a selected surface model is visualized in Figure 6.1 **A** and **B**, respectively. Each point of the Voronoi diagram is associated with a maximal inscribed sphere, a sphere not entirely contained in any other inscribed sphere, which provides information on the distance from the boundary. Thus, the complete Voronoi diagram is able to define the boundary of the surface. Besides, each point of the Voronoi diagram can be mapped to a corresponding point on the centerline. By iterating through the Voronoi diagram, we can select the corresponding point on the centerline, and move each Voronoi point a predetermined distance in order to manipulate the surface. Finally, the manipulated Voronoi diagram is reconstructed into a surface.

6.2 Method

6.2.1 Manipulation of the Anterior Bend

In Chapter 3 we performed landmarking of 10 patient-specific geometries, in order to detect the anterior bend along the ICA, which is the area of interest. In order to manipulate the anterior bend morphology, we constructed a

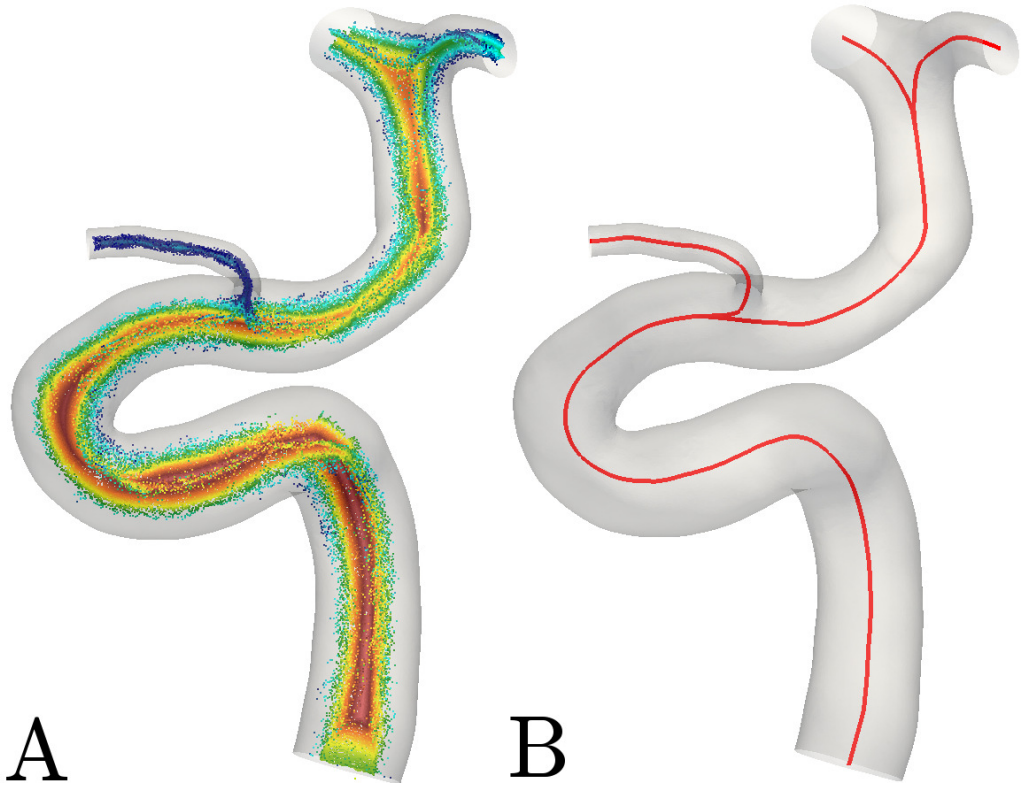

Figure 6.1: **A** Voronoi diagram colored by maximal inscribed sphere radius. **B** Centerline inside a carotid siphon model.

framework which relied on the Voronoi diagram, and the centerline of a patient-specific model, and two clipping points defining the anterior bend, according to the landmarking of the ICA presented by Bogunović et al. [34]. The location of the anterior bend along the carotid siphon relative to the other landmarks is illustrated in Figure 6.2. The algorithm was based on a framework used for ICA geometry manipulation as presented by Bergersen, and aneurysm removal as presented by Ford et al. [24, 49].

The manipulations are performed in order to vary peak curvature, and angle of the anterior bend. Hence we can apply a unified approach, as both morphological features are located in the anterior bend. Given two clipping points, which define the anterior bend, the algorithm proceeds by clipping the model's complete centerline, branching through the entirety of the geometry. The clipped curve representing the anterior bend is then manipulated, by translating points of the Voronoi diagram bounded by the clipping points, in the desired direction. In the presented framework, we have chosen to move the models along an approximation of the sagittal plane. We define the vertical displacement as the perpendicular displacement away from the line between

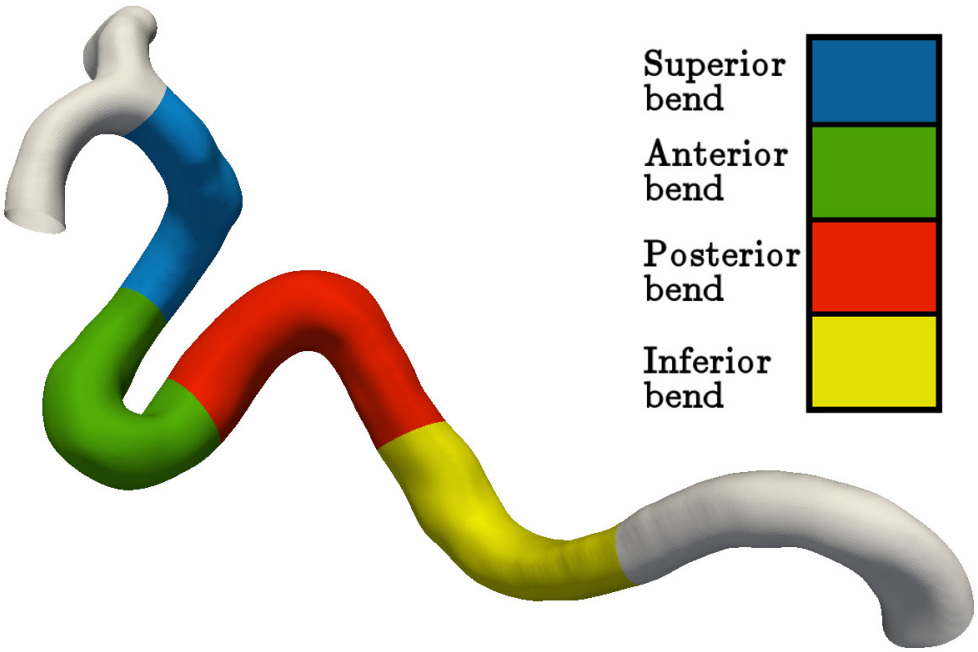

Figure 6.2: The segmentation of the carotid siphon, divided into four bends. The white areas denote the region outside of interest.

the clipping points. The horizontal displacement is defined as the displacement away from the middle point of the anterior bend, in the direction parallel to the line formed by the clipping points. Finally, a new surface model is created from the manipulated Voronoi diagram.

6.2.2 Vertical Displacement

For vertical displacement, we manipulated the initial Voronoi diagram directly, following the steps presented in Figure 6.3. We computed the distance between the line spanned by the clipping points, and the point most distal to this line. By iterating through the points of the Voronoi diagram, the closest corresponding points along the clipped part of the centerline determined how the Voronoi points were moved.

In the following definition, we denote the clipping points as P_0 and P_1. The indices of the points along the centerline are denoted δ_i, where δ_0 and δ_1 corresponds to the indices of P_0 and P_1. For vertical displacement the models were moved a distance of

$$\mathbf{v}_i = 4\Delta\mathbf{y}\left(\frac{(\delta_i - \delta_0)(\delta_1 - \delta_i)}{(\delta_1 - \delta_0)^2}\right) \tag{6.3}$$

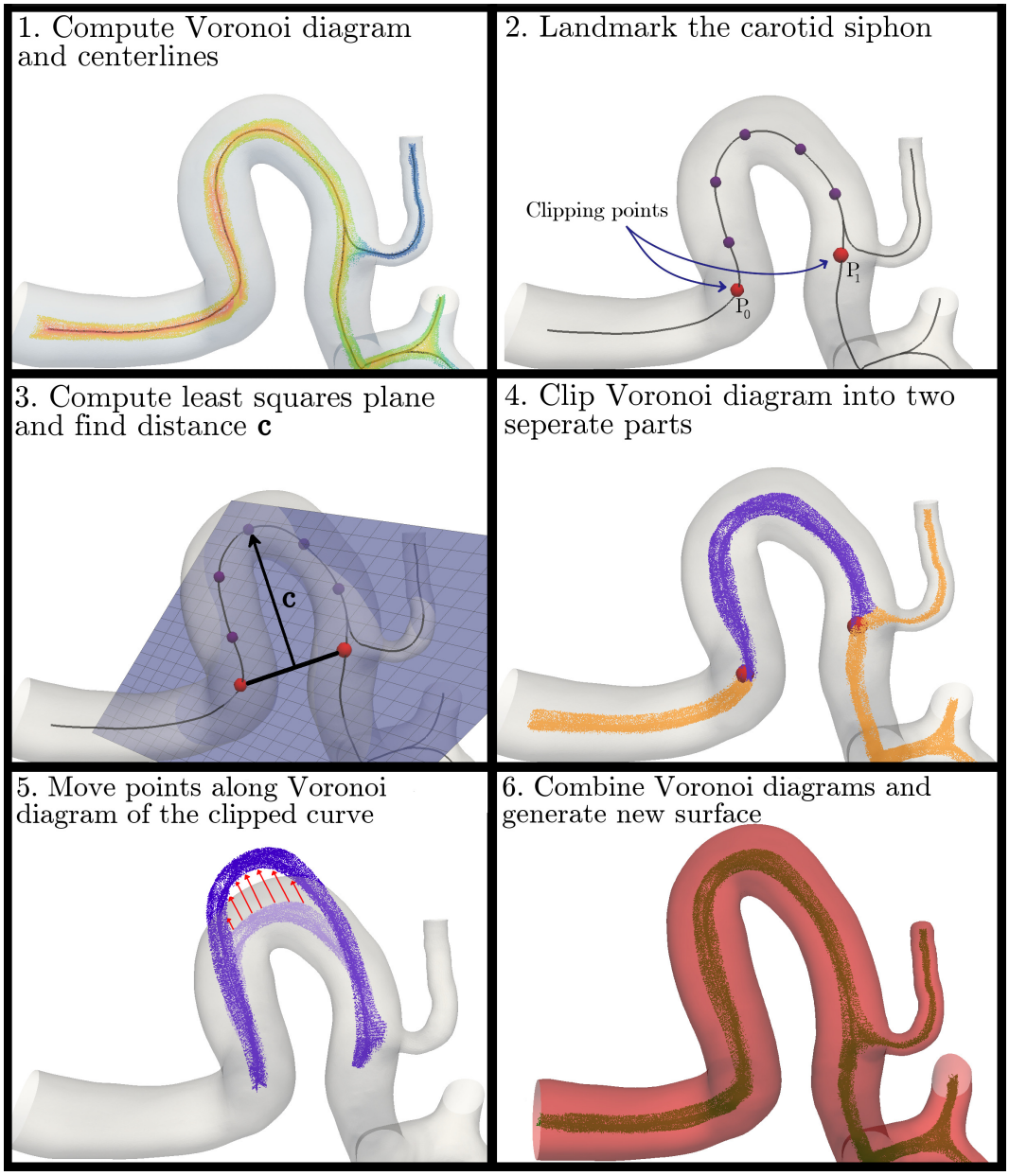

Figure 6.3: Algorithm for geometric manipulation in the vertical direction.

where $\Delta\mathbf{y} = \alpha\mathbf{c}$, with $\alpha \in (-1, 1)$ as a compression factor, and $\mathbf{c}$ is the distance from the line to the point on the centerline furthest away. The factor of 4 assures the distance is normalized at the midpoint, $\delta_{mid} = \frac{(\delta_0+\delta_1)}{2}$. The distance $\mathbf{c}$ was found by finding the constrained least squares approximation of a plane going through P_0, and P_1, and approximating a finite number of points of the anterior bend centerline. Finally, the distance from the line between the clipping points to the projection of the point furthest away defined $\mathbf{c}$.

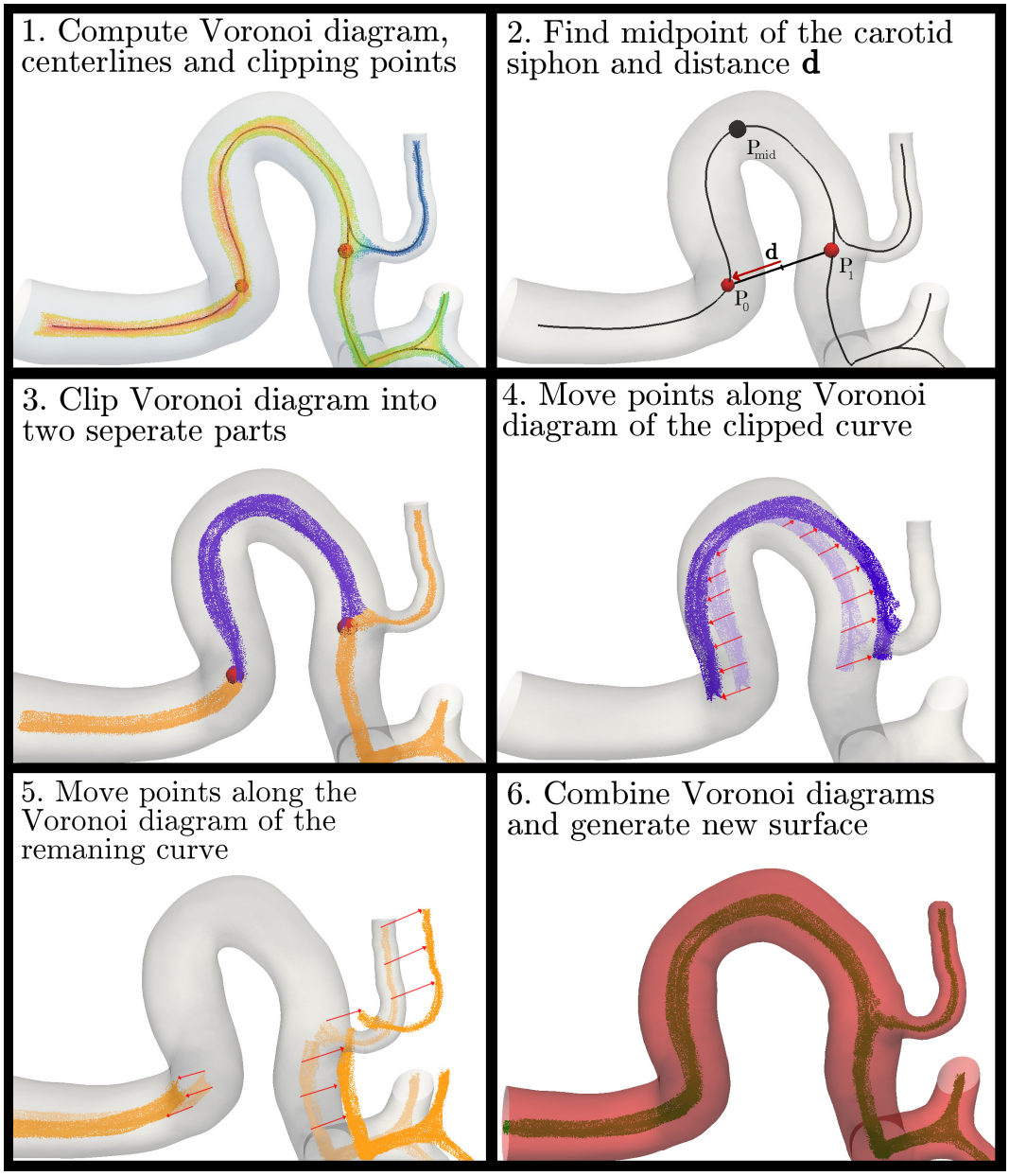

Figure 6.4: Algorithm for geometric manipulation in the horizontal direction.

6.2.3 Horizontal Displacement

The complete algorithm for horizontal displacement is shown in Figure 6.4. For the horizontal displacement, we divided the Voronoi diagram into two separate parts. One part represented the anterior bend, whereas the other part represented the remaining geometry. Following clipping of the Voronoi diagram, we performed steps 4-6 of the manipulation algorithm, as presented in Figure 6.4.

By iterating through the points of the Voronoi diagram, the corresponding points along the clipped part of the centerline determined how far the Voronoi points were displaced. In the following definition, we denote the clipping points as P_0 and P_1. The indices δ_0, δ_1 and δ_i are as defined earlier, as well as $\delta_{mid} = \frac{(\delta_0+\delta_1)}{2}$. For horizontal displacement, the points of the Voronoi diagram were moved a distance of

$$\mathbf{v}_{+i} = +\Delta\mathbf{x}\left(\frac{\delta_{mid}^2 - \delta_i^2}{\delta_{mid}^2 - \delta_0^2}\right) \qquad \text{for } \delta_i < \delta_{mid}, \tag{6.4}$$

$$\mathbf{v}_{-i} = -\Delta\mathbf{x}\left(\frac{\delta_i - \delta_{mid}}{\delta_1 - \delta_{mid}}\right)^{\frac{1}{2}} \qquad \text{for } \delta_i \geq \delta_{mid}, \tag{6.5}$$

where $\Delta\mathbf{x} = \beta\mathbf{d}$, with $\beta \in (-1, 1)$ as a compression factor, and $\mathbf{d}$ is the distance from the midpoint of the clipping point line, and P_0.

The clipped section of the Voronoi diagram, which represented the remaining part of the surface, was moved a constant distance $\pm\Delta\mathbf{x}$, to accompany for the changes to the anterior bend. The sign of $\Delta\mathbf{x}$ depended on the location of the Voronoi point relative to the midpoint of the anterior bend.

6.2.4 Selection of Compression Factors α and β

Each manipulation depended on two input parameters, the compression factors α and β, which determined the magnitude of translation. Selection of the parameters α and β was based on a surface fitting algorithm, which computed the curvature and angle as a function of α and β. Based on several discrete points, the surfaces $\kappa(\alpha, \beta)$, and $\theta(\alpha, \beta)$ were generated by cubic spline interpolation using B-splines. Given the initial angle and peak curvature, the algorithm found the intersection between the interpolated surface and the planes defined for any given value of $\theta \pm$ SD and $\kappa \pm$ SD, where SD is the standard deviation. The intersection was then used to determine possible values for α and β, as illustrated in Figure 6.5.

To avoid under- and over-stretching selection of an optimal value for α and β was based on two criteria; choosing the points closest to the origin, representing the initial value, but outside the circle centered in the origin with radius 0.15, which satisfied the inequality

$$\sqrt{\alpha^2 + \beta^2} > 0.15, \tag{6.6}$$

which we will denote as $\|\alpha\beta\| \equiv \sqrt{\alpha^2 + \beta^2}$. In addition, we including a sanity

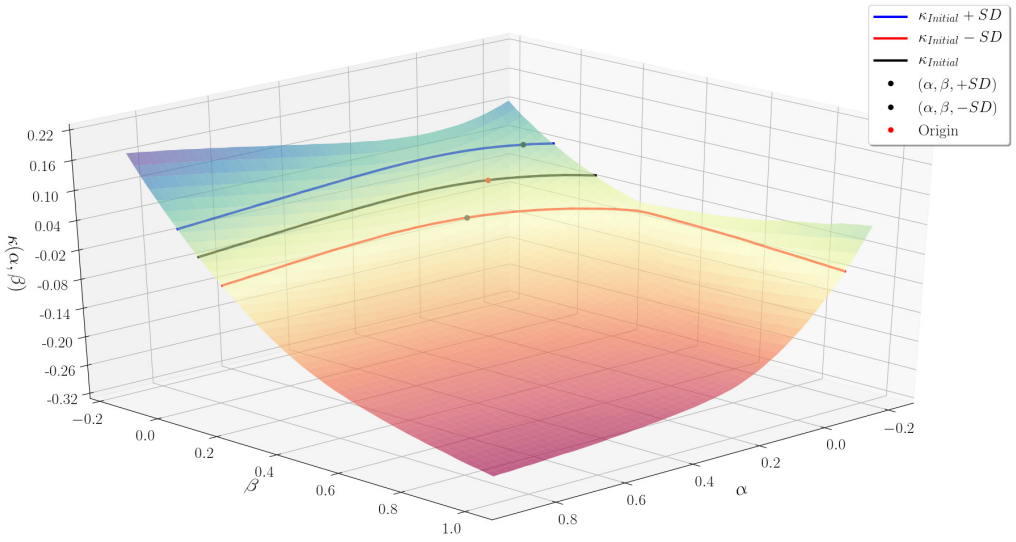

Figure 6.5: Interpolated surface of $\kappa(\alpha, \beta)$ for case P0207, including the intersection with the planes defined by the initial curvature plus and minus one SD, $\kappa_{Initial} \pm$ SD.

check of the sign of β. Increase in curvature, and decrease in angle required $\beta < 0$. Similarly, we required $\beta > 0$ for a decrease in curvature and increase in angle.

6.2.5 The Ophthalmic Artery

Geometries which possessed the ophthalmic artery needed special treatment during translation of the anterior bend. The ophthalmic artery is located within the anterior bend, and requires translation in relation to the bend, as opposed to being moved a constant distance $\pm\Delta\mathbf{x}$. The ophthalmic artery is the first artery to branch out of the ICA, branching out of the anterior bend, and is an essential part of the cardiovascular system, illustrated in Figure 6.6. However, not all computer generated models register the ophthalmic artery.

Detecting an ophthalmic artery was performed by comparing the distance between points along the shortest centerline, possibly representing the ophthalmic artery, with any other given centerline in the surface model. If the distance between corresponding points along the lines is larger than a given tolerance, before reaching the most downstream clipping point, we presumed that the short centerline diverged into the ophthalmic artery, and it was included in the translation algorithm.

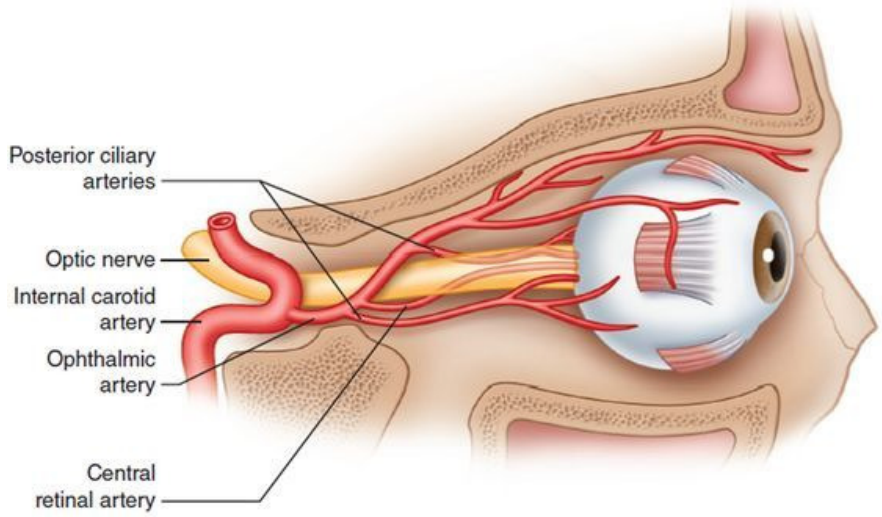

Figure 6.6: The ophthalmic artery and its location relative to the ICA.

6.3 Results

6.3.1 Qualitative Results

The results of the geometric manipulations, with variations in both vertical and horizontal direction, are presented in Figures 6.7 - 6.10. The results include the initial model to be manipulated, colored in white, and the modified models, represented by the red surface. The results represent 40 different manipulations, where the models have been moved with ±SD for angle and curvature, where we used the SD presented in previous studies by Silva et al. and Lauric et al. [21, 22]. In general, the manipulations appear to move the complete geometry accordingly to accompany the horizontal movement. When creating a new surface, the algorithm closes each boundary and creates the bowl-like surface, as shown in the results. Thus, the geometries require an additional clipping to reconstruct the inlet and outlets, which will be performed during meshing of the geometry, prior to CFD simulation in Chapter 7. In addition, the algorithm for detecting the ophthalmic artery is successful as these vessels are translated to appropriate locations in the manipulated models, as shown in cases P0086, P0157, and P0163.

Manipulation with respect to peak curvature variation is presented in Figures 6.7 and 6.8. Although the manipulated models appear to only differ slightly from the initial models, there is an apparent difference across the population. A common trend across the cases is how the cavernous and supraclinoid segments have moved either closer or further apart, corresponding to κ + SD and κ - SD, respectively. Several of the manipulations for κ + SD are also

identified by extension of the anterior bend peak, which we will refer to as the turning point of the anterior bend.

Manipulation of the anterior bend angle is presented in Figures 6.9 and 6.10. For the manipulations where the models are adjusted for plus one SD, there is a noticeable displacement in both directions for every model. All of the cases have combined horizontal and vertical displacement to lessen the amount of strict vertical or horizontal displacement, which can produce unnaturally stretched geometries. To demonstrate this combination, we can observe case P0157 in Figure 6.9, where the turning point is now located further down, and the cavernous and supraclinoid segments have been moved apart by a significant amount.

Prior to manipulation, the limit of negative β was approximated through manual testing across all cases, to prevent overlapping regions in the manipulated geometries. This was utilized in the manipulation presented in Figure 6.10, where the majority of the models show the anterior bend being contracted in the horizontal direction. The results also show how the geometries containing the ophthalmic artery along the anterior bend have been shifted accordingly.

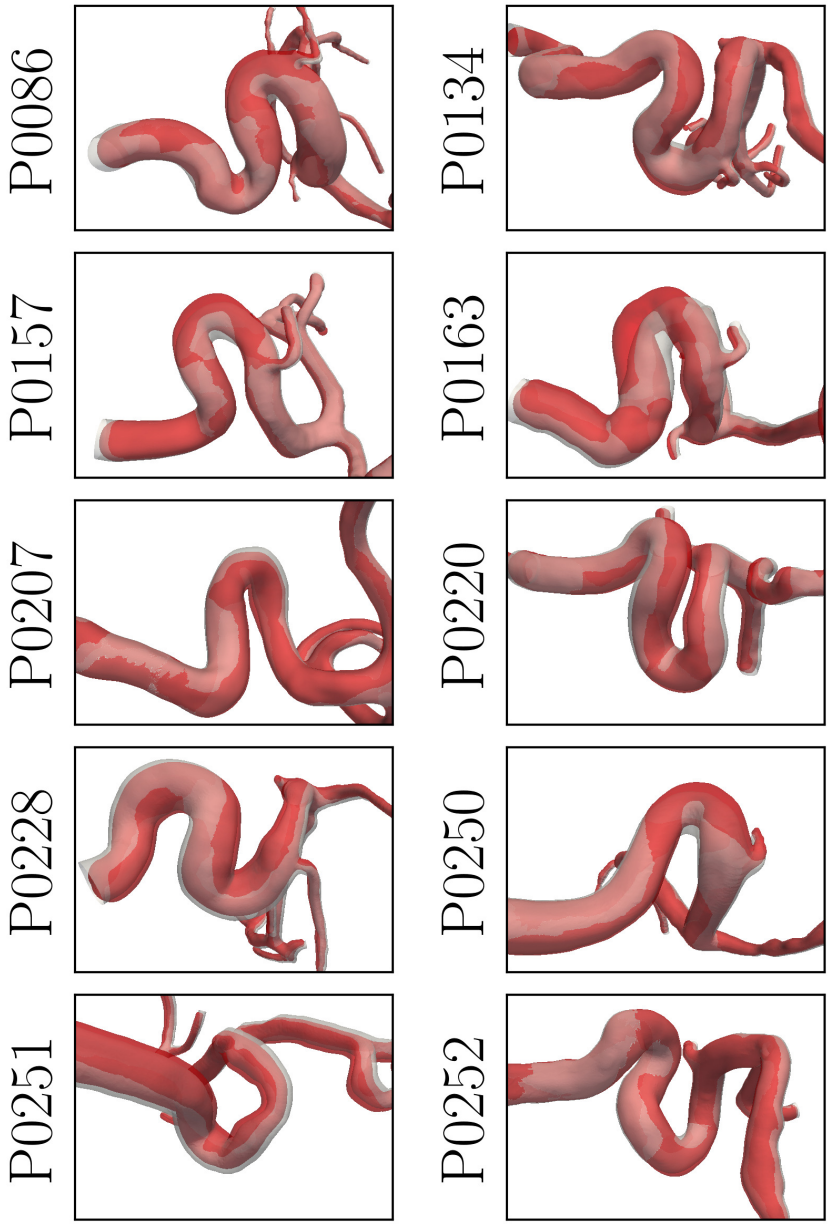

Figure 6.7: Manipulated modes for curvature + SD. The white surface represents the intial model, the red surface represents the manipulated model.

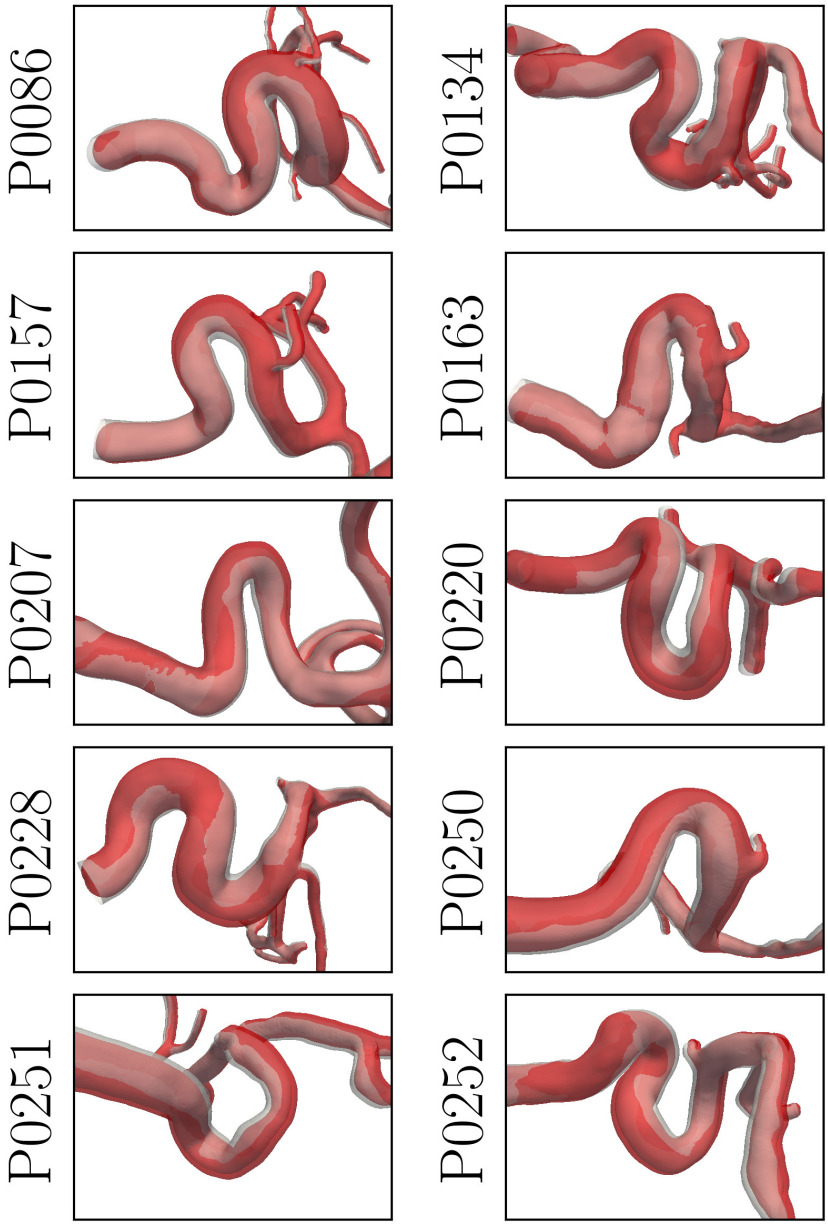

Figure 6.8: Manipulated modes for curvature - SD. The white surface represents the intial model, the red surface represents the manipulated model.

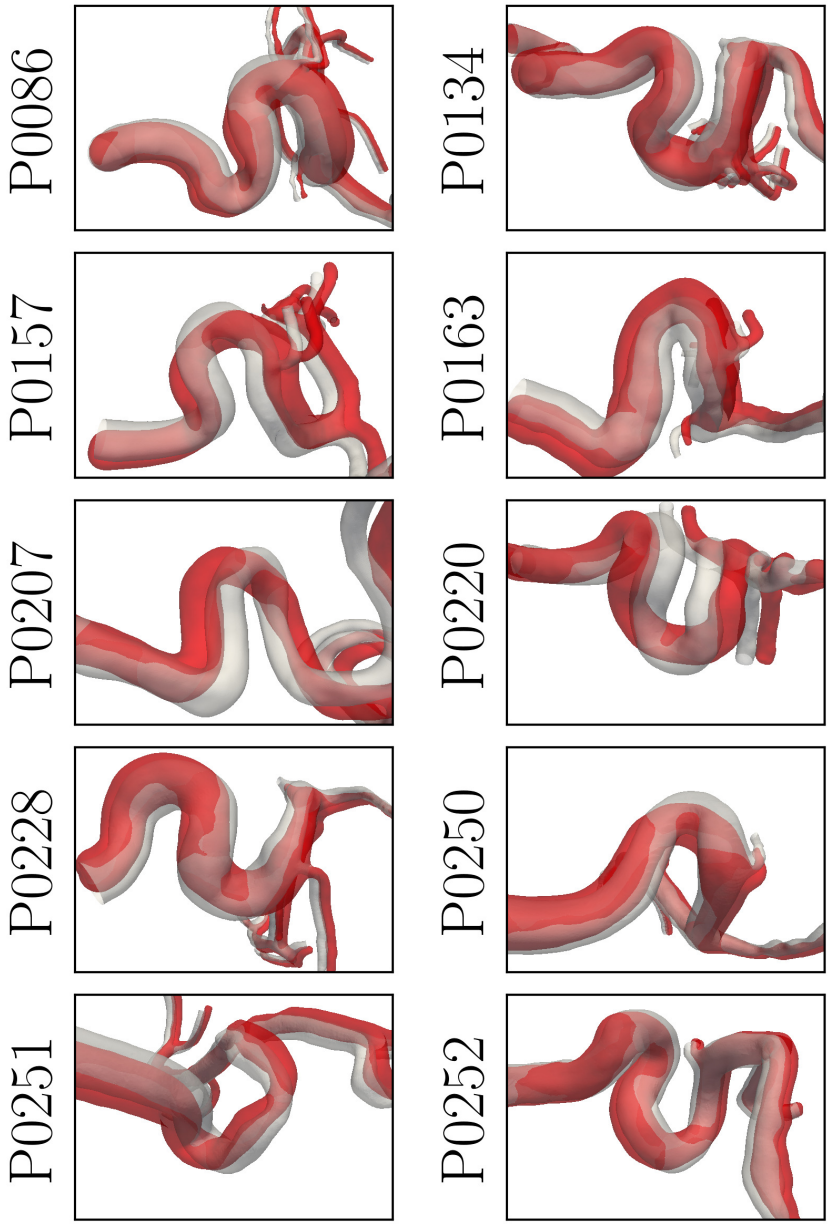

Figure 6.9: Manipulated modes for angle + SD. The white surface represents the intial model, the red surface represents the manipulated model.

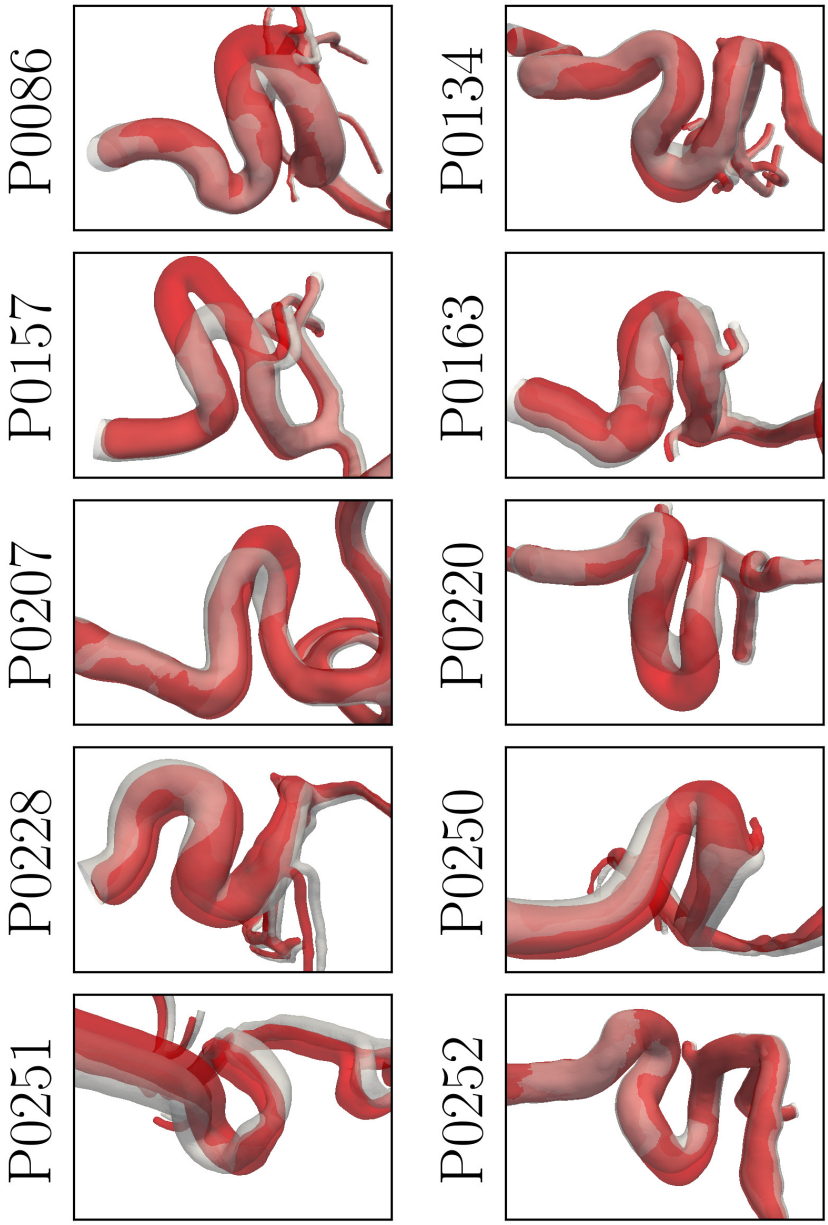

Figure 6.10: Manipulated modes for angle - SD. The white surface represents the intial model, the red surface represents the manipulated model.

Adjustment	$\kappa_{Initial}$	κ_{New}	$\Delta\kappa$
Reference (Aneurysm)	0.360±0.045	-	-
Reference (No aneurysm)	0.300±0.048	-	-
Curvature + SD	0.397±0.069	0.442±0.069	-0.045
Curvature - SD	0.397±0.069	0.353±0.068	0.045

Table 6.9: Mean ± SD of peak curvature values of the anterior bend.

Adjustment	$\theta_{Initial}$	θ_{New}	$\Delta\theta$
Reference (Aneurysm)	26.3±19.1	-	-
Reference (No aneurysm)	33.8±22.6	-	-
Angle + SD	49.11±18.42	67.39±17.72	18.28
Angle - SD	49.11±18.42	31.24±17.20	-17.86

Table 6.10: Mean ± SD of angle measurements of the anterior bend.

6.3.2 Quantitative Results

Subsequent to geometric manipulation, the change in curvature (κ) and angle (θ) were computed by generating a new centerline based on the new model.

The mean values for curvature are listed in Table 6.9, which displays the reference mean values, and standard deviation (SD) from the previous study by Lauric et al., and the new peak curvature of the manipulated geometries including SD. The mean values of the initial models for curvature are similar to the reference mean value. However, the SDs for curvature of the initial and manipulated geometries are significantly larger. Nonetheless, the manipulations were performed using the SD reference value of 0.045 mm^{-1}, which is achieved.

The individual peak curvature is displayed in Tables 6.11 and 6.12, including the differences $\Delta\kappa$. The expected curvature difference of $\Delta\kappa = 0.045$ mm^{-1} is achieved for all cases, with a maximum error of 2% for cases P0220 and P0228, following curvature reduction.

Table 6.10 presents the mean values and SD for the angle in the anterior bend of the initial and manipulated geometries, including the reference values by Silva et al. The mean value of the initial models is considerably larger compared to the reference values, while the SD is very close to the reference SD of 19.1°. However, the change in angle does not reach the expected value of 19.1°. This implies that some cases failed to meet the SD, without requiring unrealistic manipulations, thus limiting the change in angle, and consequently

lowering the mean.

The individual angles are displayed in Tables 6.13 and 6.14, including the differences $\Delta\theta$. Notice that the expected angle difference of $\Delta\theta = 19.1°$ is not achieved for three cases. Cases P0157, P0207, and P220 report angle differences of 17.95°, 14.37°, and 12.70° in magnitude, respectively. The remaining cases achieve the reference value sufficiently. When the angle is increased, case P0163 reports an angle difference of only 11.16°, whereas the remaining cases achieve angle differences of approximately 19.1°.

Case	$\kappa_{Initial}$	κ_{New}	$\Delta\kappa$
P0086	0.397	0.352	-0.0446
P0134	0.334	0.289	-0.0450
P0157	0.429	0.383	-0.0459
P0163	0.495	0.451	-0.0447
P0207	0.528	0.484	-0.0445
P0220	0.337	0.293	-0.0440
P0228	0.377	0.333	-0.0440
P0250	0.356	0.311	-0.0447
P0251	0.392	0.347	-0.0455
P0252	0.329	0.285	-0.0442

Table 6.11: Individual peak curvature values within the anterior bend for decresed curvature.

Case	$\kappa_{Initial}$	κ_{New}	$\Delta\kappa$
P0086	0.397	0.442	0.0448
P0134	0.334	0.378	0.0448
P0157	0.429	0.474	0.0452
P0163	0.495	0.539	0.0441
P0207	0.528	0.574	0.0455
P0220	0.337	0.381	0.0442
P0228	0.377	0.423	0.0455
P0250	0.356	0.400	0.0444
P0251	0.392	0.437	0.0448
P0252	0.329	0.374	0.0451

Table 6.12: Individual peak curvature values within the anterior bend for increased curvature.

Case	$\theta_{Initial}$	θ_{New}	$\Delta\theta$
P0086	41.98	22.92	-19.05
P0134	42.61	23.56	-19.05
P0157	37.11	19.16	-17.95
P0163	67.18	48.06	-19.11
P0207	39.49	25.12	-14.37
P0220	24.02	11.26	-12.76
P0228	58.02	38.91	-19.10
P0250	44.94	25.88	-19.05
P0251	45.81	26.74	-19.06
P0252	89.86	70.76	-19.09

Table 6.13: Individual angle measuments of the anterior bend for incresed angle.

Case	$\theta_{Initial}$	θ_{New}	$\Delta\theta$
P0086	41.98	61.08	19.10
P0134	42.61	61.68	19.06
P0157	37.11	56.22	19.10
P0163	67.18	78.34	11.16
P0207	39.49	58.55	19.05
P0220	24.02	43.10	19.07
P0228	58.02	77.09	19.07
P0250	44.94	63.99	19.05
P0251	45.81	64.87	19.06
P0252	89.86	108.96	19.10

Table 6.14: Individual angle measuments of the anterior bend for decresed angle.

6.4 Discussion

The main goal of this chapter was manipulation of the anterior bend, followed by a comparison of computed values for curvature and angle with previously reported values in the literature.

6.4.1 Geometric Manipulation of the Anterior Bend

Recall that

$$\|\alpha\beta\| > 0.15, \tag{6.7}$$

was the main criteria for selection of the compression factors α and β. Thus the magnitude of manipulation per model was bounded by the factor 0.15, acting as a lower limit.

Models computed with respect to the reference SD for curvature of $0.045\,\mathrm{mm}^{-1}$, ended up with a norm close to 0.15 for the majority of the cases, with a mean value of $\overline{\|\alpha\beta\|}_{\kappa} = 0.18$. The arguably low mean value resulted in a minor, although apparent morphologic difference post manipulation. Different values of α and β could be chosen in collaboration with a clinician, resulting in more or less variation. However, we argue that the choice of the selected values for α and β is reasonable, considering curvature only varies with the sharpness of the anterior bend.

On the contrary, a manipulation with intent to adjust the angle, using the reference SD of 19.1°, required large alterations in the geometry. Selection of α and β showed a considerable increase of the mean value norm of $\overline{\|\alpha\beta\|}_{\theta} = 0.51$, with $\min\|\alpha\beta\|_{\theta} = 0.26$ and $\max\|\alpha\beta\|_{\theta} = 0.91$. Thus, it can be expected that the geometries vary greatly in comparison with the initial model.

Regardless of the values of α and β, a general concern of geometry manipulation is how it affects the vessel area. Area variations are statistically linked with the presence of intracranial aneurysms, as presented by Schimansky et al. [20], and have been shown to introduce phenotypically different flow patterns resulting in increased temporal wall shear stress gradient [24]. Thus, an analysis of potential area variations was performed, based on two methods for area calculation.

Initially, the vessel area was computed by the VMTK script *vmtkcenterlinesections*, which generated cross-sectional surfaces inscribed in the vessel and positioned normal to the centerline. Conveniently, *vmtkcenterlinesection* performed computation of geometric properties including cross-sectional area. Regrettably, the cross-sectional areas were affected by the region of the vessel

leading into the ophthalmic artery, which produced unrealistic area calculations in certain parts of the ICA. Hence, an alternative, but arguably naive approach was performed for comparison. The procedure performed approximations of the vessel area by iterating along the centerline, and assuming circular cross-sections inscribed in the vessel. Thus, the area was computed by using the maximal inscribed sphere radius (MISR) in the standard formula for the area of a circle. A comparison of the two proposed methods for area calculations have been visualized in Figure 6.11, for a representative case pre- and post-manipulation. The comparison between the area before and after manipulation shows the general trend across all cases. With respect to area magnitude, there is no significant difference. However, the area has been shifted which should be considered an expected consequence as the models are stretched or contracted in various directions. Optimally we would require no vertical (magnitude) nor horizontal (shifted) change in the area, but it is reasonable to allow a shifted area distribution as long as the magnitude is overall similar.

Finally, the framework provided the possibility to move the model in both directions simultaneously. However, the user should be aware when using negative values for the compression factors α and β. Contracting the models too much can cause the Voronoi diagram to overlap, causing the reconstructed surface to overlap, thus producing unrealistic models. One way of detecting this error is by computing the centerline of the new surface, and compare it with the initial centerline, as a model containing overlaps will generate centerlines which diverge away from the initial centerline. However, this was not implemented, and detection of possible overlap was performed manually.

6.4.2 Curvature and Angle Variations

Following manipulation of the anterior bend, curvature variations (κ) and angle variations (θ) were computed for comparison with values presented in the literature [21, 22]. For each case, a new centerline through the entirety of the geometry was computed based on the newly generated surface model, in order to compute geometric properties.

The mean values for curvature in Table 6.9 is shown in comparison to the mean peak curvature of 0.36 ± 0.045 mm^{-1} as reported by Lauric et al. (2014), including a control group where the peak curvature was 0.30 ± 0.048 mm^{-1} [21]. In the report by Lauric et al. it is concluded that high bend curvature induces an increase in hemodynamic stimuli, in particular, WSS and WSSG, leading to conditions along the blood vessel known to induce vessel wall remodeling, and consequently aneurysm initiation. In addition, Lauric et al.

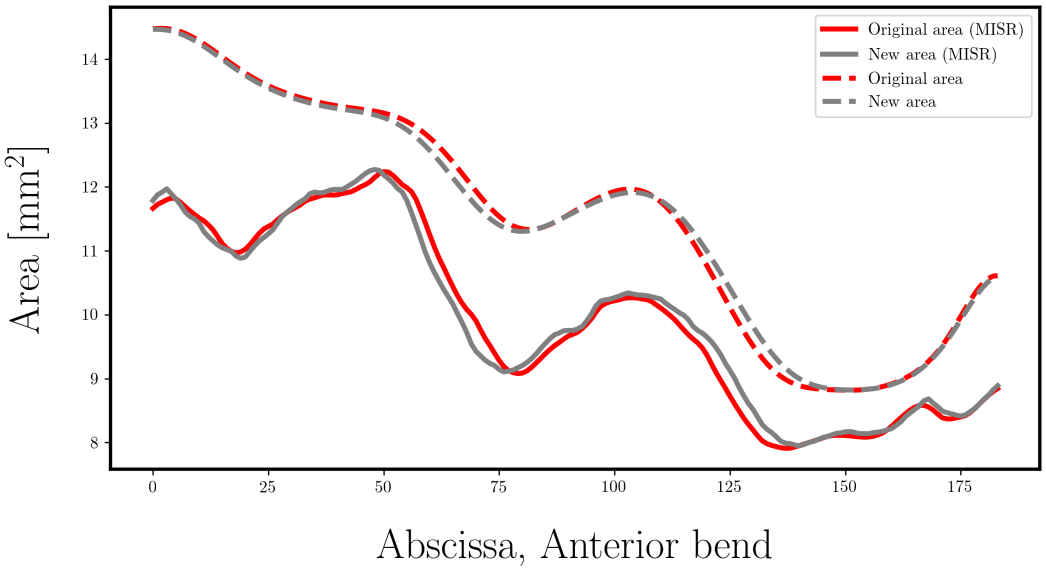

Figure 6.11: Area variation between initial and manipulated model for a representative case. Areas have been computed by `vmtkcenterlinesections` and directly from MISR, assuming circular cross section.

report that the curvature was estimated analytically by employing discrete derivatives. Regrettably, the choice of input parameters is not mentioned. Although we implemented the same method, selection of input arguments might cause differences in the peak curvature. Nonetheless, the manipulations are all successful of reaching the curvature difference of ± 0.045 mm^{-1}, as confirmed by the results in Tables 6.11 and 6.12.

For angle variations, we compared our results with the results presented by Silva et al. (2012), as listed in Table 6.10. Silva et al. evaluated ICA variants in patients with aneurysms, with a selection of posterior communicating artery (PcomA) aneurysms most common in women, and anterior communicating artery (AcomA) aneurysms more common in men. It was reported that patients with PcomA aneurysms possessed narrower angles in the carotid siphon with reports of $\theta = 27.3 \pm 19.1$, while the control group, being patients without aneurysms, had wider angles in the siphon bend, where $\theta = 34.8 \pm 22.6$. The report by Silva et al. concluded that a narrower anterior bend angle may cause increased hemodynamic stimuli, thus promoting the formation of aneurysms.

Silva et al. measured the angle where two straight lines met. However, the procedure of angle measurement is unclear. Silva et al. mention that two straight lines were drawn, starting at the midpoints of the arterial diameters of the segments under question, followed by angle measurement, with no fur-

ther explanation of this procedure. Silva et al. do admit that the procedure may be biased, considering their method has low reproducibility. Although we were inspired by the procedure by Silva et al., the results presented in this chapter may be incomparable, as our proposed method for angle measurement is considerably different.

The mean values listed in Table 6.10 show how the expected angle difference of 19.1° has not been attained. Meanwhile, the computed SDs of the patient-specific models are of similar magnitude compared to the reference SD. For further insight we can analyze the individual results as presented in Tables 6.13 and 6.14.

When the angle is decreased, the cases P0157, P0207, and P0220 show angle differences of 17.95°, 14.37°, and 12.70° in magnitude, respectively. The shape of the anterior bend in cases P0157 and P0220 both resemble a C-shape, where the bend grows slightly outward after passing the clipping points. Hence the second points along the anterior bend siphon produce a narrow initial angle. This is confirmed in Table 6.14, where case P0157, and P0220 have the smallest initial angles. Thus an unrealistic amount of manipulation is required in order to reach the goal of $\Delta\theta = -19.1°$. Although the anterior bend of case P0207 resembles the U-shape the most, the cavernous and supraclinoid segments of the ICA are initially very close, restricting the amount of manipulation between the segments. In addition, the initial angle of case P0207 is the third smallest, which may explain the results. Finally, when the angle is increased case P0163 reports an angle difference of only 11.16°. We speculate the small change in angle is related to the position of the clipping points relative to each other, as the most downstream clipping point is slightly dislocated relative to the upstream clipping point.

To summarize, the manipulations with curvature variation were successful and reached the expected curvature difference of 0.045 mm^{-1}. Although the manipulations with respect to angle variation did not achieve the expected difference of 19.1°, we argue that sacrificing some degrees in order to produce realistic models still produce satisfactory results. The morphology of the initial and manipulated models, with respect to angle variation, show large distinctions, regardless of $\Delta\theta$, making them suitable for progression.

6.5 Conclusion

The results and the following discussion shows how our approach to the geometric manipulation of the anterior bend is a reliable and robust method. Therefore we will advance by performing computational fluid dynamics simu-

lations of the initial, and manipulated geometries, and evaluate the hemodynamic stress created by different flow patterns, based on the various geometries.

Possible improvements include performing a larger cohort study to further validate this manipulation technique, or adjusting the profiles used for moving the geometries, in either direction. To minimize the horizontal area variations, an additional task may be conservation of the anterior bend length during manipulation.

7. A Computational Study of the Effects of Morphology Manipulations in the Internal Carotid Artery

In this chapter, we apply the manipulated geometries from the framework for geometric manipulation of the internal carotid artery (ICA) presented in Chapter 6. The goal of this chapter is to investigate the potential link between morphologic features known to be correlated with initiation of intracranial aneurysms, and the hemodynamic stimuli in the terminal bifurcation of the ICA. The morphological feature to be altered is the anterior bend of the ICA, by applying the tools developed in the previous chapters, followed by computational fluid dynamics simulations (CFD) in the new surface models. The simulations can give insight on whether or not certain hemodynamic stimuli is associated with aneurysm initiation, and may clarify the hypothesis presented by Valen-Sendstad et al., where it was hypothesized that aneurysm initiation could be caused by unstable blood flow, which appeared to be as common as stable, laminar flow [16]. In addition, analysis of the hemodynamic stimuli might shed light on the hypothesis by Meng et al., in which it was hypothesized that a combination of high WSS and WSSG are correlated with aneurysm initiation [10].

7.1 Method

7.1.1 Mesh generation

Our cohort consisted of ten healthy cases from the Aneurisk database, including four manipulations per case, resulting in a total of 50 surface models. Prior to CFD simulation, the manipulated geometries had to be cut at the inlet and outlets, perpendicular to the centerline. In order to maintain a consistent inlet and outlet area between the manipulated and initial models, the

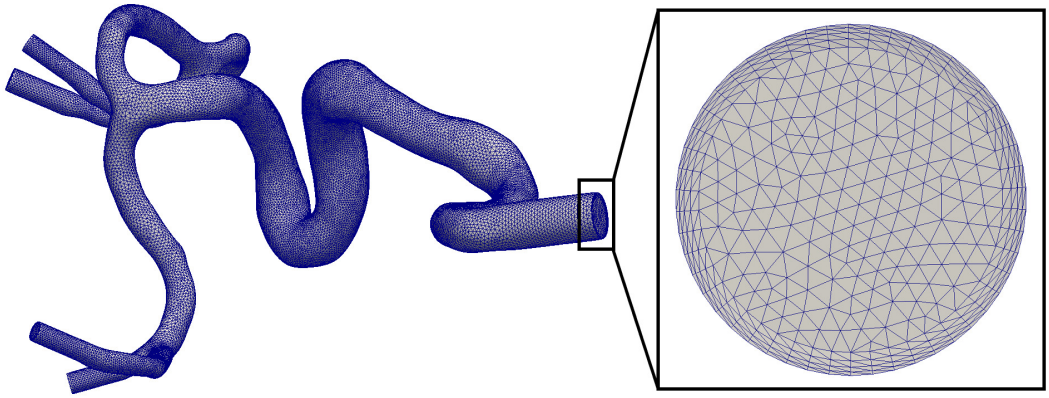

Figure 7.1: Mesh generated from case P0220, including a magnification of a inlet showing four boundary layers.

initial models underwent a Voronoi smoothing, enclosing the models, followed by uncapping. This procedure caused the inlet and outlet areas to vary with less than 1%, between the models. Flow extensions at the inlet and outlets were added to remove the effects of artificial boundary conditions. To remove non-physiological artifacts in the surface, the models were smoothed using the VMTK script *vmtksurfacesmoothing*, applying Taubin and Laplacian smoothing, with 200 and 800 smoothing iterations, and the default values for pass-band and relaxation factor, respectively. Two of the models included a sudden narrowing of the arteries, known as stenosis, which required an increased number of smoothing iterations. Each mesh was created using VMTK, by the method of variable density mesh. An illustration of a meshed surface is shown in Figure 7.1. The complete pipeline included capping, smoothing, adding flow extensions, and selection of areas requiring higher mesh density. Following mesh generation, flow rate ratios between outlets were computed, followed by the possibility to upload and initialize a simulation to the Abel supercomputer cluster [52]. Based on the original surfaces, the average number of cells used for mesh generation was 2.1 million, an adequate spatial resolution for the question of interest [14].

7.1.2 Setup

The patient-specific models of the ICA required the specification of physiological flow conditions. Ideally, both patient-specific geometries and patient-specific boundary conditions are required for accurate CFD simulations. However, patient-specific data is rarely available. Therefore, we have to adopt flow rates and waveforms from typical waveforms, averaged from multiple subjects. As a consequence, the choice of approximation will affect the computational results, and later hemodynamic analysis.

The waveform applied in this thesis is based on the waveform presented by Hoi et al. [53], using the following approximation of the mean flow rate as proposed by Valen-Sendstad et al. [54]

$$Q = 0.27A, \tag{7.1}$$

where Q is the flow rate, and A is the cross-sectional area of the inlet. The waveform presented by Hoi et al. is a volumetric flow rate waveform, and is suitable as a boundary condition for models of blood flow through the carotid arteries. Throughout the simulation, the pressure at each outlet is adjusted iteratively to achieve the desired flow division. The pressure boundary condition was based on the dual-pressure boundary condition developed for computational modeling of bifurcating conduits [55]. As presented by Gin et al., the correction of the new pressure at the ith outlet, $p_{new,i}$, is a computed by a power-law on the form

$$p_{new,i} = p_{old,i} \cdot \gamma \cdot M_{err}^{E} \qquad \text{for } i = 1, \ldots, N, \tag{7.2}$$

where the correction coefficient M_{err}^{E} consists of the mass flow error M_{err}, and exponent E, defined as

$$M_{err} = \frac{R_{optimal}}{R_{computed}}, \tag{7.3}$$

$$E = -\text{sign}(p_{old,i}) \left(1 + \frac{|R_{optimal} - R_{computed}|}{R_{optimal}}\right), \tag{7.4}$$

where

$$R = \frac{Q_{outlet,i}}{Q_{inlet}}, \tag{7.5}$$

is the flow ratio. The acceleration coefficient γ depends on the deviation between the computed and optimal flow division, for simplicity denoted

$$e_R = |R_{optimal} - R_{computed}|. \tag{7.6}$$

In the present computation, γ was modeled as

$$\gamma = \begin{cases} 0.5 & \text{if } e_R \geq 0.1, p_{old,i} < 0 \\ 1 + 5 \cdot \text{sign}(p_{old,i}) \cdot e_R^2 & \text{if } e_R < 0.1 \\ 1.5 & \text{if } e_R \geq 0.1, p_{old,i} > 0. \end{cases} \tag{7.7}$$

However, Gin et al. does not discuss the choice of initial conditions. The initial pressure at each outlet was set in such a way as to maintain a desired

flow division. For the simulations performed in this chapter, we propose the following initial value for the ith outlet

$$p_{initial,i} = 0.1 \cdot \frac{\frac{1}{R_{optimal,i}}}{\frac{1}{N}\sum_{j=1}^{N} \frac{1}{R_{optimal,j}}}, \qquad \text{for } i = 1, \ldots, N. \tag{7.8}$$

Due to the exponential nature of the proposed pressure correction model, the initial values based on the inverse flow split ratio would often lead to diverging pressure in one or multiple outlets. To cope with the exponential growth, a linear model was proposed for the first three hundred time steps, to work as a stabilizer. A simple, yet robust model was implemented as

$$p_{new,i} = p_{old,i} \left(1 - e_R \cdot h \cdot \frac{R_{optimal} - R_{computed}}{R_{optimal}}\right), \tag{7.9}$$

where h is a weighting factor set to 0.1 in this study. Throughout multiple simulations, we observed oscillations of flow split at the early stages of the first cardiac cycle, before the stabilization of pressure assured convergence of flow split.

To remove initial effects due to non-physiological initial conditions, the simulations were run over two cardiac cycles, each lasting 0.951 s. Only the second cycle was used for computation and analysis of hemodynamic stimuli. Furthermore, the time step was set to $\Delta t = 9.51 \cdot 10^{-5}$. From the studies by Khan et al., also using *Oasis*, we know that this is a sufficient temporal resolution [14]. For blood flow, the kinematic viscosity was set to $\nu = 3.3081 \cdot 10^{-6}$ m^2 s^{-1}.

During post-processing, we studied the wall shear stress (WSS), the spacial WSS gradient (WSSG), and the temporal WSS gradient (TWSSG), derived from the shear stress τ, collectively defined as

$$\tau = \mu \left.\frac{\partial u}{\partial y_w}\right|_{w=0}, \tag{7.10}$$

$$\mathrm{WSS} = \frac{1}{T}\int_0^T |\tau| \mathrm{d}t, \tag{7.11}$$

$$\mathrm{WSSG} = \nabla \left(\frac{1}{T}\int_0^T |\tau| \mathrm{d}t\right), \tag{7.12}$$

$$\mathrm{TWSSG} = \frac{1}{T}\int_0^T \left|\frac{\partial \tau}{\partial t}\right| \mathrm{d}t, \tag{7.13}$$

$$\tag{7.14}$$

where y_w is the distance to the wall, μ is the dynamic viscosity, and u is the tangential velocity to the wall. The following results have been compared in magnitude by using a common scaling, where the hemodynamic quantities were time-averaged over 200 velocity files for the second cardiac cycle.

7.2 Results

A total of ten cases were manipulated, although the results only include the first five consecutive cases. For every case, a total of five simulations were performed: $\pm$ one standard deviation (SD) of the angle in the anterior bend, the original surface, and $\pm$ one SD of the peak curvature in the anterior bend.

7.2.1 Curvature Variation Within the Anterior Bend

The qualitative results of WSS, WSSG, and TWSSG from curvature variations along the anterior bend curve are presented in Figures 7.2, 7.3, and 7.4, respectively.

First, we observe the change in WSS in Figure 7.2. The cases are visualized at the terminus bifurcation of the internal carotid artery, a common location for aneurysm initiation. The WSS is for all practical purposes unaffected by the change in curvature, with no noticeable phenotypical difference. The exception is case P0207, where a slight increase in WSS is observable, as the peak curvature is increased. There is arguably a slight decrease in WSS magnitude for case P0157, for the geometry with increased curvature. Nonetheless, for any of the five cases, the location of the WSS does not change, and there is no clear trend.

Figure 7.3 presents the WSSG at the bifurcation of the five cases. There are no remarkable phenotypical differences across the cases. Cases P0086 and P0163 show no trend in correlation with the curvature variations. A somewhat discreet difference in WSSG location is noticeable for case P0134, although the WSSG magnitude is similar. An overall increase of WSSG can be noticed at the bifurcation apex of case P0157. Case P0207 is the only case where there is a noteworthy magnitudal difference in WSSG. In particular, there is a noticeable increase in WSSG magnitude along the left daughter artery, and at the bifurcation apex, as the curvature is increased.

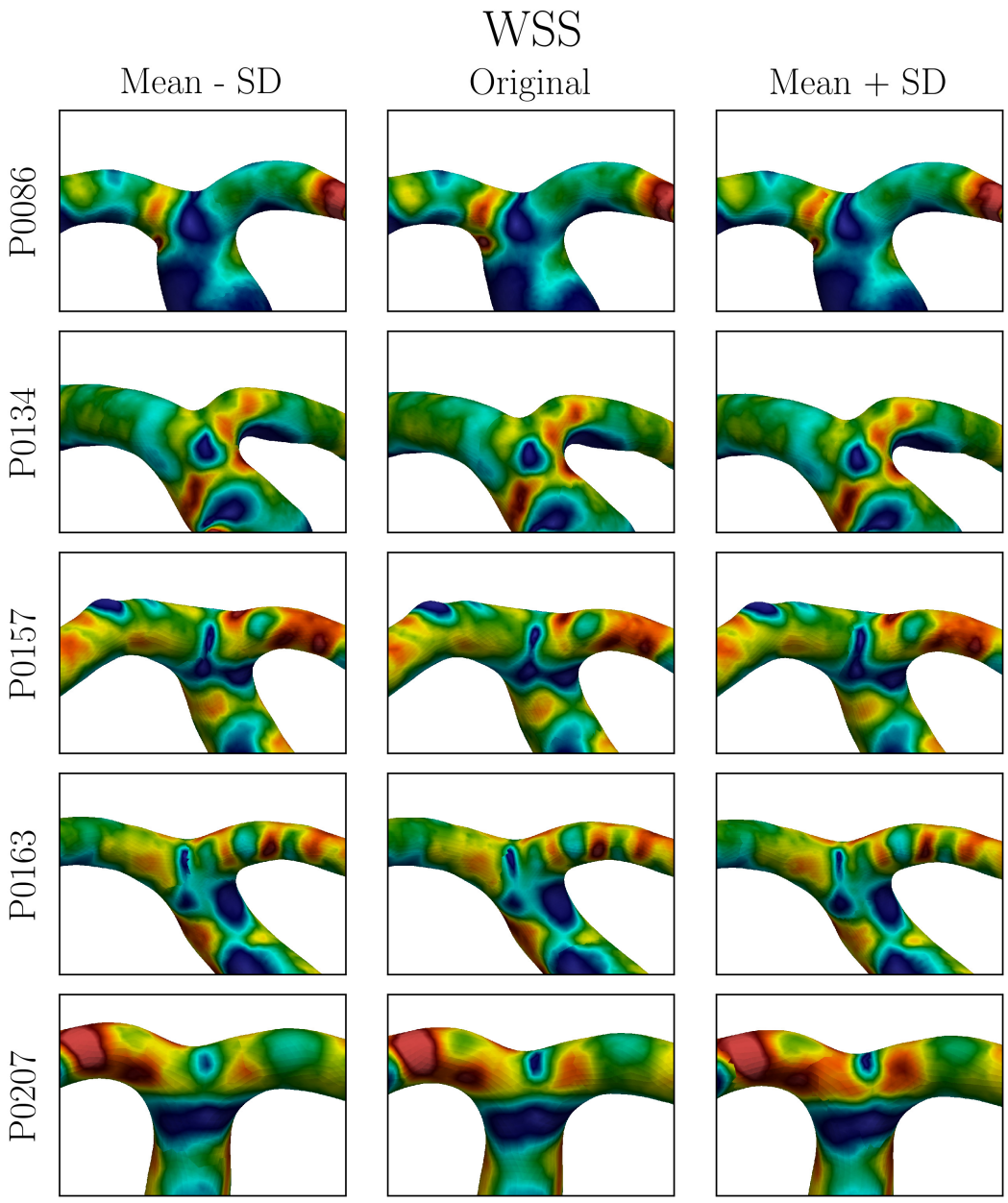

Figure 7.2: WSS for five cases, with three simulations per case, where the curvature has been adjusted ± one SD.

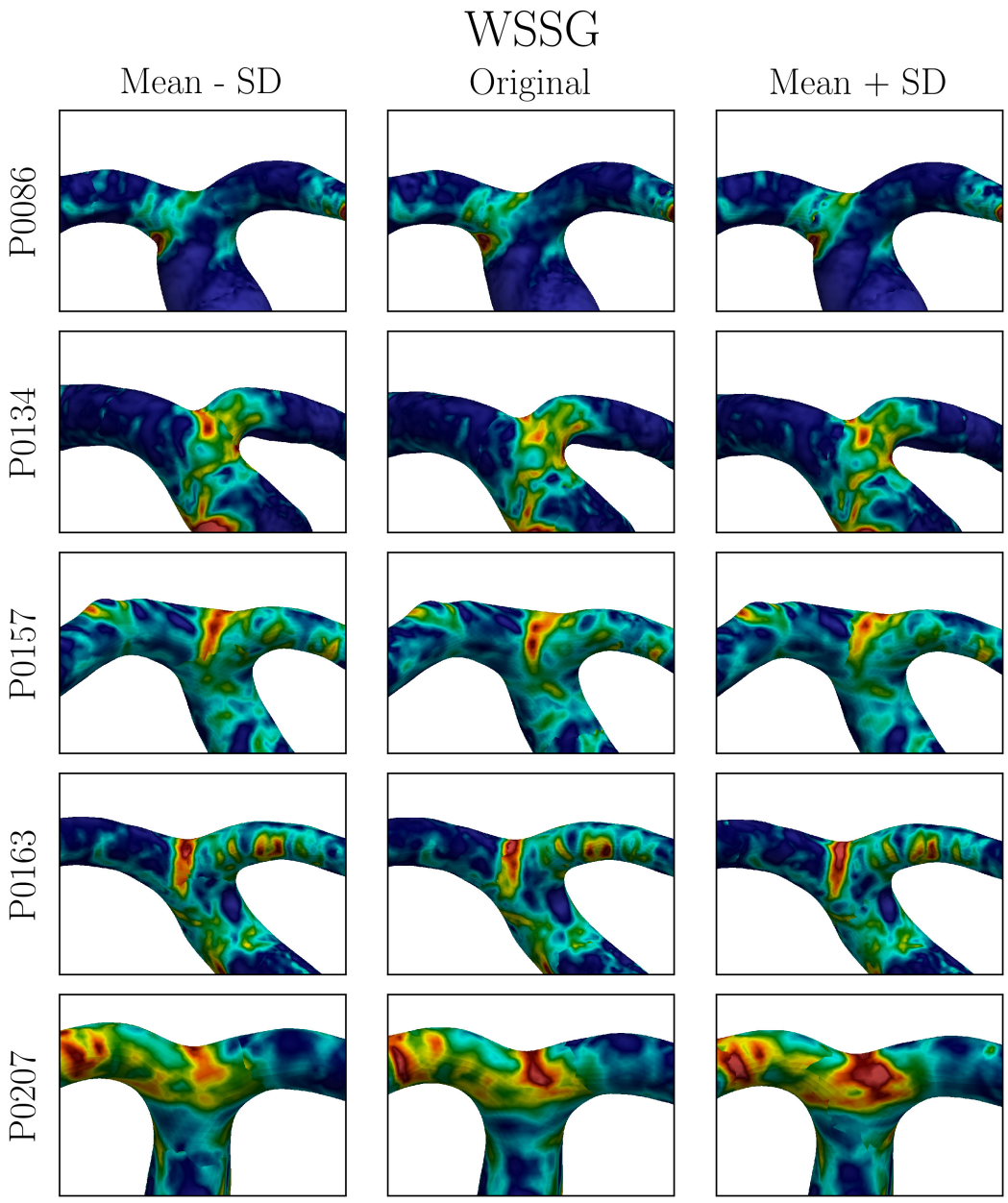

Figure 7.3: WSSG for five cases, with three simulations per case, where the curvature has been adjusted ± one SD.

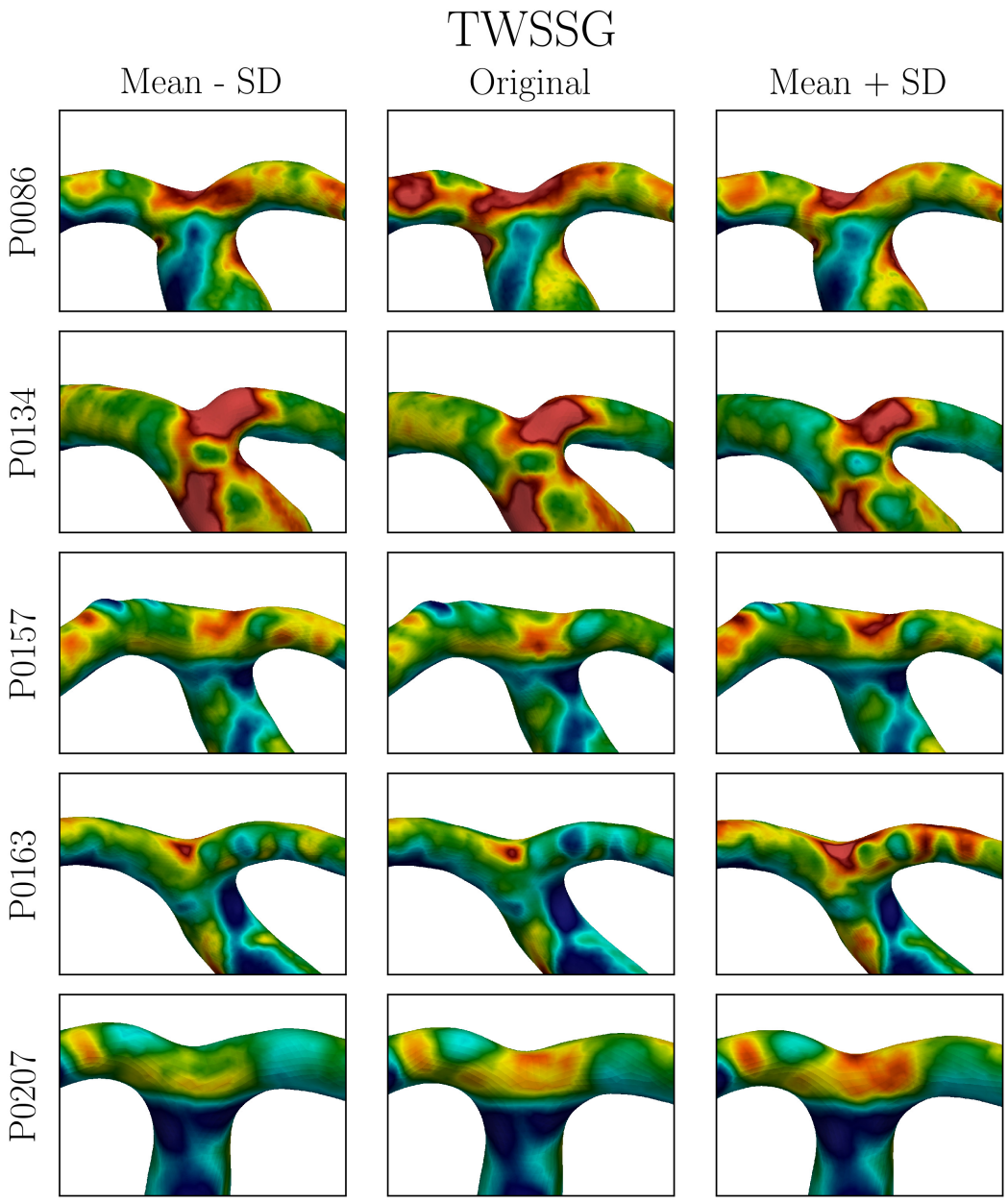

Figure 7.4: TWSSG for five cases, with three simulations per case, where the curvature has been adjusted ± one SD.

Figure 7.4 presents the TWSSG of the five cases. The results of TWSSG in the geometries exposed for curvature variations does not show any notable difference in overall magnitude. However, there is a noticeable change in location of the affected area. Case P0086 shows how the peak TWSSG is relocated as the curvature increases, moving from a less defined area in the vicinity of the apex towards the leftmost daughter artery. A small magnitudal difference can be observed upstream of the apex. There are no noticeable relocations in case P0134, although there is a slight decrease in TWSSG magnitude for increased curvature. Similarly, in case P0157, the overall TWSSG magnitude stays unaffected, although there is a slight increase around the apex, as the peak curvature of the anterior bend increases.

7.2.2 Angle Variation Within the Anterior Bend

The qualitative results of WSS, WSSG, and TWSSG for angle variations of the anterior bend is presented in Figures 7.5, 7.6, and 7.7, respectively.

The change in WSS magnitude for angle variations is presented in Figure 7.5. Among the presented results there are no considerable phenotypical differences between small and large angles of the anterior bend. In cases P0086, P0134, and P0163 we observe a negligible increase in the overall WSS magnitude, as the anterior bend angle increases. Case P0157 appears to be affected to some degree, with small variations in WSS magnitude between all the three simulations. There is a slight increase in overall WSS for both decreased and increased anterior bend angle, noticeable along the vessel of the daughter arteries. However, upstream of the bifurcation apex there is a noticeable increase in WSS magnitude as the angle is decreased. There is a noticeable correlation between the WSS magnitude and the angle of the anterior bend in case P0207, particularly around the apex and the rightmost daughter artery. Simultaneously, a decrease in WSS can be observed on the leftmost daughter artery, as the angle increases. Overall, there is no noticeable change in WSS location.

The WSSG magnitude is presented in Figure 7.6. There are no phenotypical differences, and no apparent overall trend. A small increase in WSSG is noticeable in cases P0086, P0134, and P0163, as the angle increases, although there is no apparent relocation. In case P0157, we observe a decrease of WSSG magnitude along the leftmost daughter artery and an increase along the rightmost daughter artery, as the angle increases. There are also slight differences in WSSG location around the apex. A similar trend can be noticed in case P0207, where there are large differences in WSSG magnitude along the leftmost daughter artery, and especially close to the bifurcation apex. There is also a noticeable relocation of the WSSG around the apex, where a narrow

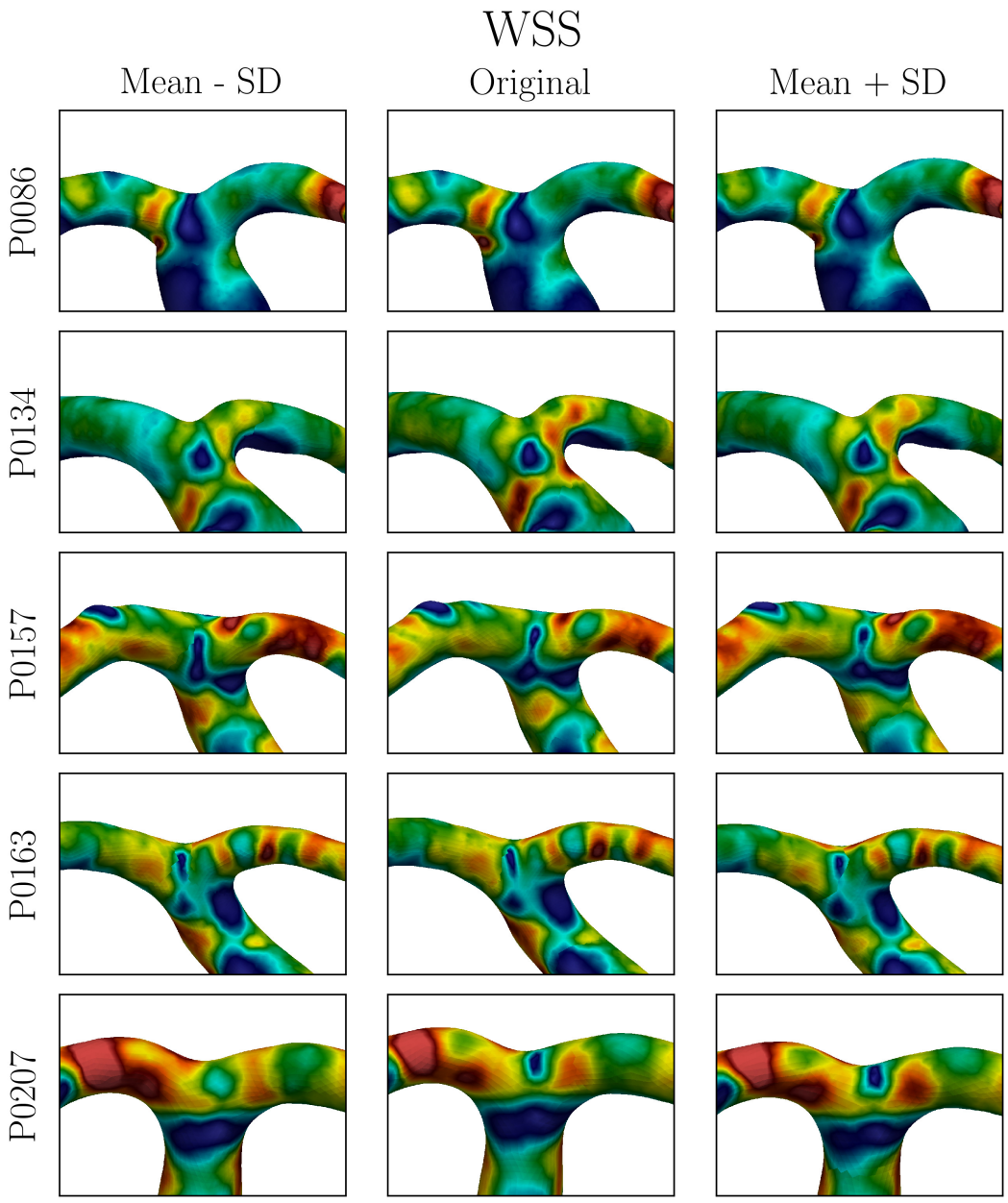

Figure 7.5: WSS for five cases, with three simulations per case, where the the anterior bend angle has been adjusted ± one SD.

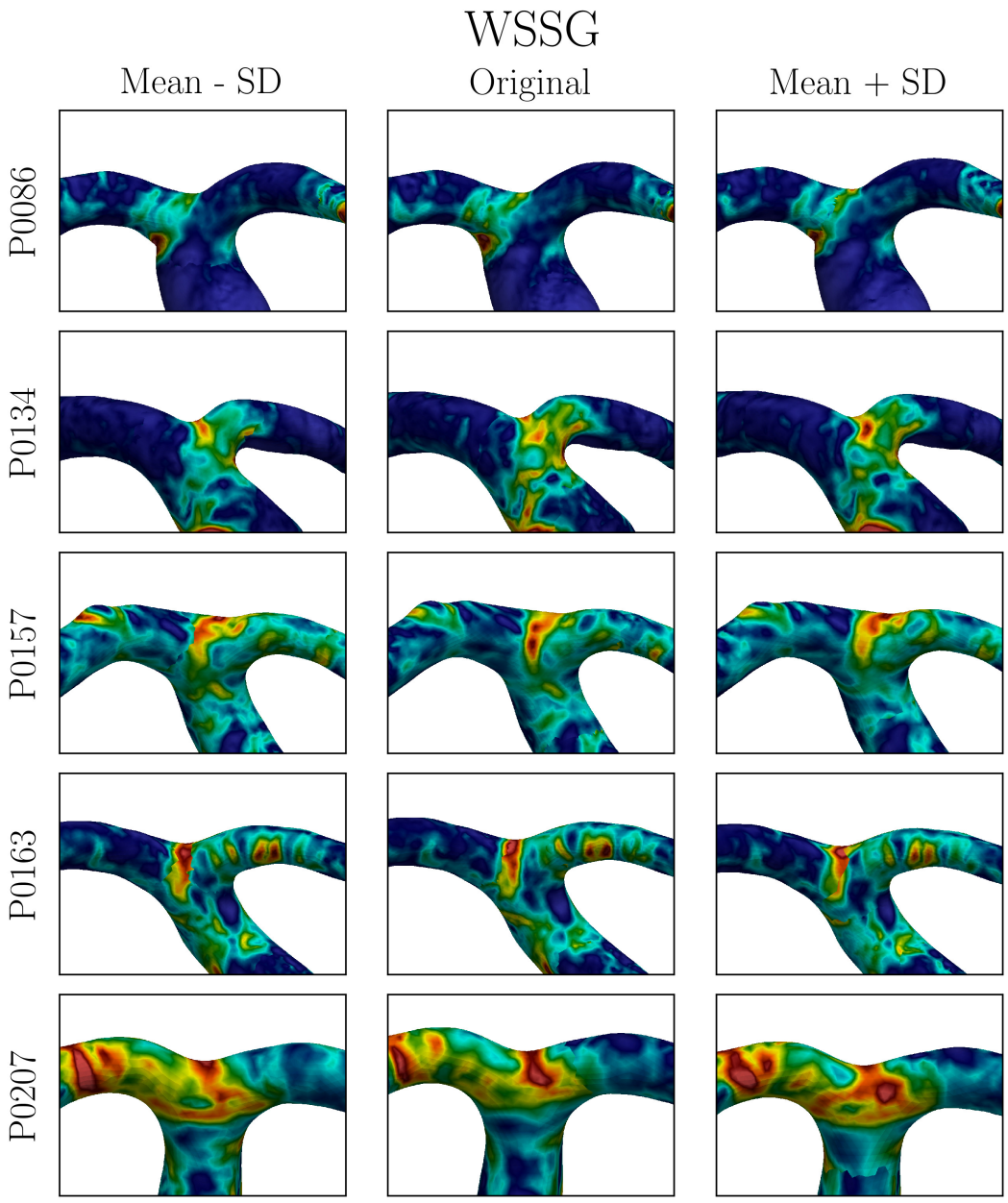

Figure 7.6: WSSG for five cases, with three simulations per case, where the the anterior bend angle has been adjusted ± one SD.

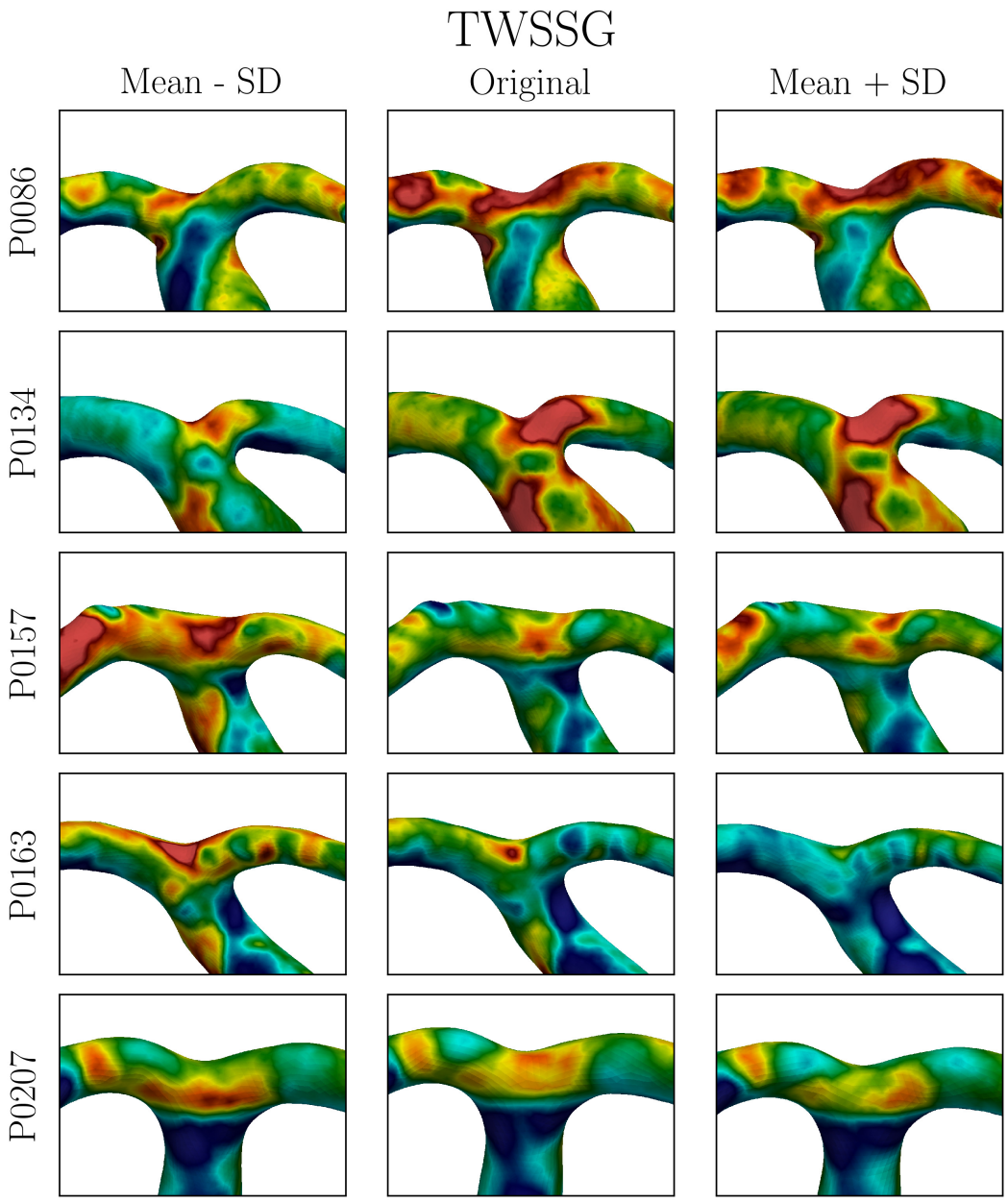

Figure 7.7: TWSSG for five cases, with three simulations per case, where the the anterior bend angle has been adjusted ± one SD.

angle leads to a gradient peak at the apex, whereas a greater angle relocates the gradient peak upstream of the apex.

Figure 7.7 presents the TWSSG of the five cases which underwent angle adjustments. Adjusting the anterior bend angle is affecting the magnitude of the TWSSG. There are considerable phenotypical differences in geometries consisting of a narrow bend angle, compared to geometries with a wide bend angle. Cases P0086 and P0134 appear to react completely opposite of the other cases, where the TWSSG is increased as the angle widens. Overall, there are no noteworthy differences in location of the affected areas.

7.3 Discussion

The goal of this chapter was to investigate the potential link between morphologic features which have been statistically linked with aneurysm initiation, and the hemodynamic stimuli at the terminus bifurcation of the ICA. Thus, we may shed light on the following question: what is the leading cause of hemodynamic stimuli, which promotes adverse remodeling of the blood vessel, and consequently aneurysm initiation?

7.3.1 Aneurysm Initiation in Correlation to High WSS and WSSG

The results of the computational study were used to investigate the leading theory for aneurysm initiation by Meng et al. (2007) [10], in which it was hypothesized that a combination of high WSS and WSSG are correlated to aneurysm initiation. In addition, we compare our results with previous studies, which have shown how high peak curvature and a narrow anterior bend angle are statistically linked with the presence of aneurysms [21, 22].

Curvature variations in the anterior bend show no direct correlation to WSS or WSSG magnitude, confirmed by the results and additional simulations. However, there is a clear difference in WSS in the inner peak of the anterior bend, which might confirm the conclusion presented by Lauric et al. [21], who studied aneurysm initiation along the vessel wall of the anterior bend. There is arguably an overall increase in WSS as the curvature increases, but the phenotypical distinctions are inconsequential.

In comparison to previous work, there are slight differences between the curvature analysis. The results of this thesis focused on the presence of aneurysms at the ICA terminus bifurcation, whereas Lauric et al. investigated the correlation between peak curvature of the anterior bend, and presence of sidewall

aneurysms along the inner carotid siphon. The study by Lauric et al. concluded that aneurysms seemed to form distal from the site of peak curvature due to fluctuating high WSS and WSSG. In order to verify the results of Lauric et al., an additional analysis of the hemodynamic stimuli in the anterior bend region could have been performed, although this was not considered in this thesis.

Angle variations in the anterior bend do not appear to affect WSS or WSSG magnitude at the terminus bifurcation. Although there are observable differences in WSS and WSSG magnitude for particular cases, the results are phenotypically similar, and follow no particular trend.

Regarding angle variations, we considered the results presented by Silva et al., who proposed that a narrow anterior bend angle may alter hemodynamic stimuli, which consequently influences aneurysm initiation. However, the variations in hemodynamic stimuli were only assessed indirectly. Furthermore, the study consisted of patients with aneurysms located at the three first bifurcations of the cerebral arteries: the posterior communicating artery, the anterior communicating artery, and the middle cerebral artery (MCA). Thus, we are guaranteed that the observations of Silva et al. are related to aneurysm presence at the ICA terminus bifurcation, corresponding to the ICA at its junction with the MCA.

As mentioned in Chapter 1, the experiments by Meng et al., and Metaxa et al. were performed in canines and rabbits, respectively. In addition, several features which are linked with human aneurysmal diseases were neglected, such as hypertension, smoking, gender, and familial preponderance. Hence there is no guarantee that the results can be directly translated to human physiology, and the relevance of the results to human intracranial aneurysms requires further investigation. Zeng et al. performed a comparison of the anatomy and the hemodynamics in rabbit and human arteries, and showed that most hemodynamic and geometric features were translatable between species [56]. However, the increased flow rate of 325% is not physiological in human beings. The maximal cardiac output during peak exercise only contributes to a 23% increase in flow rate in the ICA, complemented by blood vessel adaptation, due to CO_2 rich blood, which causes vessels to expand. Furthermore, Khan et al. performed a computational study which showed how the CFD solvers used in the animal experiments were insufficient to capture flow instabilities [14]. Considering flow instabilities have been observed at a considerably lower Reynolds number in the ICA, than presented in the animal experiments, the feature of unstable flow should not be neglected, and may affect the hemodynamic outcome. These are limitations of the *in vivo* experiments by Meng et

al. and Metaxa et al. which might explain why the leading theory does not hold.

The results show that variations in curvature and angle of the anterior bend do not affect WSS or WSSG, thus contradicting the theory by Meng et al. Thus, we are left with the following question: If high WSS and WSSG do not account for the hemodynamic stimuli which promote the adverse vessel wall remodeling, what does?

7.3.2 Aneurysm Initiation in Correlation with Blood Flow Instabilities

The TWSSG is a suggested mathematical formula, used to measure the time-averaged changes in direction and magnitude of the WSS. Thus, TWSSG measures the flow instabilities within the ICA, although the formula is not commonly reported by studies in hemodynamics. Studying the nature of flow instabilities may shed light on which forces that are involved in aneurysm initiation, as proposed by Valen-Sendstad et al. [17]. Unlike the results of the WSS and WSSG, there are distinct visible changes in the TWSSG. Curvature variations show TWSSG of similar overall magnitude, but the area of impact changes location, in particular the areas surrounding the apex. All of the geometries, which underwent angle variation, show how changes in the angle of the anterior bend influence the TWSSG. Thus the hypothesis of TWSSG being a contributing factor to hemodynamic stimuli appears more plausible.

Regrettably, to the author's knowledge, there is an absence of previous studies performing an objective manipulation of the anterior bend angle in either synthetic or patient-specific models. Similarly, there are no known reports of objective manipulation, with respect to peak curvature variation, of the anterior bend in patient-specific models. Nonetheless, we hope the results of this thesis may contribute to explain the correlation between the relevant geometric properties of the anterior bend, and the presence of hemodynamic stimuli.

Peak curvature variations appear to affect TWSSG, although there are only slight magnitudal differences between the original geometry, and the geometry with increased peak curvature. For the reported cases, the primary observations is a relocation of TWSSG in case P0086, a decrease of TWSSG as the curvature increases in case P0134, and an increase of TWSSG as the curvature increases for cases P0157, P0163, and P0207. The small differences across all cases may be explained by the arguably small manipulations of the models during curvature variation. The amount of manipulation was ultimately determined by the criteria for selection of the compression factors, α and β,

where we required

$$\|\alpha\beta\| > 0.15, \tag{7.15}$$

with the reported mean value for curvature variations of $\overline{\|\alpha\beta\|}_{\kappa} = 0.18$, contrary to the mean value for angle variations of $\overline{\|\alpha\beta\|}_{\theta} = 0.51$. The low mean value of curvature variations is linked back to the sensitivity of curvature, where we have previously discussed how large changes in curvature do not necessarily imply large geometric manipulations, in comparison to angle adjustments. In hindsight, there could have been made an effort to achieve a similar mean value of $\|\alpha\beta\|$, which may have been a better reflection of the interpatient variability.

The results of cases P0086 and P0134, which contradicts the hypothesis by Lauric et al. and Silva et al., may be explained by considering the shape of the anterior bend. The shape of the anterior bend in cases P0086 and P0134 changed, due to manipulation. Reducing the peak curvature of the anterior bend causes the bend to resemble a C-shape, while the anterior bend with increased peak curvature resembles a U-shape. Consequently, the mean curvature of a C-shaped bend is higher compared to that of a U-shaped bend, which may be a contributing factor causing hemodynamic stimuli. In previous studies by Sangalli et al. (2009A, 2009B), the shape of the anterior bend was shown to be correlated to hemodynamics, and aneurysm development [57, 40]. Sangalli et al. studied a total of 65 patient, and observed that 70% of the patients with aneurysms located at or after the terminus bifurcation possessed V-shaped siphons. Furthermore, all the ICAs without aneurysms were U-shaped. However, it is debatable whether aneurysm development is less frequent in ICAs consisting of a U-shaped anterior bend. Although the shape of the anterior bend was not considered during manipulation or simulation, we propose that the previous studies on associations between geometry and aneurysm development may explain the results of these particular cases. Angle variations in the anterior bend have an unquestionable correlation with changes in TWSSG. Although there are no apparent observations of TWSSG relocation, the TWSSG magnitude is greatly affected. This supports the conclusion of Silva et al., arguing that a narrow anterior bend angle may alter the hemodynamic stimuli. Admittedly, cases P0086 and P0134 deviates from the other cases. Both cases show little difference between the original geometry and the geometry with a widened anterior bend, which can indicate that something other than bend angle is affecting the flow characteristics. Considering the angle variations produce a large distinction between the anterior bend shapes, it is likely the bend shape should be considered, as addressed above, and explaining the results of cases P0086 and P0134.

So far the presence of unstable flow has been purely speculation based on

the TWSSG. Mathematically, TWSSG indicates fluctuations in direction and magnitude of the WSS, suggesting the presence of flow instabilities. However, the presence of high TWSSG can also be interpreted biologically. It has previously been reported, in biomechanical studies, that temporal gradients have a destructive effect on the endothelial cells, shown *in vivo*, *in vitro*, and *in silico*. Langille et al. (1986) performed *in vivo* experiments in rabbits, and reported an increased endothelial cell turnover in regions affected by unstable flow [58]. Although the hemodynamic stimuli were not precisely measured, their findings indicate a correlation between unstable flow and endothelial cell turnover. *In vitro* experiments were performed by Davies et al. (1986), studying temporal gradients by exposing endothelial cells to turbulent flow. Davies et al. demonstrated how the mechanotransduction was affected negatively by low turbulent intensity, which caused endothelial cell retraction and loss [59]. Finally, in a computational study by White et al. (2005) showed how temporal gradients, in contrast to spatial gradients, caused by high-frequency velocity fluctuations, initiated distinct cellular responses [60]. Only temporal gradients were shown to cause enhanced endothelial cell proliferation. Although the effects of TWSSG have previously been studied, the remarks concerning temporal gradients cannot be interpreted as conclusive. The cause of mechanotransduction and adverse remodeling of the vessel wall is not fully understood, and requires further research. However, based on previous research, it is reasonable to assume that TWSSG is influencing unhealthy mechanotransduction.

The TWSSG is one particular representation of oscillations in WSS, which may indicate unstable flow patterns. However, visualizing unstable flow structures can be accomplished in several ways. We propose volume rendering of the Q-criterion, which is a good indicator of turbulent flow structures. The Q-criterion states that the magnitude of the vorticity tensor is larger than the magnitude of the strain tensor [61],

$$\mathrm{Q} = \frac{1}{2}\left(\|\mathbf{\Omega}\|_F^2 - \|\mathbf{S}\|_F^2\right) > 0, \tag{7.16}$$

where $\mathbf{\Omega} = \frac{1}{2}(\nabla\mathbf{u} - (\nabla\mathbf{u})^T)$ is the vorticity tensor, $\mathbf{S} = \frac{1}{2}(\nabla\mathbf{u} + (\nabla\mathbf{u})^T)$ is the strain tensor, and $\|\cdot\|_F$ denotes the Frobenius norm. This quantity has been visualized to show the propagation of vortex structures and unstable flow patterns during different stages of the cardiac cycle.

Using case P0163 as a representative case, the Q-criterion has been visualized in Figure 7.8 for three different time points during the cardiac cycle. The selected points represent three local velocity maximum throughout a cardiac cycle, applied at the inlet. The visualization shows how the fluctuations dissipate with time, and how the flow instabilities are equalized. The flow structures in geometries with curvature variation show no noticeable difference. However,

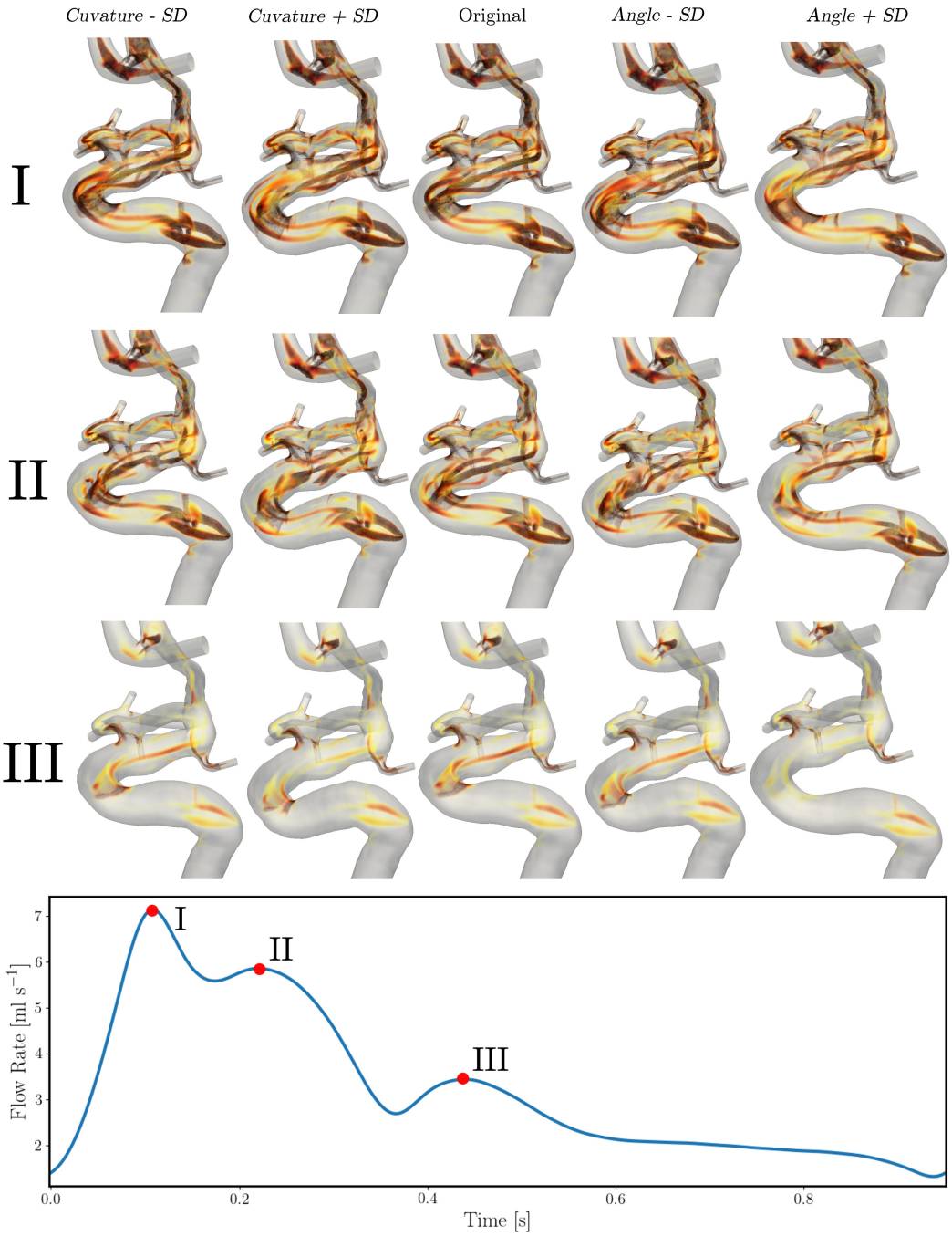

Figure 7.8: Volume rendering of the Q-criterion for all five simulations using case P0163 as the representative case. Snapshots were taken at the three peaks of the ICA velocity profile marked with red circles along the profile, denoted **I**, **II** and **III**.

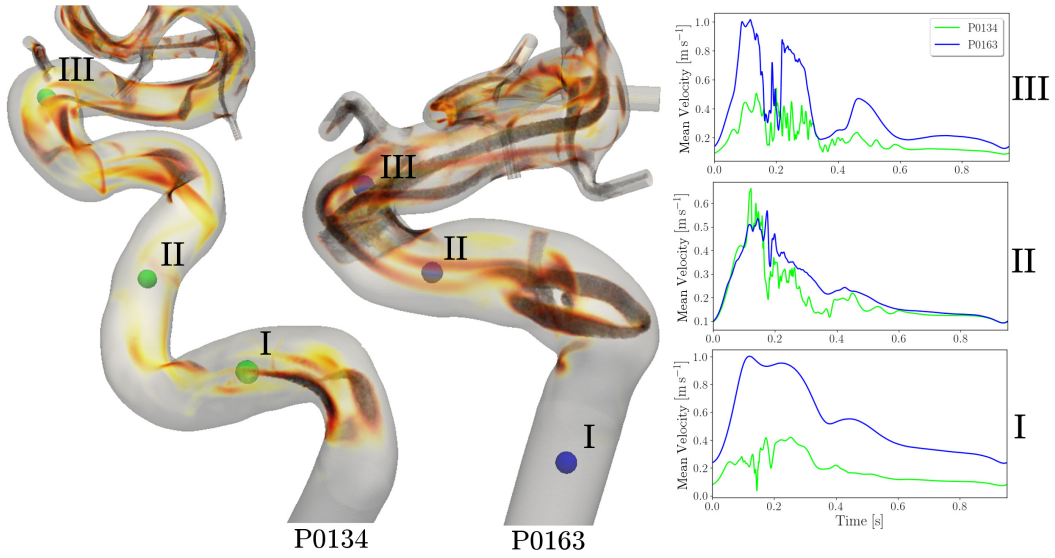

Figure 7.9: Volume rendering of the Q-criterion for case P0134 (left) and P0163 (right), indicating the origin of the unstable flow. The snapshot represents the peak systole of the cardiac cycle. The mean velocity profile, throughout one cardiac cycle, is vizualized at three separate probes in both models.

there is a noticeable difference due to angle variations, particularly for a narrow anterior bend angle. The flow originated at peak systole (**I**) introduces unstable-like structures which are noticeable at the second velocity peak (**II**). The presence of additional instabilities may indicate how narrow angles of the anterior bend are prone to increase unstable flow.

Furthermore, the Q-criterion reveals where the unstable flow structures originate. In particular, the comparison of unstable structures in cases P0134 and P0163 are shown in Figure 7.9, including three probes for mean velocity analysis. The instabilities in case P0134 arise further upstream of the anterior bend, whereas the flow is steady upstream of the anterior bend in case P0163. This is reflected in the velocity profiles of case P0134 (**I** and **II**), where we observe instabilities upstream of the anterior bend. We can speculate whether the origin of unstable flow varies with the geometry of the ICA, or if this is purely a computational limitation considering more of the ICA is included in case P0134, which includes several tortuous segments. Regardless, the overall tortuosity of the ICA it is worth including as a contributing factor in the presence of unstable flow, as suggested by Piccinelli et al. [23].

Finally, we will consider the location of TWSSG, in correlation with the fact that approximately 90% of intracranial aneurysms are located at bifurcations. Indeed, peak TWSSG is almost exclusively located at bifurcations, as high-

lighted using a representative case in Figure 7.11. The visualization emphasizes

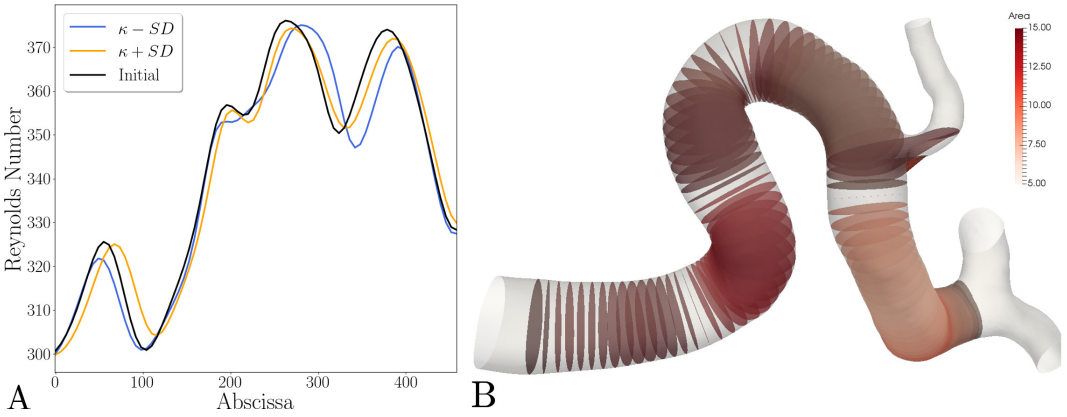

Figure 7.10: **A** Evolution of the Reynolds number (Re) along the abscissa of the ICA, including the original model and the manipulated models with respect to curvature adjustment. **B** The initial model containing the cross-sections used for computation of mean velocity. A sudden increase in area is noticeable in the vicinity of the ophthalmic artery.

the specific impact of flow instabilities at bifurcations throughout the carotid arteries, and includes the WSS of the model. The particular location of high TWSSG may also strengthen the possible correlation between flow instabilities and aneurysm initiation, considering approximately 90% of all cerebral aneurysms are located in the vicinity of the first two branches after the ICA, specifically at bifurcations [62]. The explanation for the absence of aneurysms in bifurcations further downstream follows from the evolution of the Reynolds number (Re), defined as

$$\mathrm{Re} \ = \frac{\overline{u}\, d}{\nu}, \tag{7.17}$$

where $\overline{u}$ is the mean velocity through a cross-section of the ICA, ν is the kinematic viscosity, and d is the characteristic length scale. The presence of unstable flow are correlated with the evolution of Re throughout the Circle of Willis. First, we will consider area variations of the ICA. It has been shown using conical diffusers that flow separation, an early transition to the turbulent flow regime, can be expected for angles above 5° for Reynolds numbers less than 2000 [63]. Although this threshold might not be directly translated to arteries, the observation is reason enough to believe that sudden area variations in the vessel may introduce unstable flow. However, based on the discussion in Chapter 6, we argue that the horizontal change in the area across the cases do not substantially affect Re. For verification, a comparison of Re for curvature variations is shown in Figure 7.10 **A**, using a representative case. The

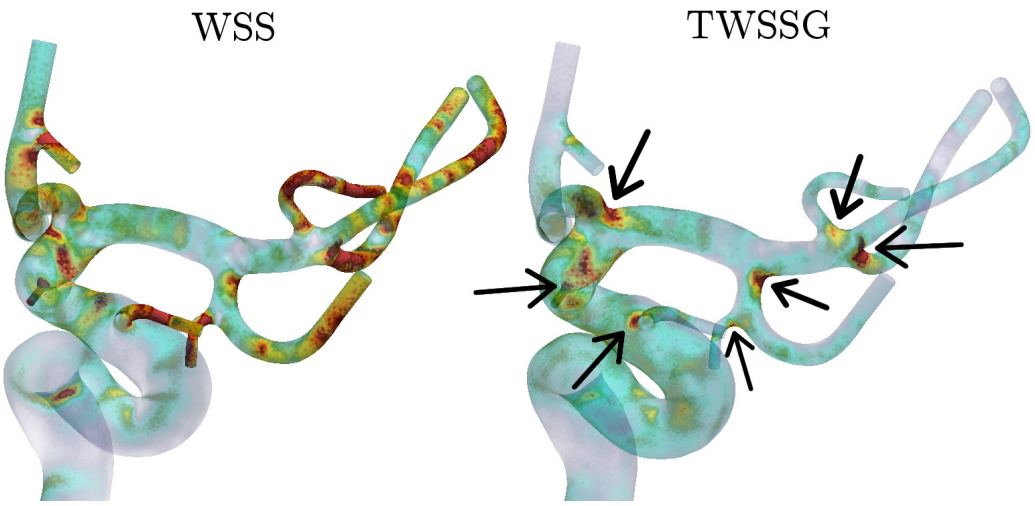

Figure 7.11: Opacity mapping emphasising the locations of high WSS (left) and TWSSG (right) for case P0134. Arrows indicate the areas of high TWSSG.

comparison shows a clear correlation between the peaks along the siphon, and a magnitudal similarity. Towards the end of the siphon, there is a noticeable decrease in Re, creating a saddle point. The decrease is caused by the combination of a sudden increase in area, as the cross-sections pass the ophthalmic artery, as shown in Figure 7.10 **B**, and by flow passing the bifurcation at the ophthalmic artery, which leads to the second point.

The presence and dissipation of unstable flow is correlated with the Reynolds number. The Circle of Willis is a network consisting of multiple bifurcations which have an immediate effect on Re. A rough estimation of how Re changes after a bifurcation can be made by considering a fully symmetric bifurcation with two daughter branches of equal radius. Assuming Murray's law is valid, it can be shown that Re is reduced by approximately 60% for each bifurcation. However, previous studies have suggested that Murray's law may scale with two, instead of three, in the vicinity of the Circle of Willis [18, 64], which would reduce Re by approximately 70% for each bifurcation. Regardless, the approximation heavily implies that flow instabilities with origin in the vicinity of the anterior bend will dissipate, and stabilize quickly. Besides, the estimation provides a plausible explanation for the absence of aneurysms further downstream in the carotid arteries. The explanation is also supported by the locations of peak TWSSG as shown in Figure 7.11, strengthening the theory of TWSSG being the cause of aneurysm initiation.

7.3.3 Modeling Assumptions

Computational fluid dynamics analysis applies a range of assumptions and simplifications, in order to reduce the computational effort, and to specify flow conditions. Hence, it is necessary to consider the most common assumptions, to see how they can affect the fluid flow, and possibly the simulation results.

First, we will address assumptions made when modeling blood. Blood is by nature a non-Newtonian fluid, and does not satisfy Newton's Law of Viscosity. Instead, the viscosity of blood decreases under shear strain, known as shear-thinning. Hence, blood should ideally be modeled using viscosity models. A recent study by Khan et al. (2018) performed simulations of flow through a non-axisymmetric stenosis model, in order to study the impact of shear-thinning in transitional blood flows [65]. Using a conventional definition of Re, based on high-shear viscosity, showed that transition was delayed for the shear-thinning model. However, using a domain-averaged viscosity, the transition, evolution of perturbations, and turbulent flow patterns remained similar.

Furthermore, a consequence of modeling blood as a Newtonian fluid was analyzed by Xiang et al. (2011), where the results showed only a significant difference (10-20%) in a very slow recirculating flow in aneurysms, but no effect in the rest of the model [66]. In a study by Evju et al. Newtonian and non-Newtonian models were compared, and were found to correlate strongly on most WSS-based indicators [67]. Thus, Newtonian rheology had a negligible impact on the WSS, and by extension, on the TWSSG.

Modeling of blood vessels in arterial trees require assumptions about the vessel walls. Contrary to the reality of the artery walls, most CFD analyses assume the vessel walls to be rigid, and not compliant, which may affect the estimation of hemodynamic quantities. Previous studies using fluid-structure interaction (FSI) solvers to model the effect of a compliant wall found an effect up to 50% in WSS inside aneurysms [68]. It is worth mentioning that this was for a point value comparison, and changes in WSS due to a compliant geometry could be considered negligible when considering sac averages, as the material properties are only estimated. Thus, the effect of FSI does not alter the overall stress in the aneurysm, and is generally neglected in most arterial studies. In addition, FSI modeling requires more complex computational models, and increases the computational time. Furthermore, a comparison between the blood flow characterization, obtained from numerical simulations in a rigid wall model, did not significantly differ from that in compliant models, where the deformation field was extrapolated from the bidimensional measurements [69, 70].

Patient-specific models of the ICA require the specification of physiological

flow conditions. Variable inlet profiles have been presented in retrospective studies, to select the most plausible waveform to represent the pulsation of the heart. The waveform applied in this thesis is based on the waveform presented by Hoi et al. [53]. The waveform presented by Hoi et al. is a volumetric blood flow rate waveform, and is suitable as a boundary condition for models of blood flow through the cerebral arteries.

Using patient-specific flow rates may change the transition between laminar and turbulent-like flow. However, patient-specific flow rates are rarely available, and have to be approximated. At the inlet, we seek to derive a relationship between the flow rate and the cross-sectional vessel area of the ICA, as proposed by Cebral et al. [71]. Based on the Poiseuille law for steady flow, Cebral et al. assumed a power-law relationship between the flow rate Q, and the cross-sectional area A, on the form

$$Q = k \cdot A^n \qquad k \in \mathbb{R}. \tag{7.18}$$

Based on this model, Valen-Sendstad et al. compared a square-law ($n = 2$) and a cube-law ($n = 3$), where the flow rate was scaled with the radius squared and cubed, respectively [54]. Based on simulations using models from the Aneurisk database, they demonstrated that the square-law resulted in flow rates which demonstrably fell within a physiological range, and was more appropriate for estimating ICA flow rates than the cube-law. Hence it is a reasonable assumption that Murray's law may scale with two instead of three in the vicinity of the Circle of Willis [18, 71]. Therefore, the simulations were performed with a flow rate following a square-law.

7.4 Conclusion

The results presented in this chapter and the following discussing indicate that the theory by Meng et al. might not hold. We have shown there is no correlation between the morphological features which are statistically linked with aneurysm initiation, and high WSS and WSSG. There may be a direct correlation between the considered morphological features, and unstable flow, as shown through observation of high TWSSG. However, the results of the TWSSG are inconclusive and require further analysis in order to determine whether or not TWSSG can be considered the cause of aneurysm initiation. Additionally, we propose that results presented in this thesis should be viewed in combination with Bergersen's results, who performed similar geometric manipulations [24].

Improvements can be made with increased knowledge of the mechanotransduction pathway. For future work, we propose that a larger cohort study using the presented framework for geometric manipulation would shed light on the influence of the TWSSG on aneurysm development.

8. Future Work and Conclusions

8.1 Future Work

The main objectives of this thesis can be summarized in the three following points:

- Landmarking of the Internal Carotid Artery
- Manipulation of the Anterior Bend
- Computational Fluid Dynamics of the Internal Carotid Artery

Regrettably, the authors behind the landmarking procedures, peak curvature evaluation, and anterior bend angle measurements did not provide a sufficient amount of information in order to reproduce their results. Instead, it was necessary to dedicate Chapter 3: *Estimation of Discrete Curvature and Torsion* and Chapter 4: *Measurement of the Anterior Bend Angle* to evaluate several methods for geometric measurement, which could have been prevented if the original studies provided sufficient information. However, the presented tools in this thesis are admittedly not perfect, and may not be the ideal measure, making them suitable for further validation.

The computational study in this thesis indicates the importance of flow conditions, and parameters used throughout the simulations. Besides, several features of the geometries were not considered, in particular, the shape of the anterior bend, which may influence the results. The results and following discussion about the challenges of realistic flow simulations using CFD, show how CFD can provide misleading information. Although CFD simulations have proven itself as a valuable tool, verification and validation are essential for any CFD analysis, and previously reported results should be revisited.

8.2 Conclusions

To recap, **the goal of the thesis** was to develop a framework for geometric manipulation of patient-specific models, followed by computational fluid dy-

namics analysis in order to investigate the correlation between hemodynamic stimuli at the terminus bifurcation of the internal carotid artery, with the initiation of intracranial aneurysms. To summarize, the main conclusions of this thesis are:

- Estimation of higher order derivatives of discrete curves have shown to be highly sensitive to input parameters.
- A reliable and objective framework for landmarking of the internal carotid artery is implemented and presented.
- Measurements of bend angles within the cerebral arteries may not be the ideal measure of a physiological bend.
- A framework for objective manipulation of morphological features is presented in order to adjust the angle, and peak curvature of the anterior bend.
- There is no apparent correlation between high WSS and WSSG at the terminus bifurcation, and morphological features, which are statistically linked with aneurysm initiation.
- Unstable flow is present and affects the hemodynamic stimuli temporally. Hence, the turbulent-like flow may be linked with morphological features associated with aneurysms, possibly being the cause of aneurysm initiation. Further research is required to verify this observation.

Bibliography

[1] Emelia J Benjamin, Salim S Virani, Clifton W Callaway, Alanna M Chamberlain, Alexander R Chang, Susan Cheng, Stephanie E Chiuve, Mary Cushman, Francesca N Delling, Rajat Deo, et al. Heart disease and stroke statistics—2018 update: a report from the american heart association. *Circulation*, 137(12):e67–e492, 2018.

[2] UCAS Japan Investigators et al. The natural course of unruptured cerebral aneurysms in a japanese cohort. *N Engl J Med*, 2012(366):2474–2482, 2012.

[3] JaGJR van Gijn and GJE Rinkel. Subarachnoid haemorrhage: diagnosis, causes and management. *Brain*, 124(2):249–278, 2001.

[4] S Claiborne Johnston, Steve Selvin, and Daryl R Gress. The burden, trends, and demographics of mortality from subarachnoid hemorrhage. *Neurology*, 50(5):1413–1418, 1998.

[5] N.A. Kumar. Aneurysm. `http://www.medindia.net/patients/patientinfo/images/aneurysm.jpg` [Accessed 08.10.2017], December 2014.

[6] Marieke JH Wermer, Hieke Kool, Kees W Albrecht, and Gabriël JE Rinkel. Subarachnoid hemorrhage treated with clipping: long-term effects on employment, relationships, personality, and mood. *Neurosurgery*, 60(1):91–98, 2007.

[7] Alexander Keedy. An overview of intracranial aneurysms. *McGill Journal of Medicine: MJM*, 9(2):141, 2006.

[8] Cornelia Hahn and Martin A Schwartz. Mechanotransduction in vascular physiology and atherogenesis. *Nature reviews. Molecular cell biology*, 10(1):53, 2009.

[9] Peter F Davies. Hemodynamic shear stress and the endothelium in cardiovascular pathophysiology. *Nature Reviews Cardiology*, 6(1):16, 2009.

[10] Hui Meng, Zhijie Wang, Yiemeng Hoi, Ling Gao, Eleni Metaxa, Daniel D Swartz, and John Kolega. Complex hemodynamics at the apex of an arterial bifurcation induces vascular remodeling resembling cerebral aneurysm initiation. *Stroke*, 38(6):1924–1931, 2007.

[11] Hui Meng, Daniel D Swartz, Zhijie Wang, Yiemeng Hoi, John Kolega, Eleni M Metaxa, Michael P Szymanski, Junichi Yamamoto, Eric Sauvageau, and Elad I Levy. A model system formapping vascular-responses to complex hemodynamics at arterial bifurcations in vivo. *Neurosurgery*, 59(5):1094–1101, 2006.

[12] Eleni Metaxa, Markus Tremmel, Sabareesh K Natarajan, Jianping Xiang, Rocco A Paluch, Max Mandelbaum, Adnan H Siddiqui, John Kolega, J Mocco, and Hui Meng. Characterization of critical hemodynamics contributing to aneurysmal remodeling at the basilar terminus in a rabbit model. *Stroke*, 41(8):1774–1782, 2010.

[13] Kristian Valen-Sendstad and DA Steinman. Mind the gap: impact of computational fluid dynamics solution strategy on prediction of intracranial aneurysm hemodynamics and rupture status indicators. *American Journal of Neuroradiology*, 35(3):536–543, 2014.

[14] MO Khan, K Valen-Sendstad, and DA Steinman. Narrowing the expertise gap for predicting intracranial aneurysm hemodynamics: impact of solver numerics versus mesh and time-step resolution. *American Journal of Neuroradiology*, 36(7):1310–1316, 2015.

[15] Markus Tremmel, Jianping Xiang, Yiemeng Hoi, John Kolega, Adnan H Siddiqui, J Mocco, and Hui Meng. Mapping vascular response to in vivo hemodynamics: application to increased flow at the basilar terminus. *Biomechanics and modeling in mechanobiology*, 9(4):421–434, 2010.

[16] Kristian Valen-Sendstad, Kent-André Mardal, and David A Steinman. High-resolution cfd detects high-frequency velocity fluctuations in bifurcation, but not sidewall, aneurysms. *Journal of biomechanics*, 46(2):402–407, 2013.

[17] Kristian Valen-Sendstad, Marina Piccinelli, and David A Steinman. High-resolution computational fluid dynamics detects flow instabilities in the carotid siphon: Implications for aneurysm initiation and rupture? *Journal of biomechanics*, 47(12):3210–3216, 2014.

[18] Tor Ingebrigtsen, Michael K Morgan, Ken Faulder, Linda Ingebrigtsen, Trygve Sparr, and Henrik Schirmer. Bifurcation geometry and the presence of cerebral artery aneurysms. *Journal of neurosurgery*, 101(1):108–113, 2004.

[19] Allen L Ho, Ning Lin, Kai U Frerichs, and Rose Du. Intrinsic, transitional, and extrinsic morphological factors associated with rupture of intracranial aneurysms. *Neurosurgery*, 77(3):433–442, 2015.

[20] Sarah Schimansky, Samir Patel, Jason Rahal, Alexandra Lauric, and Adel M Malek. Extradural internal carotid artery caliber dysregulation is associated with cerebral aneurysms. *Stroke*, 44(12):3561–3564, 2013.

[21] Alexandra Lauric, James Hippelheuser, Mina G Safain, and Adel M Malek. Curvature effect on hemodynamic conditions at the inner bend of the carotid siphon and its relation to aneurysm formation. *Journal of biomechanics*, 47(12):3018–3027, 2014.

[22] Ângelo Raimundo Silva Neto, Ródio Luis Brandão Câmara, and Marcelo Moraes Valença. Carotid siphon geometry and variants of the circle of willis in the origin of carotid aneurysms. *Arquivos de neuro-psiquiatria*, 70(12):917–921, 2012.

[23] Marina Piccinelli, Susanna Bacigaluppi, Edoardo Boccardi, Bogdan Ene-Iordache, Andrea Remuzzi, Alessandro Veneziani, and Luca Antiga. Geometry of the internal carotid artery and recurrent patterns in location, orientation, and rupture status of lateral aneurysms: an image-based computational study. *Neurosurgery*, 68(5):1270–1285, 2011.

[24] Aslak Wigdahl Bergersen. Investigating the link between patient-specific morphology and hemodynamics: Implications for aneurism initiation? Master's thesis, University of Oslo, 2016.

[25] Frank M. White. *Viscous Fluid Flow*. McGraw-Hill, 3rd edition edition, 2006.

[26] Charles L Fefferman. Existence and smoothness of the navier-stokes equation. *The millennium prize problems*, pages 57–67, 2006.

[27] Todd Dupont, Johan Hoffman, Claus Johnson, Robert C Kirby, Mats G Larson, Anders Logg, and L Ridgway Scott. The fenics project. Technical report, Tech. Rep. 2003–21, Chalmers Finite Element Center Preprint Series, 2003.

[28] Mikael Mortensen and Kristian Valen-Sendstad. Oasis: A high-level/high-performance open source navier–stokes solver. *Computer physics communications*, 188:177–188, 2015.

[29] James Ahrens, Berk Geveci, and Charles Law. Paraview: An end-user tool for large data visualization. *The Visualization Handbook*, 717, 2005.

[30] JC Simo and F Armero. Unconditional stability and long-term behavior of transient algorithms for the incompressible navier-stokes and euler equations. *Computer Methods in Applied Mechanics and Engineering*, 111(1-2):111–154, 1994.

[31] Guttorm Magnus Leiel Kvaal. Numerical simulations of pharmaceutical particles depositing in the human respiratory system. Master's thesis, 2017.

[32] GI Taylor and AE Green. Mechanism of the production of small eddies from large ones. *Proceedings of the Royal Society of London. Series A, Mathematical and Physical Sciences*, 158(895):499–521, 1937.

[33] Luca Antiga. Patient-specific modeling of geometry and blood flow in large arteries. *Politecnico di Milano*, 2002.

[34] Hrvoje Bogunović, José María Pozo, Rubén Cárdenes, María Cruz Villa-Uriol, Raphaël Blanc, Michel Piotin, and Alejandro F Frangi. Automated landmarking and geometric characterization of the carotid siphon. *Medical image analysis*, 16(4):889–903, 2012.

[35] Luca Antiga, Marina Piccinelli, Lorenzo Botti, Bogdan Ene-Iordache, Andrea Remuzzi, and David A Steinman. An image-based modeling framework for patient-specific computational hemodynamics. *Medical & biological engineering & computing*, 46(11):1097, 2008.

[36] Marina Piccinelli, Alessandro Veneziani, David A Steinman, Andrea Remuzzi, and Luca Antiga. A framework for geometric analysis of vascular structures: application to cerebral aneurysms. *IEEE transactions on medical imaging*, 28(8):1141–1155, 2009.

[37] Eric Jones, Travis Oliphant, and Pearu Peterson. {SciPy}: open source scientific tools for {Python}. 2014.

[38] Tom Lyche and Knut Morken. Spline methods draft. *Department of Informatics, Center of Mathematics for Applications, University of Oslo, Oslo*, 2008.

[39] Shanggang Zhou and Xiaotong Shen. Spatially adaptive regression splines and accurate knot selection schemes. *Journal of the American Statistical Association*, 96(453):247–259, 2001.

[40] Laura M Sangalli, Piercesare Secchi, Simone Vantini, and Alessandro Veneziani. Efficient estimation of three-dimensional curves and their derivatives by free-knot regression splines, applied to the analysis of inner carotid artery centrelines. *Journal of the Royal Statistical Society: Series C (Applied Statistics)*, 58(3):285–306, 2009.

[41] Yi An, Cheng Shao, Xiaoliang Wang, and Zhuohan Li. Geometric properties estimation from discrete curves using discrete derivatives. *Computers & Graphics*, 35(4):916–930, 2011.

[42] Erich Fischer. Die lageabweichungen der vorderen hirnarterie im gefassbild. zbl. *Neurochir*, 3:300–312, 1938.

[43] Alain Bouthillier, Harry R Van Loveren, and Jeffrey T Keller. Segments of the internal carotid artery: a new classification. *Neurosurgery*, 38(3):425–433, 1996.

[44] Richard L Bishop. There is more than one way to frame a curve. *The American Mathematical Monthly*, 82(3):246–251, 1975.

[45] L Antiga, T Passerini, M Piccinelli, and A Veneziani. Aneurisk web, ecm2. mathcs. emory. edu/aneuriskweb, 2011. *URL: ecm2. mathcs. emory. edu/aneuriskweb*.

[46] E Waihrich, P Clavel, GAC Mendes, C Iosif, I Moraes Kessler, and C Mounayer. Influence of carotid siphon anatomy on brain aneurysm presentation. *American Journal of Neuroradiology*, 38(9):1771–1775, 2017.

[47] Andriy Fedorov, Reinhard Beichel, Jayashree Kalpathy-Cramer, Julien Finet, Jean-Christophe Fillion-Robin, Sonia Pujol, Christian Bauer, Dominique Jennings, Fiona Fennessy, Milan Sonka, et al. 3d slicer as an image computing platform for the quantitative imaging network. *Magnetic resonance imaging*, 30(9):1323–1341, 2012.

[48] Andras Lasso. 3d slicer scripted module for measuring angle between rulers. `https://gist.github.com/lassoan/9bf334743871e400f7e3b3745b312b14`, 2017.

[49] MD Ford, Y Hoi, M Piccinelli, L Antiga, and DA Steinman. An objective approach to digital removal of saccular aneurysms: technique and applications. *The British journal of radiology*, 82(special_issue_1):S55–S61, 2009.

[50] A Mantha, Christof Karmonik, G Benndorf, C Strother, and Ralph Metcalfe. Hemodynamics in a cerebral artery before and after the formation of an aneurysm. *American Journal of Neuroradiology*, 27(5):1113–1118, 2006.

[51] Dominique Attali and Annick Montanvert. Computing and simplifying 2d and 3d continuous skeletons. *Computer vision and image understanding*, 67(3):261–273, 1997.

[52] Aslak Bergersen. Describes a pipeline for automated pre processing of surfaces using vmtk. `https://github.com/aslakbergersen/automatedPreProcessing`, 2018.

[53] Yiemeng Hoi, Bruce A Wasserman, Yuanyuan J Xie, Samer S Najjar, Luigi Ferruci, Edward G Lakatta, Gary Gerstenblith, and David A Steinman. Characterization of volumetric flow rate waveforms at the carotid bifurcations of older adults. *Physiological measurement*, 31(3):291, 2010.

[54] Kristian Valen-Sendstad, Marina Piccinelli, Resmi KrishnankuttyRema, and David A Steinman. Estimation of inlet flow rates for image-based aneurysm cfd models: where and how to begin? *Annals of biomedical engineering*, 43(6):1422–1431, 2015.

[55] Ron Gin, Anthony G Straatman, and David A Steinman. A dual-pressure boundary condition for use in simulations of bifurcating conduits. *Journal of biomechanical engineering*, 124(5):617–619, 2002.

[56] Z Zeng, David F Kallmes, MJ Durka, Y Ding, D Lewis, R Kadirvel, and Anne M Robertson. Hemodynamics and anatomy of elastase-induced rabbit aneurysm models: similarity to human cerebral aneurysms? *American journal of neuroradiology*, 32(3):595–601, 2011.

[57] Laura M Sangalli, Piercesare Secchi, Simone Vantini, and Alessandro Veneziani. A case study in exploratory functional data analysis: geometrical features of the internal carotid artery. *Journal of the American Statistical Association*, 104(485):37–48, 2009.

[58] B Lowell Langille, Michael A Reidy, and Robert L Kline. Injury and repair of endothelium at sites of flow disturbances near abdominal aortic coarctations in rabbits. *Arteriosclerosis, Thrombosis, and Vascular Biology*, 6(2):146–154, 1986.

[59] Peter F Davies, Andrea Remuzzi, Ethel J Gordon, C Forbes Dewey, and Michael A Gimbrone. Turbulent fluid shear stress induces vascular endothelial cell turnover in vitro. *Proceedings of the National Academy of Sciences*, 83(7):2114–2117, 1986.

[60] Charles R White, Mark Haidekker, Xuping Bao, and John A Frangos. Temporal gradients in shear, but not spatial gradients, stimulate endothelial cell proliferation. *Circulation*, 103(20):2508–2513, 2001.

[61] Václav Kolář. Vortex identification: New requirements and limitations. *International journal of heat and fluid flow*, 28(4):638–652, 2007.

[62] David O Wiebers, International Study of Unruptured Intracranial Aneurysms Investigators, et al. Unruptured intracranial aneurysms: natural history, clinical outcome, and risks of surgical and endovascular treatment. *The Lancet*, 362(9378):103–110, 2003.

[63] EM Sparrow, JP Abraham, and WJ Minkowycz. Flow separation in a diverging conical duct: Effect of reynolds number and divergence angle. *International Journal of Heat and Mass Transfer*, 52(13-14):3079–3083, 2009.

[64] JR Cebral, MA Castro, CM Putman, and N Alperin. Flow–area relationship in internal carotid and vertebral arteries. *Physiological measurement*, 29(5):585, 2008.

[65] MO Khan, K Valen-Sendstad, and DA Steinman. Direct numerical simulation of laminar-turbulent transition in a non-axisymmetric stenosis model for newtonian vs. shear-thinning non-newtonian rheologies. *Flow, Turbulence and Combustion*, pages 1–30, 2018.

[66] Jianping Xiang, Markus Tremmel, John Kolega, Elad I Levy, Sabareesh K Natarajan, and Hui Meng. Newtonian viscosity model could overestimate wall shear stress in intracranial aneurysm domes and underestimate rupture risk. *Journal of neurointerventional surgery*, pages neurintsurg–2011, 2011.

[67] Øyvind Evju, Kristian Valen-Sendstad, and Kent-André Mardal. A study of wall shear stress in 12 aneurysms with respect to different viscosity models and flow conditions. *Journal of biomechanics*, 46(16):2802–2808, 2013.

[68] Ryo Torii, Marie Oshima, Toshio Kobayashi, Kiyoshi Takagi, and Tayfun E Tezduyar. Influence of wall elasticity in patient-specific hemodynamic simulations. *Computers & Fluids*, 36(1):160–168, 2007.

[69] Juan R Cebral, Marcelo A Castro, James E Burgess, Richard S Pergolizzi, Michael J Sheridan, and Christopher M Putman. Characterization of cerebral aneurysms for assessing risk of rupture by using patient-specific computational hemodynamics models. *American Journal of Neuroradiology*, 26(10):2550–2559, 2005.

[70] Marcelo A Castro, María C Ahumada Olivares, Christopher M Putman, and Juan R Cebral. Wall motion and hemodynamics in intracranial aneurysms. *Journal of Physics: Conference Series*, 477(1):012004, 2013.

[71] JR Cebral, MA Castro, CM Putman, and N Alperin. Flow–area relationship in internal carotid and vertebral arteries. *Physiological measurement*, 29(5):585, 2008.